SUBSONIC-TRANSONIC SUBMERGED INTAKE DESIGN FOR A CRUISE
MISSILE

A THESIS SUBMITTED TO
THE GRADUATE SCHOOL OF NATURAL AND APPLIED SCIENCES
OF
MIDDLE EAST TECHNICAL UNIVERSITY

BY

ORAL AKMAN

IN PARTIAL FULFILLMENT OF THE REQUIREMENTS
FOR
THE DEGREE OF MASTER OF SCIENCE
IN
AEROSPACE ENGINEERING

NOVEMBER 2014

Approval of the thesis

SUBSONIC-TRANSONIC SUBMERGED INTAKE DESIGN FOR A CRUISE MISSILE

submitted by **ORAL AKMAN** in partial fulfillment of the requirements for the degree of **Master of Science in Aerospace Engineering Department, Middle East Technical University** by**,**

Prof. Dr. Gülbin Dural   _____
Dean, Graduate School of **Natural and Applied Sciences**

Prof. Dr. Ozan Tekinalp   _____
Head of Department, **Aerospace Engineering**

Assoc. Prof. Dr. Sinan Eyi   _____
Supervisor, **Aerospace Engineering Dept., METU**

Examining Committee Members:

Prof. Dr. Nafiz Alemdaroğlu   _____
Aerospace Engineering Dept., METU

Assoc. Prof. Dr. Sinan Eyi   _____
Aerospace Engineering Dept., METU

Prof. Dr. İsmail Hakkı Tuncer   _____
Aerospace Engineering Dept., METU

Prof. Dr. Serkan Özgen   _____
Aerospace Engineering Dept., METU

Emrah Gülay, M.Sc.   _____
Senior Engineer, ROKETSAN

Date: 27/11/2014

I hereby declare that all the information in this document has been obtained and presented in accordance with academic rules and ethical conduct. I also declare that, as required by these rules and conduct, I have fully cited and referenced all material and results that are not original to this work.

Name, Last name   : Oral AKMAN

Signature   :

ABSTRACT

SUBSONIC-TRANSONIC SUBMERGED INTAKE DESIGN FOR A CRUISE MISSILE

Akman, Oral
M.S., Department of Aerospace Engineering
Supervisor: Assoc. Doc. Dr. Sinan Eyi

November 2014, 99 Pages

In this thesis, aerodynamic design and optimization of subsonic-transonic submerged intake is done for specified cruise conditions. A gradient-based optimization algorithm is developed for intake design studies. Subsonic intake geometric parameterization is conducted and a generic submerged intake for a cruise missile is constructed by using CATIA V5 generative shape design module. Computational Fluid Dynamics (CFD) solver FloEFD v12 is used for computational analyses. Two NASA test cases are used for CFD tool validation. Developed optimization algorithm is validated using random initial intake geometry by setting all design parameters free and not using any geometric limits. Application of subsonic intake design optimization is done after validation of optimization algorithm. Intake geometries are compared to each other which are obtained from optimization iterations. CFD analyses are conducted at engine corrected mass flow rate about 4.43 kg/s. All geometries, obtained from optimization algorithm, are compared to each other. Optimized geometry reached 0.945 Pressure Recovery (PR) coefficient and 0.0262 Distortion Coefficient (DC_{DPCP}). An inferior intake geometry chosen as starting point for the optimization algorithm and after five optimization iterations 6.4% improvement in PR and about 45% enhancement in DC coefficients are achieved. On

the other hand total axial force coefficient of cruise missile (C_{Abody}) is reduced about 13% as intake design improved.

ÖZ

SES ALTI ve SES CİVARI HIZLARDA UÇAN BİR SEYİR FÜZESİNİN HAVA ALIĞI TASARIMI

Akman, Oral
Yüksek Lisans, Havacılık Mühendisliği Bölümü
Tez Yöneticisi: Doç. Dr. Sinan Eyi

Kasım 2014, 99 Sayfa

Bu tezde, ses altı ve ses civarı hızlarda uçan bir seyir füzesi için hava alığı aerodinamik tasarımı ve eniyilemesi yapılmıştır. Eniyileme çalışmaları türev tabanlı eniyileme algoritmalarından biri olan "En Hızlı Azalan Eniyileme Metodu" ile "Çizgi Arama Algoritması" ile birlikte kullanılarak geliştirilen bir eniyileme algoritması kullanılarak yapılmıştır. Tasarlanacak hava alığı için geometrik parametreler belirlenmiş ve CATIA V5 katı model programı kullanılarak parametrik bir hava alığı modeli oluşturulmuştur. Elde edilen hava alığı modellerinin aerodinamik analizleri ticari bir Navier-Stokes çözücüsü olan FloEFD v12 kullanılarak yapılmıştır. Literatürde test ve analiz sonuçları bulunan iki adet jenerik hava alığının bu yazılım ile aerodinamik analizleri yapılarak analiz aracının doğrulama çalışması yapılmıştır. Geliştirilen eniyileme algoritması bir başlangıç geometrisi üzerinde parametrelerin serbest bırakılması koşulu ile doğrulanmıştır. Doğrulama çalışması sonrasında eniyileme algoritması kullanılarak hava alığı tasarım uygulaması yapılmıştır. Eniyileme çalışması sonucunda basınç korunumu katsayısında %6.4 artış, bozuntu katsayısı değerinde ise %45 azalma elde edilmiştir. Elde edilen hava alığı geometrisinin basınç korunumu katsayısı 0.945, SAE standartlarına göre hesaplanan bozuntu katsayısı ise 0.0262 olarak hesaplanmıştır. Öte yandan eniyileme çalışmaları sonucunda hava alığı tasarımının iyileşmesine

bağlı olarak füze toplam eksenel kuvvet katsayısında (C_A) %13 iyileşme elde edilmiştir.

Anahtar Kelimeler: Hava Alığı Tasarımı, Yarı-Gömülü Hava Alığı, Ses-altı Hava Alığı, Füze Hava Alığı, Seyir Füzesi, Basınç Korunumu Katsayısı, Bozuntu Katsayısı, Hava Alığı Optimizasyonu, FloEFD, CFD, PR, DC, Kütle Debisi.

To my marvelous family

ACKNOWLEDGEMENTS

TABLE OF CONTENTS

LIST OF FIGURES

FIGURES

xviii

xix

LIST OF TABLES

TABLES

LIST OF SYMBOLS

A_{th}	Throat Area
AIP	Aerodynamic Interface Plane
k	S-Shape Parameter
D_{aip}	Diameter of AIP
sf	Scale Factor
mtl	Motor Tangent Length
dfl	Diffuser Length
rmpl	Ramp Length
e1	Throat Length.1
e2	Throat Length.2
e3	Throat Length.3
upnt	Upper Lip NACA Type
upnl	Upper Lip Profile Length
lownt	Lower Lip NACA Type
lownl	Lower Lip Profile Length
offset	Length from missile body
Obj	Objective Function Value
α	Angle of Attack (°)
β	Angle of Sideslip (°)
γ	Specific Heat Ratio of Air
ρ	Air density
R	Real Gas Constant
PR	Pressure Recovery Coefficient
DC_{DPCP}	Distortion Coefficient (SAE Standards)
$\dot{m}$	Mass Flow Rate
$\dot{m}_{corr}$	Corrected Mass Flow Rate
PAV	Ring Average Pressure
PAVLOW	Lower Ring Average Pressure
P_0	Total Pressure
P	Static Pressure
T_0	Total Temperature
T	Static Temperature
ref	Sea Level Reference Values

CHAPTER 1

INTRODUCTION

In this thesis subsonic submerged intakes are investigated and a generic submerged intake is generated for design optimization process. Design variables of subsonic-transonic submerged intake are defined in order to implement shape alternations for design optimization. A gradient based optimizer with line search algorithm is employed to obtain better intake designs in design space. The objective function is defined by using Pressure Recovery Coefficient (PR) and Distortion Coefficient (DC). The PR is calculated by FloEFD computational fluid dynamics (CFD) analysis tool that uses Modified k-ε turbulence model. The optimum intake design is achieved after several iterations done by optimization algorithm that uses CFD analysis data. Axial force coefficient is not taken into account as a performance parameter in this study however this coefficient calculated and compared during design optimization iterations.

1.1   Outline of Thesis

After giving general information on air intakes with a greater detail in the concept of submerged intakes, Chapter 2 introduces methodology that is used in this study regarding analysis tool and optimization algorithm. Analysis tool is validated in Chapter 3 by using NASA Flush Mounted S-Duct Intake and NASA S-Shaped Intake diffuser intake test cases. In Chapter 4 benchmark problem of this thesis is described and subsonic-transonic submerged intake parameters are introduced. S-shape design is mentioned in detail additionally. Results and discussion about the work done is introduced in Chapter 5. Conclusion and future work about intake design is given in Chapter 6. Finally references used in this thesis are given at Chapter 7.

1.2 Background

Recent missile technology aims to deliver larger warheads to increased range with high precision. For the long range missions, ballistic missiles have been used since World War 2 and they are still in the inventory of the armies of various countries. Nowadays with the development of technology, the cruise missiles take place of ballistic missiles because of their superiority regarding enhanced performance and cost effectiveness. Several advantages of cruise missiles are realized when they are compared with ballistic missiles such as accuracy, low detectability and effectiveness because of enhanced aerodynamic stability during the missions with various optional launch characteristics. Cruise missiles can be launched from almost all platforms such as aircrafts, ships, submarines and various land based vehicles and installations.

Cruise missiles are guided weapon systems that use aerodynamic forces to maintain their movements on certain altitude consisting of four key components which are airframe, guidance system, payload and propulsion system. If these key components are considered in detail, cruise missiles could be associated with small, pilotless airplanes [1]. Cruise missiles' advanced airframe configurations are designed to meet high aerodynamic performance, such as high lift over drag ratio. Guidance system consists of inertial navigation system, GPS, radio communication systems, radar and infrared seekers, radar altimeters, advanced digital computers and advanced algorithms are utilized on these missiles as subsystems for enhanced navigation, guidance and control characteristics to high accuracy mission achievement [2]. This system should be capable of interfacing with the airframe aerodynamic flight controls [1]. Payload is called as warhead in the missile industry and it generally contains high explosives with different types of explosion activators such as penetration and delayed action impact blasting. Finally propulsion system is a key design parameter for the cruise missiles that specifies the characteristics of the missile and flight envelope. This component is directly related to topic of this study therefore it is investigated in detail. Various engine types have been used for the power supply such as solid-fueled rockets, turbojets, turbofans and ramjets. Surface launched turbo-fan, turbojet and ramjet engines require a solid-fueled booster system to accelerate the airframe to the velocity that it could sustain cruise flight [1].

- Solid-fuelled rocket engine missiles can flight at both subsonic and supersonic speeds but have short range characteristics compared to other types. Their solid fuel requires oxidizer to burn the fuel therefore fuel part of the missile occupy large volume in the airframe and this kind of missile could carry small payloads. At high supersonic flights, atmospheric heating of the solid propellant engine missiles are become critical for stealth characteristics because they could easily detected by IR sensors and have risks to be destroyed by IR-homing air defense missiles. Example: EXOCET

- Turbojet engines use atmospheric oxygen to burn the liquid fuel. This kind of engines produces high thrust levels at certain flight conditions. In order to diffuse the free-stream air into the compressor of the turbojet engine, different types of air intakes are designed and placed on the missile airframe. Currently many of the cruise missiles used in the inventory of the armies are equipped with turbojet engines. Example: C-802 [1]

- Turbofan engines produce higher thrust, are fuel effective and quiet among the other types. This kind of engines resemble to turbojet engine with additional fan upstream of the compressor. Fan forces air into combustion chamber, at the same time some of the air is sent out of combustion chamber and directed to the exhaust stream in order to create additional thrust. Bypassed air also cools the exhaust gases hence reduces the IR radar signature.

- Missiles with ramjet engine are operated at supersonic flow regimes so that an aircraft or a solid propelled booster is needed to accelerate the missile to operating Mach number. Aside from the high speed characteristics of the ramjet propelled missiles there are some disadvantages. Missiles with ramjet engines are heavier than the subsonic flight missiles [1] and are more easily detectable because of supersonic heating. Example: Russian SS-N-22 Sunburn (Moskit) Scramjet engines are in same principle with the ramjet engine missiles and are used frequently.

All propulsion alternatives are mentioned above briefly. Additionally four propulsion alternatives for cruise missile are compared at Table 1-1. The propulsion alternatives are referenced to a 900 kg launch weight missile which is the limit of the carriage of the F-18C.

According to Table 1-1 subsonic cruise with turbojet propulsion is preferred for long range strike against the stationary targets because of superiority at performance characteristics. As it is seen in the table, subsonic cruise with turbojet propulsion has greater range characteristics from the best alternative among the others [3].

Table 1-1 Propulsion Alternatives for Long-Range Precision Strike Missiles [3]

Parameter	Subsonic Turbojet Missile	Liquid Fuel Ramjet Missile	Hydrocarbon Fuel Scramjet Missile	Solid Rocket
Lift/Drag	10	5	3	5
Average Velocity	300 m/sec	1100 m/sec	1800 m/sec	900 m/sec
Fuel/Launch Weight	0.3	0.2	0.1	0.4
Cruise Range	3300 km	1550 km	570 km	470 km

According to Table 1-1 subsonic turbojet engine could be better for long range cruise missile regarding superiority of cruise range and aerodynamic performance such as lift over drag ratio characteristics.

1.3 Air Intakes

Turbojet engines require an air intake to supply its air-breathing propulsion system with the free-stream air in order to burn the fuel at the combustion chamber. The main roles of air intakes are to capture the airflow that the turbojet engines and other conditioning systems needed and slowing the velocity of the air to the level of combustion chamber requires [4]. Engine air intake design is a crucial process for the integration of the turbojet engines within the air vehicles. The aim of the design process of air intakes is twofold [4]. Firstly air intake must supply the engine in order to provide maximum thrust and secondly, air intake should induce minimum drag. Maximum thrust is obtained by minimizing the loss of total pressure by providing efficient transformation dynamic pressure into static pressure throughout the intake. Efficiency is an intake performance parameter that is a ratio of the total pressure at aerodynamic interface plane (AIP) over free-stream total pressure. (Aerodynamic interface plane is an imaginary area which is placed at the intersection of diffuser end and compressor face of the turbojet engine). The uniformity of the total pressure at

AIP also important and it is another design parameter of the intake called total pressure distortion that indicates safe engine operation. These parameters will be mentioned in detail. Minimum drag is obtained by optimal placement of the intake and avoiding the Mach numbers that creates shocks on the lip of the intakes for all certain types of intakes.
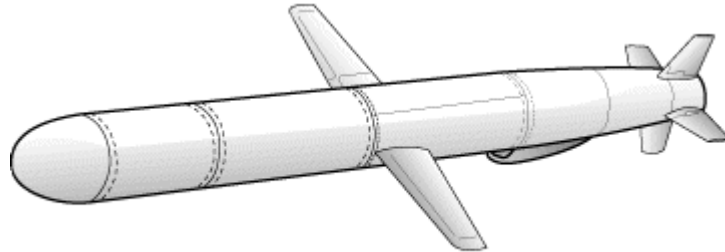
Figure 1-1 Tomahawk Missile with Air Intake

1.3.1   Air Intake Types

In last decades design requirements of the air intakes are changed and became quite challenging by increasing requirements of the stealth technology. Developing aerial defense systems have triggered the attack technology by means of reducing infrared and radar signature of the air attack platforms. In order to reduce the detectability of the cruise missiles, different types of air intake designs come across. In literature air intake types can be separated in different groups according to their integration on missile airframe. In this study air intakes will be investigated in 3 groups as "Pitot type", "NACA type", and "Submerged Air Intake" represented at Table 1-2.

Table 1-2 Subsonic Cruise Missile Intake Types [6]

Pitot Type Air Intake	
NACA-Type Air Intake	
Submerged Air Intake	
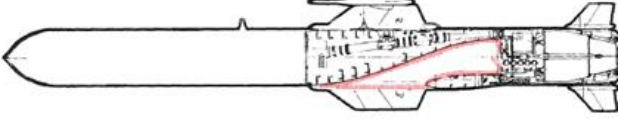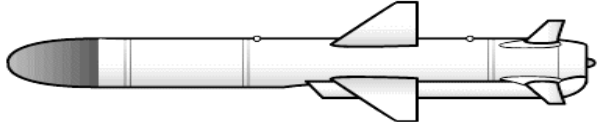
1.3.1.1 Pitot Type Air Intakes

Pitot type air intakes are the simplest air intake type among the other types. The reason why they are called as pitot type is related to integration of the body. This type of intake is placed outside of the geometry and receives the free-stream air flow clearly. There is minimum boundary layer taken inside so that the performance of the intake is not affected from boundary layer and secondary flow development. Also they are not sensitive to angle of attack or yaw angle either [4]. These types of intakes are very common in commercial aircrafts and UAV's because of their ease of design and superior performance. Commercial aircraft engine intakes could be a good example of this type of air intakes.

1.3.1.2 NACA-Type Air Intakes

NACA-type air intakes, represented at Figure 1-2, are developed by National Advisory Committee for Aeronautics at early 1940's. A lot of study and investigation is conducted on this type of intake between 1940 and 1960 and this intake have been widely used in both automobile and aircraft industries because of its low drag characteristics on air conditioning, ventilation and cooling systems (Airbus A320) [5].

6

Figure 1-2 NACA-type Air Intake [5]

NACA-type air intakes are flush with the airframe with a trapezoidal opening and sharp lateral edges that generate two counter-rotating vortices [5]. The key advantage of these counter-rotating vortices is while they entering in the intake, they are energizing the boundary layer with the lower energy and avoid inflow against the separation. Also, because of their shape and integration to the airframe they have low drag, low distortion and low radar cross-section (RCS). Drawbacks of this type of intakes are taking up too much internal space and lower efficiency because of large amount of boundary layer ingestion.

1.3.1.3 Submerged Air Intakes

Submerged intakes, the focus of interest of this thesis, resemble to NACA-type intake on the aspect of shape and integration. The experience and inspiration of development of submerged intake topology comes from the auxiliary air intakes that are developed for satisfying the requirements air ventilation or cooling system. Due to great contribution potential to the aircraft performance such as lowering system weight, reducing RCS, reducing aerodynamic drag and reducing risk of foreign object damage (FOD) to engine components, submerged intake has been of interest to aeronautical community since it was first developed. Well-designed submerged intake could yield improvements including increased range and engine reliability, reduced fuel consumption and reduced observability of the cruise missile. When taking into account military constraints regarding radar and infrared signature that increase observability of the missile and the aspect of aerodynamic performance such as pressure recovery and flow uniformity upstream on the AIP, the submerged intakes have greater advantages among the other intake topologies. Therefore this study is concentrated on this type of air intake design for modern-day cruise missiles.
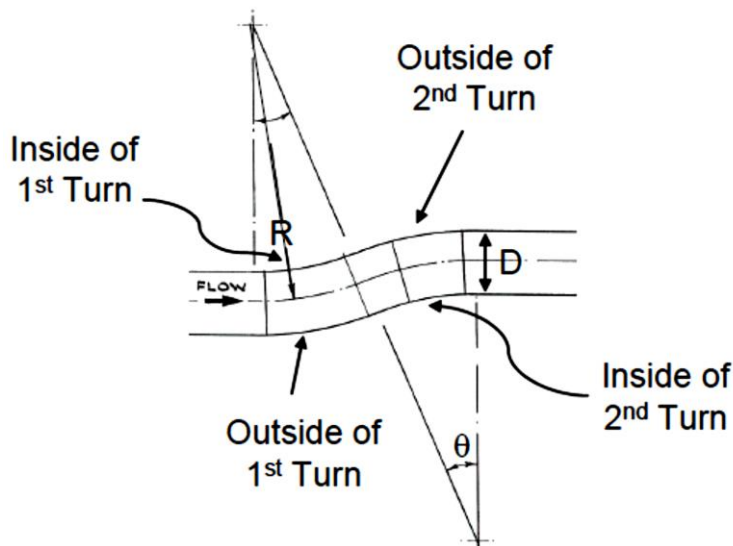
Figure 1-3 Representative S-Duct [7]

Submerged air intakes consist of short S-shaped duct, also known as serpentine duct in literature, and a lip. S-shaped duct is used to save installation space in the missile airframe and a lip is used for taking air into the duct. Short S-shaped duct geometry brings some drawbacks such as flow separation and boundary layer growth due to strong curvatures and bending. Eventually total pressure of the air intake is reduced. These geometric topologies could also trigger the secondary flow development in the S-duct that diminishes the efficiency of the intake. On the other hand short S-duct affects total pressure uniformity of the inflow in the S-duct throughout the AIP so that engine stability could be affected because of high distortion effect.
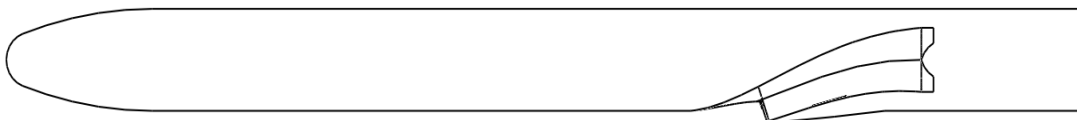
Figure 1-4 Representative Submerged S-duct Intake on Cruise Missile Body

Although submerged intakes ingests large amount of boundary layer and that could affect the overall missile performance, stealth characteristics such as low observability and high survivability, lower weight specialty and lower drag characteristics make these intake topologies the best choice for the modern–day cruise missile. Because of the advantages of the submerged intake, this study is concentrated on this type of air intake design and optimization for subsonic-transonic cruise missile.

8

1.3.2   Intake Performance Parameters

Mass flow rate, pressure recovery coefficient and distortion coefficient are the most common parameters that define the intake performance and stability. Some brief information and basic formulas are given below to describe intake performance parameters.

1.3.2.1   Pressure Recovery Coefficient (PR)

Pressure recovery is the most common and significant parameter in the design process of turbojet and turbofan engine intakes. PR is a representation of efficiency for intakes. Intake transports the air from free-stream to aerodynamic interface plane and reduces the velocity of the air along the intake. Thus pressure recovery defined as the ratio of total pressure of AIP to free-stream total pressure. For an efficient intake, the total pressure recovery should be as high as possible [8]. Furthermore pressure recovery affects the thrust and stability of the engine compressor [9] directly. This coefficient is the primary objective that is handled to improve in intake design process. PR will be calculated as given Equation 1.1.

$$PR = \frac{P_{t,AIP}}{P_t} \tag{1.1}$$

1.3.2.2   Mass Flow Rate

Mass flow rate is another major performance parameter for intake performance that defines amount of mass flow entering the intake per second. This parameter varies according to type of turbojet or turbofan engine for each flight condition. Mass flow rate can be stated as follows;

$$\dot{m} = \rho * V * A \tag{1.2}$$

Mass flow rate on AIP can also be defined as;

$$\dot{m}_{AIP} = \frac{P_{t,AIP}}{\sqrt{T_{t,AIP}}} * A_{AIP} * \sqrt{\frac{\gamma}{R}} \, M_{AIP} * \left(1 + \frac{\gamma-1}{2} * M_{AIP}{}^2\right)^{\frac{-(\gamma+1)}{2(\gamma-1)}} \tag{1.3}$$

1.3.2.3 Corrected Mass Flow Rate

In order to compare mass flow rate parameter for different flight conditions and different ambient conditions, corrected value of mass flow rate parameter is required for design process [10]. Total pressure and total temperature values are non-dimensionalized with the sea level static pressure and temperature. Corrected mass flow rate can be defined as;

$$\dot{m}_{corr} = \dot{m} * \frac{\sqrt{\dfrac{T_t}{T_{sea\ level}}}}{\dfrac{P_t}{P_{sea\ level}}} \tag{1.4}$$

1.3.2.4 Distortion Coefficient (DC)

Total pressure variation across the engine face is described as flow distortion and it can be steady or time variant [8]. This parameter identifies the flow uniformity on the engine face. Thus distortion coefficient is used to measure the quality of flow inside the intake [11]. After designing the intake duct wind tunnel testing is generally required to inspect the air flow characteristics on the engine face. According to these tests engine manufacturers evaluate the effect of distortion to performance and stability of the engine for various flight conditions [12]. High levels of distortion coefficient means non-uniform pressure load on the compressor blades that can affect the compressor blade stability and it can also cause aerodynamic stall of the engine called surge. Effects of distortions can be investigated under different topics such as aeromechanical, stability, operability, and acoustic problems for the turbojet engine. The compatibility of the engine with the inflow conditions is ensured when certain distortion requirements at the AIP are met [13]. In most cases engine manufacturers develop their own distortion coefficient calculations in order to determine the intake characteristics before the intake/engine compatibility wind tunnel tests.

As it was mentioned before, different engine manufacturers use various distortion coefficient descriptors. The aim of the distortion descriptors is to generate universal definition about distortion of the flow on the AIP. Designers use one of these descriptors determined by the engine manufacturer in design process. Commonly used DC descriptors are mentioned below.

1.3.2.4.1 The SAE Circumferential Distortion Descriptor (DC$_{\text{DPCP}}$)

Distortion descriptor obtained from 40 data points on 5 concentric rings on the AIP. This descriptor defined by intensity and extent parameters that obtained from each ring. Rings and data points are represented in Figure 1-5. Rings are numbered 1 to 5 from inner to outer respectively. Extent and intensity parameters are described in detail below.
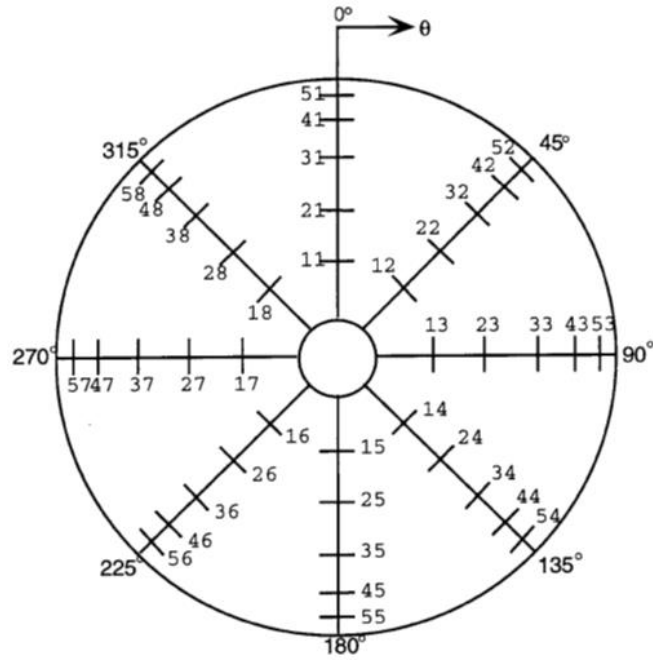
Figure 1-5 SAE Probe Orientation of AIP [14]

The extent parameter for each ring θ_i^- is the region in degrees in which the total pressure is below the average ring total pressure. The extent of the circumferential distortion is given as;

$$Extent = \theta_i^- = \theta_{2_i} - \theta_{1_i} \tag{1.5}$$

11
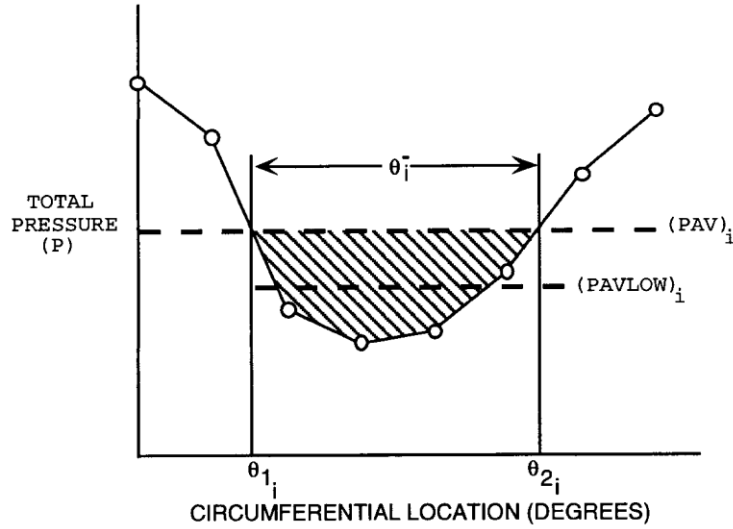
Figure 1-6 Ring Circumferential Distortion for a One-Per-Rev Pattern [14]

Intensity parameter describes the magnitude of the total pressure deviation from the ring average for each ring. According to the SAE [14] the circumferential distortion intensity for the ith ring is calculated by;

$$Intensity = \frac{(PAV)_i - (PAVLOW)_i}{(PAV)_i} \tag{1.6}$$

Where;

Ring average total pressure;

$$(PAV)_i = \frac{1}{360} \int_0^{360} P(\theta)_i d\theta \tag{1.7}$$

Ring average low total pressure;

$$(PAVLOW)_i = \frac{1}{\theta_i^-} \sum_{k=1}^{K} \int P(\theta)_i d\theta \tag{1.8}$$

The DPCP can be described as the average of the ring distortion intensities. According to Tournier and Paduano the SAE distortion descriptor DPCP is acceptable under 0.05 [15].

12

1.3.2.4.2 DC(60)

DC(60) parameter is one of the common distortion descriptor that intake and engine designers considered in their designs. This distortion parameter introduced by Rolls Royce Engine Company and used in the European Fighter Programs Tornado and Eurofighter [16]. DC(60) parameter can be also used as DC(90), DC(120) etc. for different engine manufacturers but DC(60) is used extensively in the past design studies. This descriptor calculates the flow distortion by determining the deviation of the minimum averaged total pressure over any 60° slice of the AIP from average total pressure over entire AIP area.

General equation of DC(60) is;

$$DC(60) = \frac{\overline{P_{t,AIP}} - \overline{P_{t,\theta}}}{\overline{q_{AIP}}} \tag{1.9}$$

Where $\overline{P_{t,\theta}}$ is the minimum of mean total pressures obtained from each 60° pieces over the AIP.

In this study AIP section is divided into 24 equivalent slices for DC(60) calculations represented in Figure 1-7
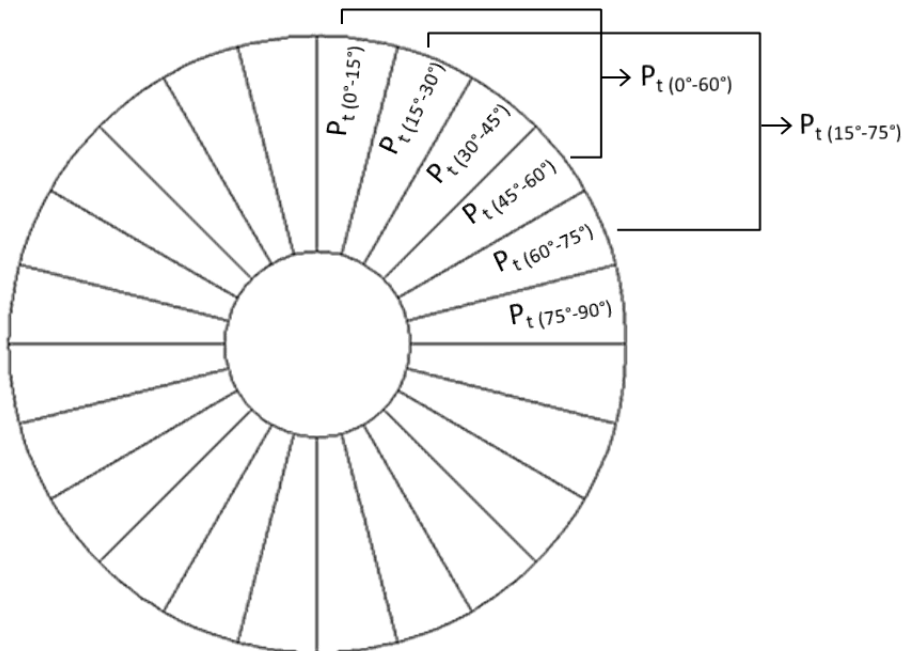
Figure 1-7 15°-Slices and 60°-Pieces on AIP

13

For calculation of DC(60); First, area weighted average of total pressure of each 15°-slice (Pt (0°-15°), Pt (15°-30°), Pt (30°-45°), … , Pt (345°-360°)) is obtained. Then the average total pressure is calculated for each 60°-slice. (PT (0°-60°), Pt (15°-75°), Pt (30°-90°), …, Pt(345°-45°)). The minimum average total pressure among the 60°-slices (Pt,min) is used for DC60 calculation. DC60 is the absolute value of difference between the minimum average total pressure (Pt,min) and the average total pressure of 15°-slices (Pt,ave) divided by the average dynamic pressure on AIP.

$$DC(60) = \frac{abs\left(P_{t,min} - P_{t,ave}\right)}{q_{AIP}} \tag{1.10}$$

The last 60°-piece (Pt (345°-45°)) is the average of total pressures of the 15°-slices of Pt (345°-360°), Pt (0°-15°), Pt (15°-30°), Pt (30°-45°).

According to Kyungjae et al. [12], DC(60) distortion descriptor limits are tabulated at Table 1-3 below.

Table 1-3 The Limit of DC(60) for various Engine [12]

Civil Subsonic Transport	0.2
Military Fighter Aircraft	0.9
Industrial, Marine and Automotive Engine	< 0.1

In this study DPCP and DC(60) limits are determined as 0.05 and 0.2 respectively.

14

1.4   Shape Optimization for Submerged Intake Design

In engineering design problems optimization algorithms are widely used in order to reach an optimum design by considering design limits and variables. There are various methods available for design optimization process, each one keeps back of its own advantages and disadvantages depending on the structure of the design problem. Gradient based and stochastic methods are both used in literature for design problems. Gradient based optimization methods could be risky because of the nature of the algorithm; solution can converge in a local optimum rather than reaching the global optimum [17]. Furthermore convergence in these algorithms is highly influenced by starting point. In contrast, stochastic methods contain degree of randomness in order to avoid convergence to local optimum and these methods less dependency to starting points then gradient methods. Nevertheless stochastic methods require more iterations than gradient based optimization techniques. Optimization technique is selected from these alternatives according to complexity of the geometry and considering design analysis tool time for each design iteration step. It is concluded that gradient based optimization method is the most suitable one by taking into account the simulation time of high accuracy CFD tools and the starting point of optimization which is considered to be near the global optimum. For design optimization problems, a design objective function is determined according to goals of the design problem. Optimization problems can use more than one objective are commonly known as multi-objective optimization problems such as maximizing one design goal while minimizing other design goal. Moreover, the limits of the design variables can be introduced as penalty values during optimization process in order to avoid time expending out of design limits.

For intake design optimization studies in literature; pressure recovery (PR) and distortion coefficient (DC) are commonly used as objective parameters.

In this study, gradient based optimization method steepest descent algorithm is used in conjunction with line search algorithm for improved convergence. Single performance parameter PR considered as design objective to maximize.

1.5   Intake Design Improvement

There are several methods used to improve intake performance by minimizing flow non-uniformity. Methods are utilized for avoiding effects of boundary layer from the intake entrance. Numerous works are done in order to control the boundary layer to improve intake design considering flow distortion and PR for intake designs. Active and passive flow control schemes are employed to enrich flow properties at AIP. Active control schemes consist of blowing and suction mechanisms, passive flow control elements are vortex generators. Works done by the scientists in order to understand the effects of boundary layer and flow control mechanisms to improve intake performance are mentioned below.

Rabe [18] conducted experimental investigation in a static ground test facility to determine the flow quality of a serpentine intake duct integrated with active flow control for several simulated flight conditions. The intake duct and air injection system are both developed by Lockheed Martin. Intake is examined in the ground tests at throat Mach number 0.55. According to wind tunnel tests active flow control is found that it improves the flow uniformity and decrease the distortion of the intake on AIP at each flight condition. At on design flight conditions, by the addition of air flow control, the total pressure recovery is increased 2 percent and maximum circumferential distortion is decreased 70 percent. At the off-design flight conditions the total pressure recovery is increased about 1.5% and 2% and maximum circumferential distortion is decreased about 30%-40% respectively. Devine et al. [19] investigated the performance improvement of the vortex generator (VG) control on the flush, parallel walled auxiliary intake by performing numerical analysis and experimental tests. Their measurements and calculations indicated a performance enhancement of between 35% and 40% as a result of the application of the vortex generators. Allan and Owens [20] conducted validation of NASA developed RANS flow solver OVERFLOW for a boundary layer ingesting intake in high subsonic flow regime with passive and active flow control devices. Passive vane flow control and active mass injection flow control methods are investigated in this work. Boundary layer diverters and boundary layer suction methods are employed in order to increase performance of the intake. Nichols and Pierpont [21] conducted experimental investigation on boundary layer suction slots placed upstream submerged intakes.

They examined effect of the boundary layer suction slots quantity and placement, on the intake performance. According to experimental tests, boundary layer control increased the pressure recovery of submerged intake. Pierpont and Howell [22] also handled experimental investigation of boundary layer suction slots for semi-submerged air scoop at low speeds. As their study boundary layer suction slots increase the PR of the intake, but position of the suction slot is not found as critical. Area of the suction is effective for the intake performance according to their work.

It can be stated that from the past investigations and works about performance improvements, different methods are held and become successful enhancement of performance.

1.6   Literature Survey

For this research paper, books and reports are covered create background information about the topic. Related works about the topic focus on different aspects and have different motivations. All of these studies helped to get broad range of background information. Some selected studies related to the subject are covered well and all these priceless works are mentioned below.

At the earlier 1940's researchers directed their interest about NACA-type flush intakes was leaded by National Advisory Committee for Aeronautics (NACA). Rogallo [23] investigated internal flow systems of aircrafts and its efficient arrangements. His works comprised wind tunnel tests of intake and outlet openings in a flat plate and in a wing. He represents design recommendations about intake openings, ducts and outlet openings for typical aircrafts. Some years after investigations about the concept of submerged intake, at the end of 1945's lots of experimental works are conducted by the researchers of NACA simultaneously. NACA-type flush intake which is still used nowadays had been designed and experimental works focused on design parameters (lip, ramp and diffuser) of this kind of intake, intake entrance and placement on the aircrafts. All experimental works had been done for understanding internal flow phenomena and design problems. Frick et al. [24] introduced NACA-type submerged intake and published a report about their experimental study based on this intake at the end of 1945. Their aim is investigation of the submerged intakes which are placed below the surface of aircraft body. According to their work this kind of intake has some advantages such

as reduction of the internal duct weight, reduction in pressure losses and external drag compared to other kinds and easier attainment of high critical speeds attitude of the airplane. The experimental investigation focused on ramp design, lip design, entrance shape, entrance aspect ratio and boundary layer thickness. All these intake parameters and their effects on the intake performance are discussed and valuable data are generated and represented for future intake designers. In this same context Mossman and Randall [25] investigated primary design variables of NACA submerged intake duct. They condensed their experimental work on; entrance width to depth ratio, ramp wall divergence, ramp angle and deflector size. Furthermore they presented effect of boundary layer thickness on the intake performance.

Effects of the side walls are also significant parameter on the NACA-type intakes performance hence some experimental comparisons had conducted by the engineers of NACA. Delany [26] conducted an experimental study on 1/4 scale model of a typical fighter airplane in order to determine the effect of submerged intake walls on intake performance. According to experimental results the submerged intake with parallel walls are less acceptable then the submerged intakes with divergent walls for a typical fighter aircraft. He also discussed the place that submerged intake should be placed on the fuselage. Mossman [27] investigated the side-wall effects on submerged intake performance at subsonic and transonic speeds. According to his experimental work divergent-walled intakes are more satisfactory than parallel-walled ones for all Mach regimes. Similar experimental work had done about design of the side-walls for a NACA-type subsonic intake for transonic speeds represented by Taylor [28]. Martin and Holzhauser [29] also conducted NACA submerged air intake investigation on a full-scale model of fighter airplane in order to determine the effect of ramp divergence on pressure recovery.

On the other hand effects of the flow conditions and properties on pressure recovery of the S-duct intakes are also examined by the researchers. Hall and Frank [30] undertake the experimental investigation about the effects of Mach number, angle of attack, entrance mass flow, boundary layer thickness and intake location on the submerged intake performance.

Furthermore some works conducted on submerged intakes at different Mach regimes. Transonic speeds and high subsonic speeds experimental investigations were

undertaken to comprehend the submerged intake behavior at different Mach regimes in references [31, 32, 33].

Besides the all experimental works, flight tests were also conducted on two different intake configurations for investigation of the differences between submerged intakes and NACA-type flush intakes. Rolls [34] installed a submerged intake and a NACA-type intake on an YF-93 plane and flight test were conducted in 1953. Total pressure recoveries and total airplane drag were measured for each configuration. According to the flight tests submerged intake had higher pressure recoveries all over the most Mach regimes but also had higher drag than NACA-type intake.

Placement of the intakes on the aircraft body is also taken interests of the scientists. They had directed their focuses on the placement of the intake on the aircraft after determining intake design parameters. NACA submerged intake is investigated in order to place it right region on the fighter body to make it more efficient by Gault [35]. Hall and Barclay [36] also conducted experimental study at same years about the submerged intakes placed forward of the leading edge of the wing for high subsonic speeds. They also investigated boundary layer thickness, deflectors and intake lip angle on the intake performance.

Besides all these experimental works theoretical studies were also done for the submerged intakes. Sacks and Spreiter [37] theoretically investigated submerged intakes at low speeds. They governed equations for determining laminar and turbulent boundary layer growth along the parallel, convergent and divergent ramp for the submerged intake. Growth of the boundary layer for divergent ramp intake is retarded compared to others. Effects of vortex formations and mass flow ratio are also discussed regarding the supporting equations. On the other hand the effect of lip geometry on subsonic intake determined theoretically incompressible potential flow calculations corrected for compressibility by Albers and Miller [38].

By increasing mastery of knowledge about submerged intakes, some optimization works had done by the scientists. Luidens et al. [39] studied on the finding optimum subsonic intake design regarding the earlier investigations about subsonic intakes. They determined the typical V/STOL aircraft intake operating conditions and choose the critical operating conditions among the others and presented a design method by

taking into consideration of important design parameters such as intake lip and diffuser.

Relation between pressure recovery and thrust is used to be an attractive subject for intake designers. On this subject Hanson and Mossman [40] investigated the effect of the pressure recovery on the performance of a typical jet engine and typical jet-propelled fighter aircraft. They introduced the ram recovery ratio which is the ratio of the impact pressure recovered to the impact pressure available indicates the efficiency of the air induction system. The effect of ram-recovery ratio on the net thrust and on the specific fuel consumption of a turbojet engine is calculated for various speeds and for altitudes. According to the study increase of 28 percent in ram-recovery, result 18.9 percent increase in net thrust and 9.5 percent decrease in specific fuel consumption.

At the end of 1970's, with the development of the computer technologies computational studies have been become widespread, and commercial CFD tools have been started to use to solve fluid dynamics problems. Expensive and exhaustive experimental works give way to cost friendly CFD analysis among the designers. Nowadays CFD tools are more popular in the subject of intake design works and numerical analyses make it easy to find a design solution for submerged intakes. He and Li [41] researched the influence of the centerline and the cross–section variation on aerodynamic performance of submerged intake numerically by using commercial numerical simulation software CFX. Their aim is designing an intake meets the needs of stable flight of loitering aircraft that has a total pressure recovery 93.2% and total pressure distortion coefficient is 1.2% by optimizing centerline S-shape. In the same context, Lee, Jung and Ahn [42] are also investigated the effects of some design parameters of three dimensional flush intake performances numerically by using commercial CFD code. They handled the pressure recovery at the intake exit plane though numerical analyses of 3D turbulent flow by changing ramp angle, width of throat and effects of mass flow rate and angle of attack.

In 1993 Wellborun and Okiishi [7] generated aerodynamic data for compressible S-duct intake configuration. They conducted experimental tests and numerical solutions to understand flow phenomena in S-duct intakes and validate the computational codes. Numerical solutions are obtained by using parabolized Navier-

Stokes equations. The aim of this study is to provide benefits to aircraft intake designers by presenting validated computational works with experimental test data. Secondary flows in the S-duct intake are also aimed to be investigated in this work. With using same S-Duct intake Vuillerme and Deck [43] conducted numerical studies by developing numerical methodologies and using various turbulence modelling. Generated data are compared with available experimental data presented by Wellburn and Okiishi. This experimental and numerical data is used in my thesis as a validation study of employed CFD tool FloEFD. Similarly, Berrier et al. [44] conducted an experimental research of a flush-mounted, S-duct intake that ingesting large amounts of boundary layer. In addition to experimental study, they managed computational studies of this intake by using Navier-Stokes solver OVERFLOW to direct their aim to present a database for CFD tool validation on this type of intake and provide a baseline intake for future intake flow control studies. This valuable work is also used in my thesis as a test case to validate employed CFD tool FloEFD. Sun, Guo and Wu [45] worked to enhance submerged intake performance with flush mounted planar side entrance. They determined three significant parameters side edge angle, ramp angle and parameter of aft lip and they studied the effects of these parameters on the intake performance by both experiment and computational fluid dynamics in 2007. Leoper and King are also studied the effects of five different parameters of S-duct intake on its performance numerically such as duct length, vertical offset distance, expansion ratio of the cross-sectional area, aspect ratio of elliptical entry and Mach number at entry [46].

As computer technologies are developed and become widespread optimization procedures are integrated with computational study works. Zhang et. al. [47] studied design of S-shaped intake by using multi-objective and multidisciplinary techniques. They parameterized the S-shaped intake and aerodynamically improved this baseline intake by integrating CFD computations with mathematical optimization methods. Similarly [48] Reddy found optimum S-shaped intake design working on design optimization of a subsonic intake by changing lip shape parameters, using Automated Design Synthesis code that is interfaced with CFD solver and grid generation code. Taskinoglu and Knight [49] [17] studied on multi-objective optimization of generic submerged intake for ultimate purposes by performing

computational analyses. The objective functions of the optimization problem were distortion and swirl indices over the exit cross-section of the subsonic submerged air vehicle intake. Geometrical parameters were chosen fin height, length and incidence angle of placed on the baseline intake surface.

CHAPTER 2

METHODOLOGY

In this chapter design methodology, optimization process and used optimization algorithm will be described. Firstly CFD analysis tool FloEFD and solution approach will be introduced. After description of the CFD tool, optimization algorithm will be explained. Finally, flow chart of the design and optimization algorithm will be represented.

2.1   Analysis Tool

In this study a commercial CAD-embedded CFD solver FloEFD software is used for computational fluid dynamics analyses. FloEFD is capable of solving compressible, incompressible fluid flow and heat transfer equations by using Cartesian mesh based on octree technology combined with a unique immersed boundary approach for wall friction and heat transfer [50]. Octree algorithm approach refines the generated initial mesh according to criteria set by increasing the precision of refinement in order to capture the solid model. This process stops the mesh refinement automatically once the mesh is locally fine enough to capture the fluid solid interaction region to solve the fluid dynamics problem. FloEFD also uses solution adaptive refinement (SAR) to optimize the mesh density in order to minimize solution error arising from discretization of governing differential equations. In Figure 2-1 adaptive mesh refinement process for a generic submerged inlet is presented from initial to denser mesh.
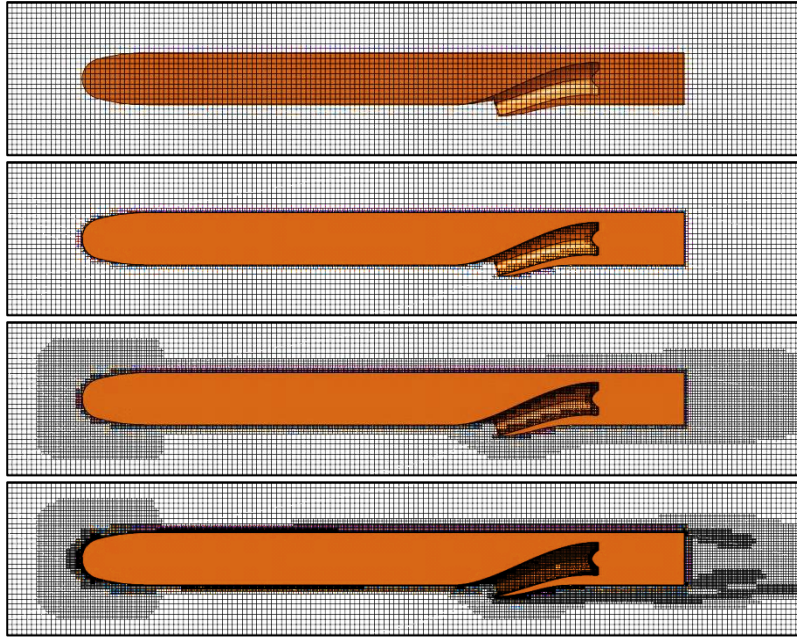
Figure 2-1 Adaptive Mesh Refinements of a Generic Subsonic Intake (Coarse to Dense Mesh)

In FloEFD Van Driest's turbulent boundary layer profiles are utilized and two methods are developed (Two-Scale Wall Functions) to simulate the boundary layer profile of fluids relative to free-stream flow properties [51]. Thin and thick boundary layer approach is used to solve flow properties near the solid wall. Use of Two-Scale Wall Function treatment technique depends on whether boundary layer is thin or thick compared to cell size near the wall [50]. This technique simplifies the mesh generation and diminishes the total number of cells.

Modified k-ε turbulence model is used with additional empirical improvements that cover wide range of industrial flow applications. This turbulence model allows calculation of the transition laminar to turbulent automatically.

Cartesian mesh Navier-Stokes solver with enhanced wall treatment and improved k-ε turbulence model work each other within the FloEFD successfully and makes it different against the other commercial solvers. Developers of FloEFD call this combination of algorithm "Enhanced Turbulence Modelling" structure illustrated in Figure 2-2 [51].
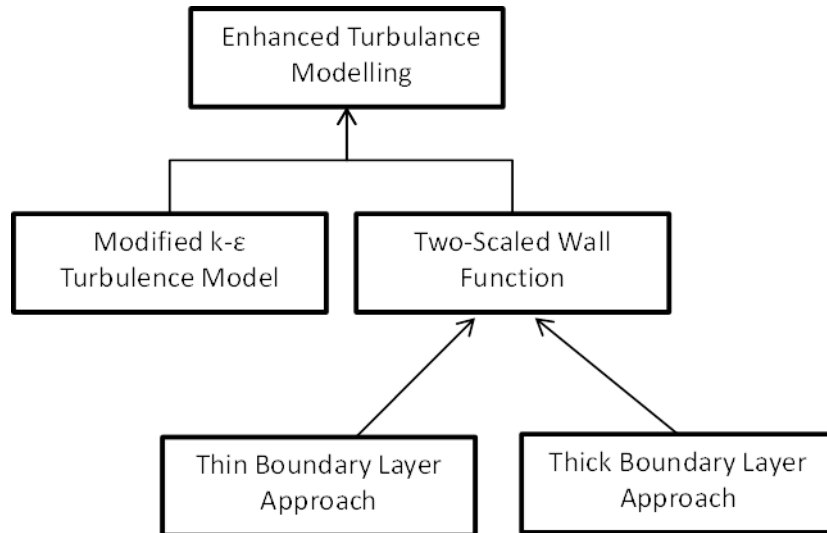
Figure 2-2 Enhanced Turbulence Modelling Structure of FloEFD [51]

FloEFD software is chosen for this study because it has several advantages regarding easiness to work with CAD models, short mesh generation time, fast convergence and solution adaptive refinement. FloEFD does not require any surface meshing so that it is easy to work with multiple geometries with small differences between each other. Also, mesh adaptation algorithm refines and coarsens the grid regarding the converging solution in order to obtain accurate flow field solution without increasing computational load. In this study, an initial Cartesian mesh is generated and its grid generation options are preserved for the remaining geometries during optimization process. So, meshes generated for all of the geometries during the optimization process can be considered as having same quality. Working with multiple geometries by preserving same mesh options reduces the pre-processing time for the optimization process.

2.2 Optimization Algorithm

In this study, a method is developed to maximize PR of subsonic cruise missile intake by using steepest descent optimization method with line search algorithm. Pressure recovery coefficient is used for determining objective function of S-duct intake optimization. As it mentioned in Chapter 1, distortion coefficient is a requirement for engine operation given by engine manufacturer. Acceptable levels of static distortion values are generally considered below about 0.05 [14] according to SAE circumferential distortion descriptor standards [44]. Regarding to this

information; distortion coefficient levels above 0.05, introduced as a penalty value for the optimization process.

2.2.1 Objective Function

Optimization can be defined as finding the best design solution among the design alternatives. In order to determine how good the solution is, the objective function that relates design variables to assess the value of the solution must be obtained. In most of the engineering problems, it is very difficult to determine the objective function directly. Some analysis software or fast prediction tools generally used to calculate objective function as a bridge between design tool and optimization algorithm in design process. In this study, CFD tool calculates the pressure recovery coefficient that will be used for calculation of the objective function.

In general objective function is calculated by weighted sum of multiple objectives;

$$f(\vec{X}) = \sum_{i=1}^{n} w_i . f_i(\vec{X}) \tag{2.1}$$

where $\vec{X}$ is the variable vector, w_i is the weight factor of the objective i.

Penalty value is added to objective value when performance and design variable constraints are violated. Penalty value is given to DC parameter in order to limit the value below 0.05.

2.3 Steepest Descent and Line Search Optimization Algorithm

Steepest descent method is used in this study which uses derivative information to search optimum value and line search optimization method is used for enhancement of optimization efficiency and fast convergence characteristics.

First, gradient of the objective function is calculated by changing each design variables by small amounts while other variables remain constant for each optimization step. The amount of change should be suitable for grid size and sensitivity of the analysis tool. Secondly, new geometric variables are found by calculating gradients of each design parameter.

Gradient of the objective function at the iteration i given as;

$$G^i = -\nabla F(X^i) \tag{2.2}$$

Variables at the all geometric iterations i, are summed by gradient times scaling factor by summing the variables with the scale factor (*sf*) is called line search algorithm.

Gradient of the objective function at iteration i is calculated as;

$$X^{i+1} \leftarrow X^i + sf * G^i \tag{2.3}$$

Simple line search algorithm is the method of finding sf that minimize;

$$F(X^i + sf * G^i) \tag{2.4}$$

Line search algorithm is employed to improve convergence time and find the optimum scaling factor for the design variables at each optimization step. Scaling factors are calculated by using line search algorithm and generates new geometry in order to gradient calculations for next step again.
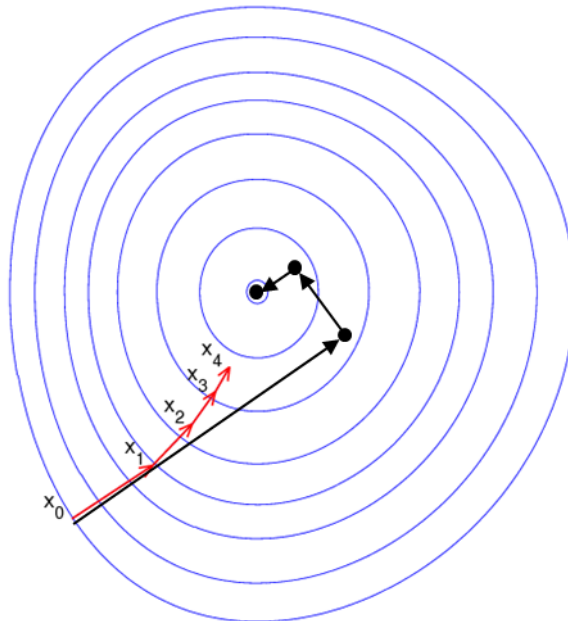
Figure 2-3 Gradient Based and Line Search Algorithm

Gradient based method converges nearest optimum and for this study it can be assumed that there is only one optimum near the initial point which is also global optimum. Although CFD simulations have high computational cost, overall optimization time is reduced by employing steepest descent gradient method which requires less number of iterations compared to other methods.

2.4   Design Study Flow Chart

Flow chart of design optimization study is given in Figure 2-4. Model preparation for CFD analysis and shape optimization process given step by step in flow chart.
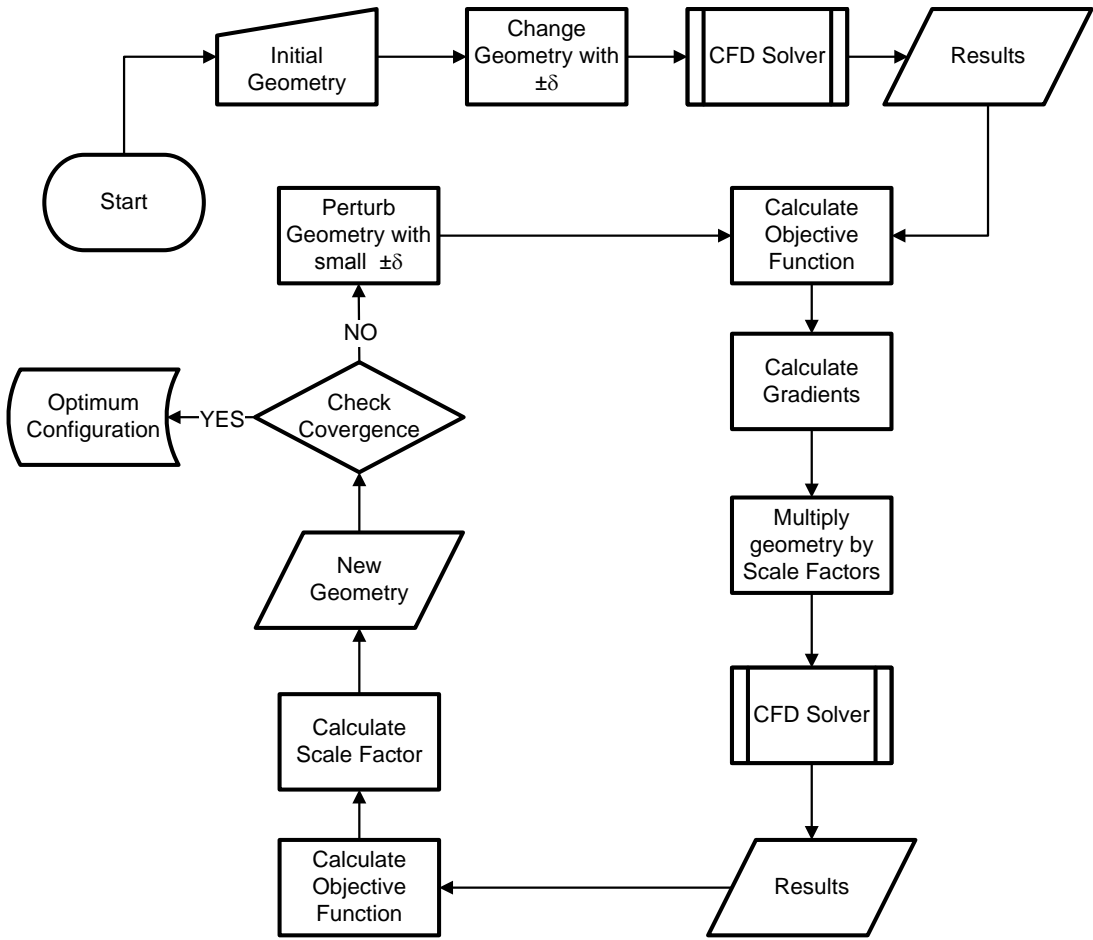
Figure 2-4 Problem Solution Flowchart

CHAPTER 3

CFD TOOL VALIDATION STUDIES

3.1 NASA FLUSH MOUNTED S-DUCT INTAKE TEST CASE

3.1.1 Introduction

This validation study based on an experimental investigation of flush mounted, S-duct intake with large amount of boundary layer ingestion [44]. Reference wind tunnel tests were performed in the NASA Langley Research Center 0.3 Meter Cryogenic Tunnel. Present study CFD analysis of a baseline intake is performed by using FloEFD version 12 commercial CFD tool. Results of the present study are compared with experimental wind tunnel test data and additional CFD study of "*OVERFLOW.*" The results of commercial CFD tool are presented and compared with the reference data.

3.1.2 Reference Experimental Work

The experimental study is performed in the NASA Langley Research Center 0.3 Meter Cryogenic Tunnel. Intake tests are held to; build up a new high Reynolds number intake test capability for flush-mounted intakes, to create database for CFD tool validation, review the performance of S-duct intakes, provide a baseline intake for future designs works [44]. Thanks to this reference study that creates great chance to validate CFD software and to builds a great design background for my thesis.

3.1.3 Geometry Description

For experimental study; Boeing Company designed four flush mounted S-duct intake models denoted Inlet-A, B, C and D. These intakes are designed for integrating large blended wing body transport aircraft as well as fighter type military aircrafts with

flush-mounted intakes. Intakes were mounted on the wind tunnel wall in order to simulate a boundary layer development upstream of the intake duct. Based on the intake height approximately 30 percent boundary layer ingestion occurs on a typical blended wing body transport aircraft [44]. Predicted boundary layer height (δ_{est}) is given as 0.501 in.

The flush mounted intake geometry is presented in Figure 3-1, Figure 3-2 and wind model of Inlet-A presented at Figure 3-1Figure 3-3.

Variable	Inlet A
H_{max}, in.	2.185
L, in.	7.697
L + a, in.	8.174
a, in.	0.477
b, in.	0.239
a/D_2	0.195
H_i, in.	1.703
W_i, in.	3.249
A_i, in^2	4.400
A_C, in^2	5.760
ΔH, in.	2.543
D_2, in.	2.448
A_2, in^2	4.707
L/D_2	3.144
$\Delta H/L$	0.330
A_2/A_i	1.070
$W_i/2H_i$ or AR	0.95
a/b	2.0
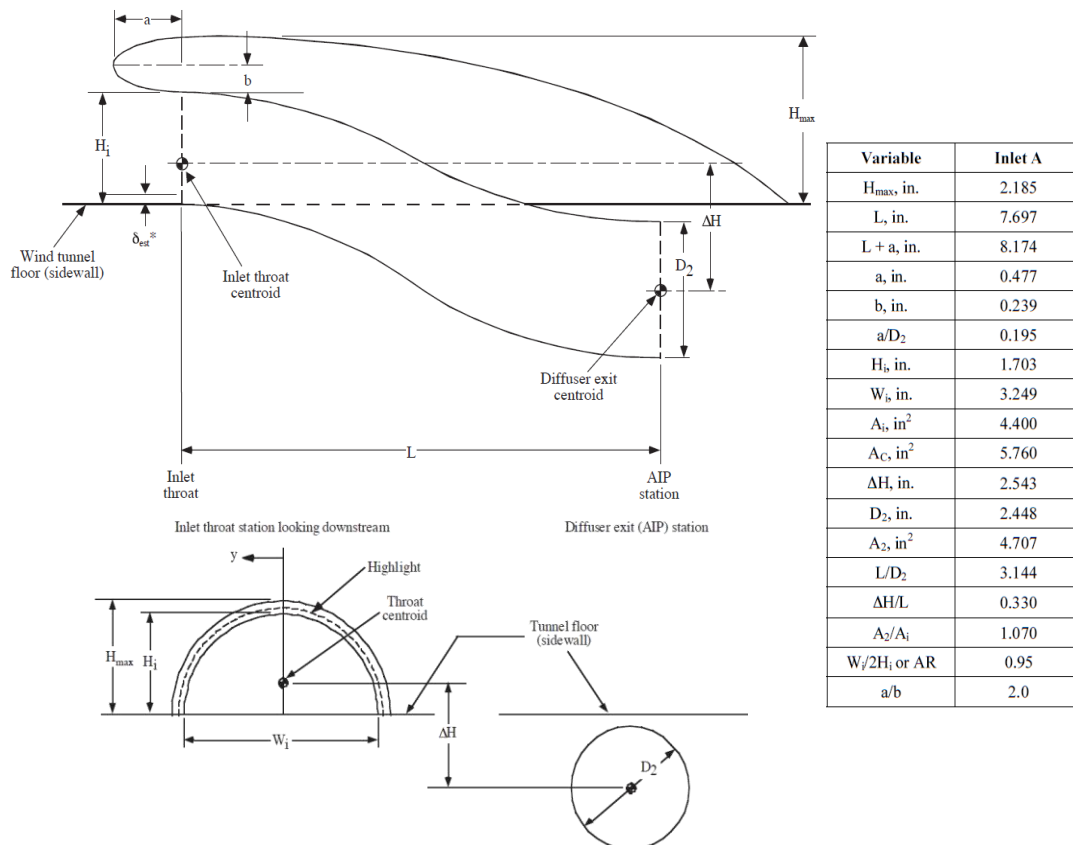
Figure 3-1 Inlet-A Geometry Description and Dimensions [44]
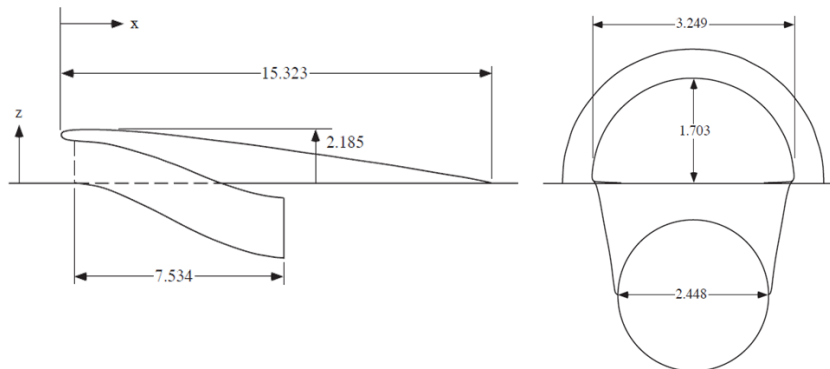
Figure 3-2 Continued [44]
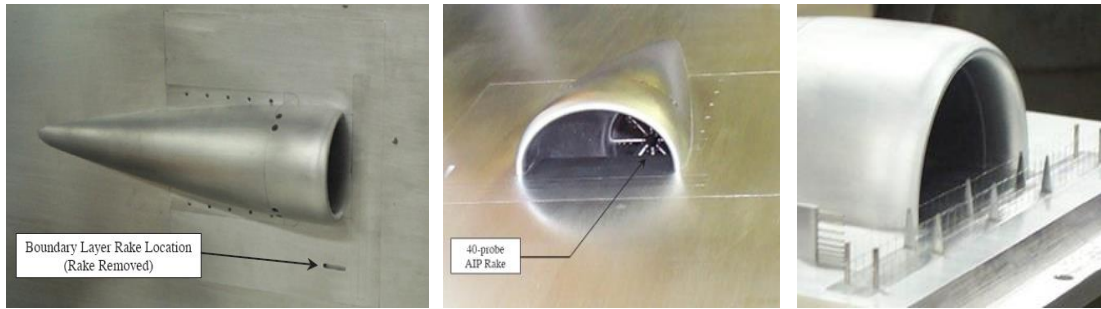
Figure 3-3 NASA Langley Intake-A Wind Tunnel Model [44]

Inlet-A S-duct is built by lofting 16 sections, given details below in the graphs in Figure 3-4.
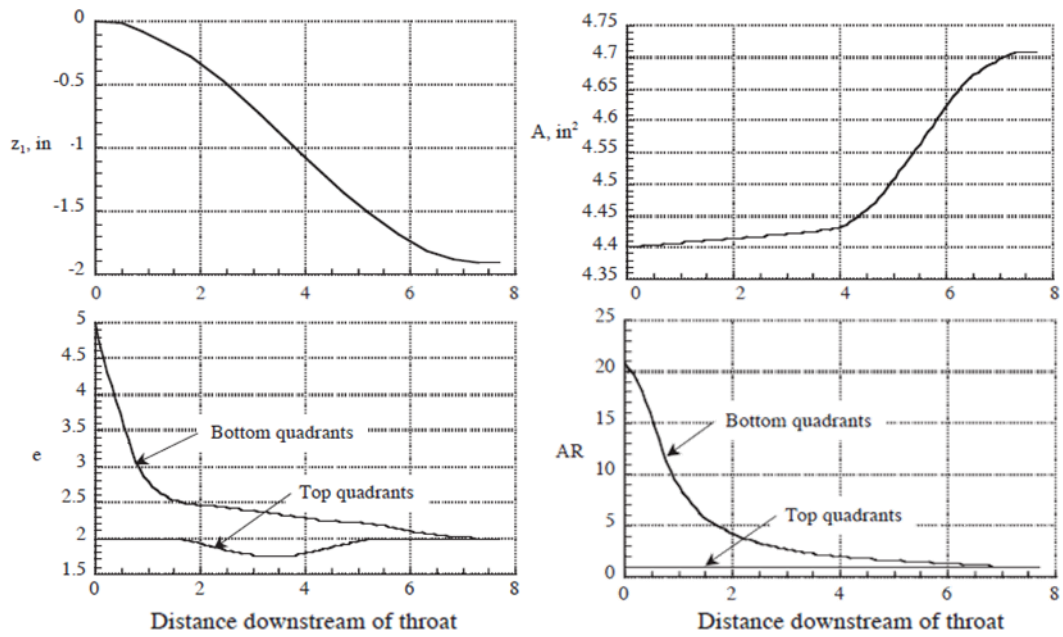
Figure 3-4 Geometry Sections Description [44]

Centerline distribution (z), cross-sectional area (A) for each section and super-ellipse shape parameter (e), duct aspect ratio (AR) for each section quadrant are given in Figure 3-4 with respect to distance downstream of throat.

The sections quadrant shapes are described by Equation 3.1;

$$x_1{}^e + z_1{}^e = 1.0 \tag{3.1}$$

According to given details of the intake duct sections, intake-A duct built and solid model of intake is created by using "SOLIDWORKS12". Sections that built by lofting are given at Figure 3-5, solid model of Inlet-A presented Figure 3-6.

31
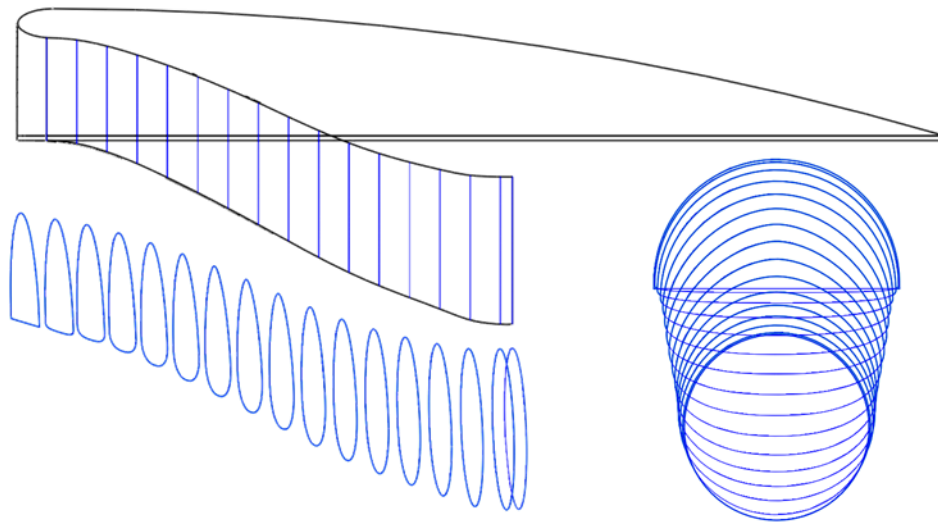
Figure 3-5 Sections of Intake -A
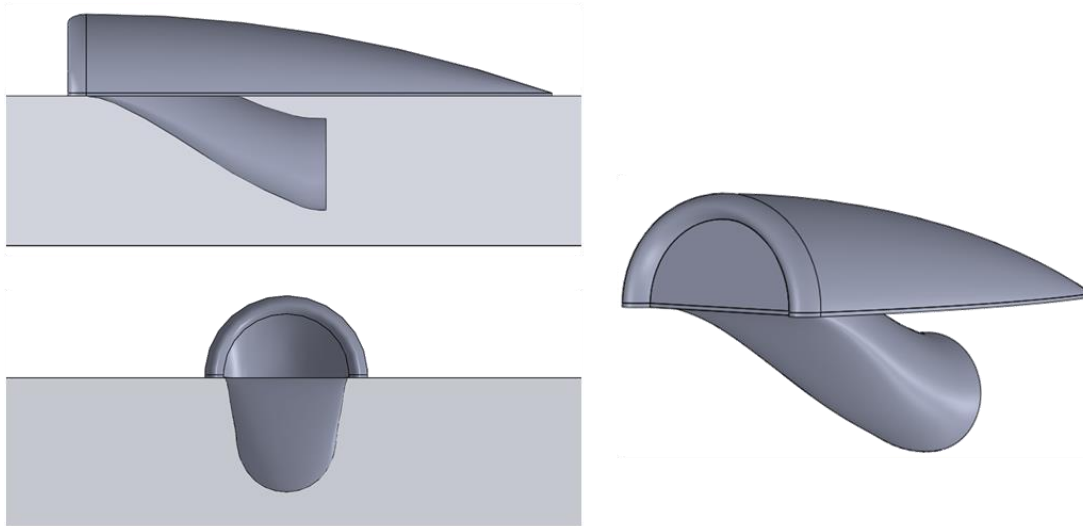
Figure 3-6 Solid Model of Inlet-A

The wind tunnel flow is simulated by mounting the Inlet-A model on a flat plate surface. Length of the flat plate upstream of the inlet duct is calculated to adjust boundary layer thickness at intake duct location in order to match the experimental boundary layer thickness.

For chosen wind tunnel test condition boundary layer thickness and Reynolds Number are given below;

$$\delta = 0.0138 \, m \tag{3.2}$$

$$Re = 13.9 * 10^6 \tag{3.3}$$

Boundary layer thickness for turbulent flow on a flat plate is;

$$\delta = \frac{0.382 * x}{Re^{0.2}} \tag{3.4}$$

Hence;

$$x = 0.960 \ m \tag{3.5}$$

According to calculations, 0.96 m flat plate is located upstream of the intake duct. The plate length behind the intake duct and thickness are chosen as 0.913 m and 0.1 m respectively. Plate dimensions are represented at Figure 3-7.
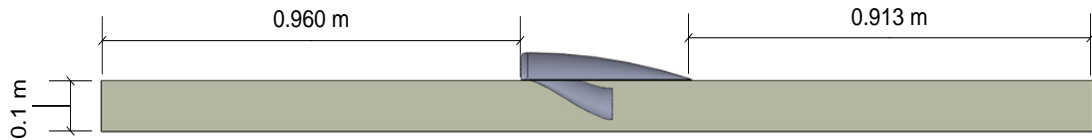
Figure 3-7 Plate Dimensions

3.1.4 Computational Grid Generation and Numerical Analysis

FloEFD adaptive 3-D mesh solver is used for generating computational grid and performing numerical analysis for this problem. FloEFD solves the compressible Navier-Stokes flow equations on structured grids using modified k-ε turbulence model. Three adaptations are performed by FloEFD v12 on the initial computational grid during the CFD analysis in order to capture boundary layer development and fluid-solid interaction. Final computational grid is presented at Figure 3-8 and surface grid of Inlet-A represented at Figure 3-9

Nitrogen gaseous is used to obtain full-scale Reynolds numbers for the wind tunnel test so; nitrogen gaseous is used for the numerical analysis.

Table 3-1 The Element Number of Initial and Final Mesh

Number of Mesh	
Initial Mesh	618,350
Final Refinement	1,874,000
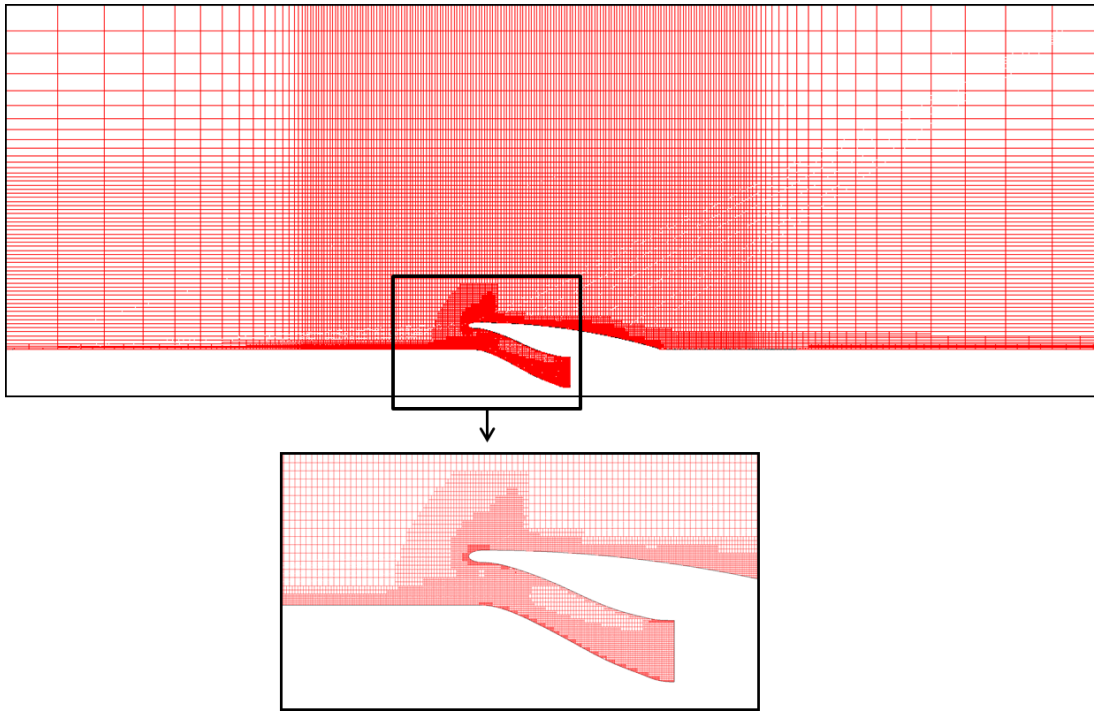
Figure 3-8 Final computational grid
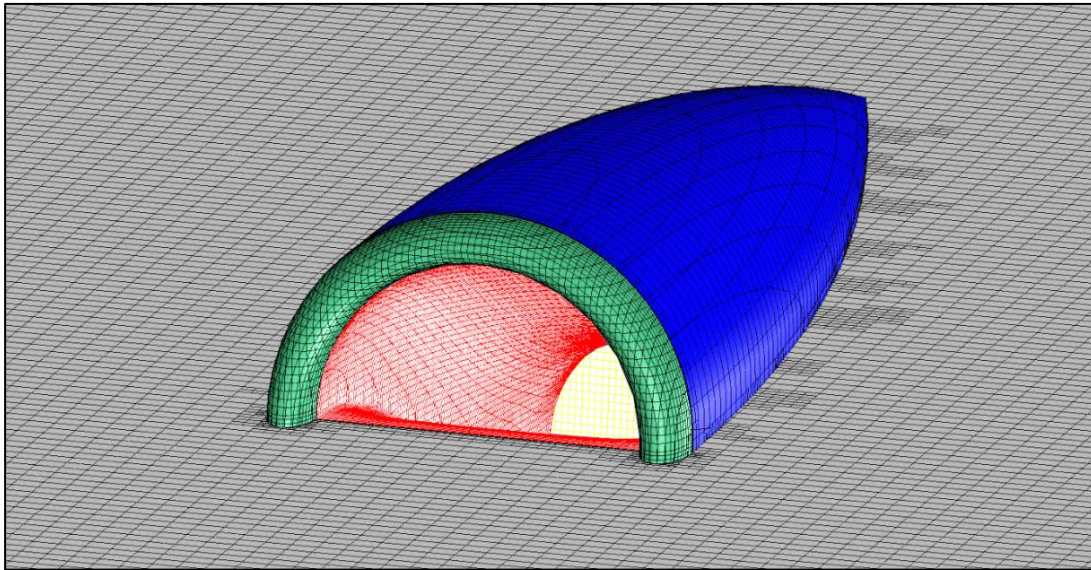
Figure 3-9 Surface Grid of Inlet-A

3.1.4.1 Boundary Conditions

There is not much information about intake exit pressure and temperature about the experiment study in the reference paper so that the mass flow rate for the intake is considered to match the experiment by varying the exit pressure of the intake. Pressure outlet boundary conditions are applied at the downstream exit of the intake (Figure 3-10) between 28000 Pa to 29000 Pa. Mass flow rate results of each analysis

are compared with the experimental data to determine which pressure value simulates the wind tunnel exit conditions. Wind tunnel free-stream test conditions are given as free-stream conditions for numerical analysis and represented at Table 3-2.
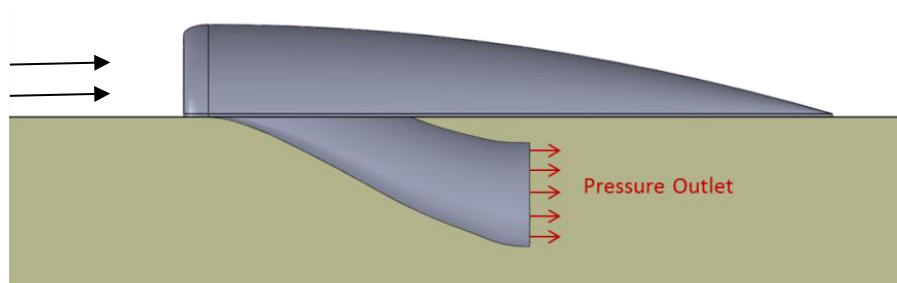
Figure 3-10 Intake downstream boundary conditions

Table 3-2 Free-stream Conditions for Inlet-A Test Case

Mach Number	0.834
Reynolds Number	13.9×10^6
Fluid	Nitrogen
P_{static}	218528.3 Pa
T_{static}	88.2 K
ρ	8.635 kg/m3

3.1.5 Results

Numerical analysis after setting up the problem that modeling the wind tunnel tests are done and results of the numerical analysis are compared with the NASA Langley Research Center experimental results. Performance parameters of S-duct Inlet-A; pressure recovery (PR), distortion coefficient (DC), the ring intensity (intensity), and corrected mass flow rate ($\dot{m}_{corr}$) are given in the equations at Section 1. These values obtained by the CFD analysis are compared with the experimental data in Table 3-3 and Table 3-4.
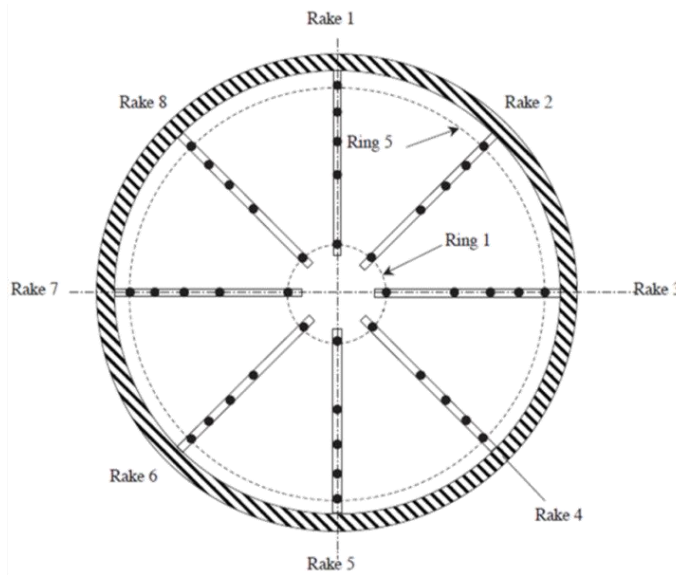
Figure 3-11 Ring of NASA Intake-A

- The Ring Intensity;

Aerodynamic interface plane is depicted in Figure 3-11 that is used for experimental tests. For experimental measurements at the AIP section of Intake-A instrumented with 8 Rake and 5 ring. Area weighted 40 total pressure probe located 45° apart with 5 probes on each arm installed to measure total pressure distributions. Ring radiuses are 6.9596 cm, 16.764cm, 21.87 cm, 25.93cm and 29.44 cm respectively.

As it mentioned in the boundary conditions section mass flow rate for the intake is considered to match the experiment by varying the exit pressure of the intake. Pressure outlet boundary condition is applied on intake exit varied 28000Pa to 29000 Pa. As seen in the Figure 3-10, 283500 Pa matched the corrected mass flow rate of the experiment.
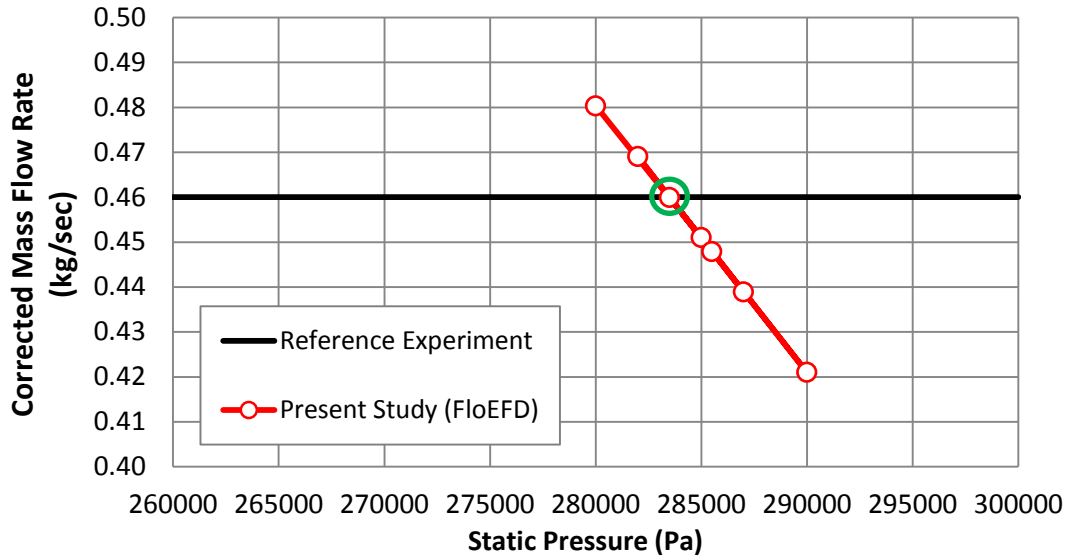
Figure 3-12 Static Pressure Boundary Condition Sweep on AIP

For 28500 Pa static pressure boundary condition, convergence history of PR is represented at Figure 3-13.
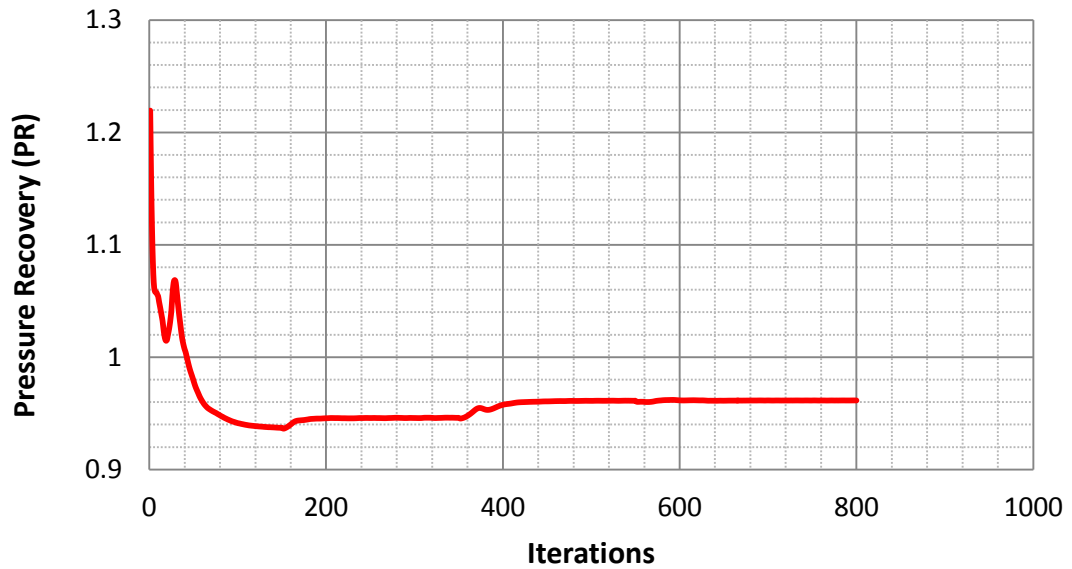
Figure 3-13 Convergence History of Pressure Recovery Coefficient

After 800 iterations calculation is converged and lasts about 4.5 hours by using 8 cores.

The ring intensities for each ring are calculated and compared with experimental data are tabulated in Table 3-3.

Table 3-3 Total pressure Intensity Comparison Experiment vs CFD

Ring	Intensity (Experiment)	Intensity (Present Study)	Error (%)
1(Hub)	0.039	0.028	28.20
2	0.055	0.057	-3.63
3	0.050	0.057	-14.0
4	0.044	0.051	-15.90
5	0.037	0.041	-10.81
Average	0.045	0.0468	3.23

Corrected mass flow rate, pressure recovery and distortion coefficient of the Intake-A are presented in Table 3-4 and compared with the experimental results.

Table 3-4 Present Study Comparison with Experimental Results

Parameter	Reference Experiment	Present Study (FloEFD)	Present Study Error (%)
Mass Flow Rate (MFR)	2.570	2.502	2.64
Pressure Recovery (PR)	0.960	0.961	-0.10
Distortion Coefficient (DC)	0.045	0.046	-2.22

Total pressure distribution contours on AIP obtained in experiment, reference CFD analysis and present study are compared and represented in Figure 3-14.
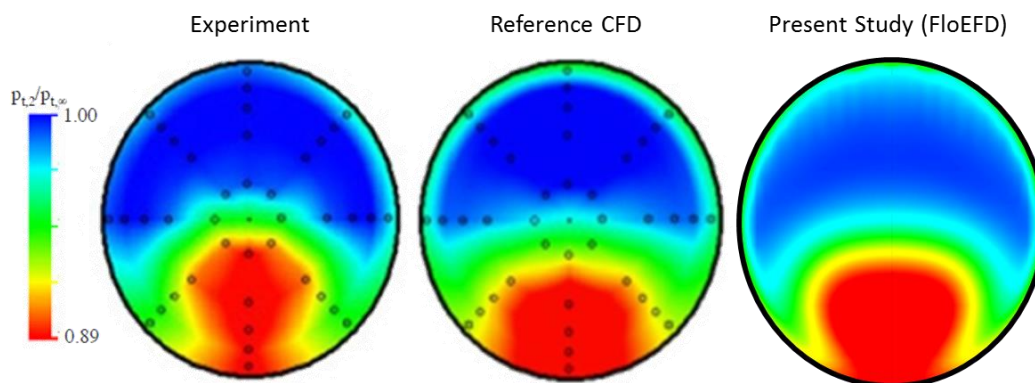
Figure 3-14 Total pressure distribution on AIP

Mach number distribution and total pressure distribution on symmetry plane are compared with the reference CFD solutions in Figure 3-15 and Figure 3-16.
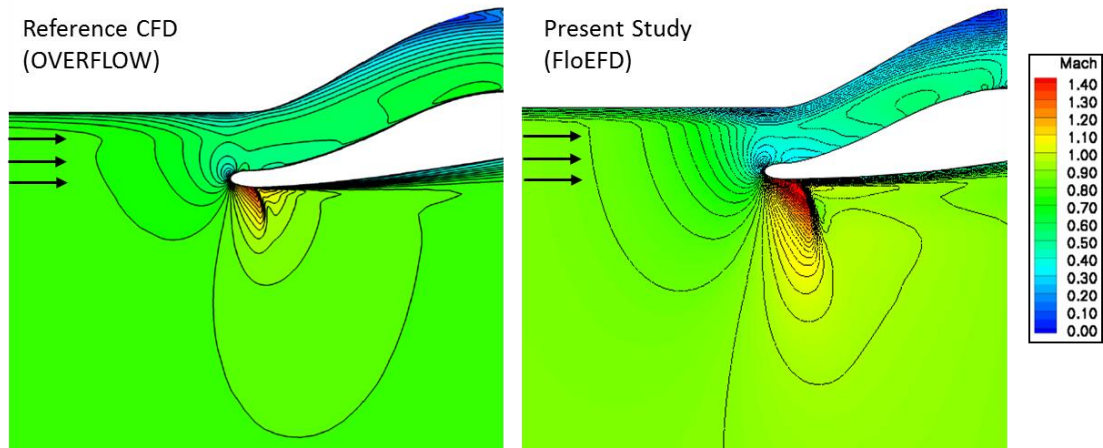
Figure 3-15 Mach numbers distribution comparison on symmetry plane
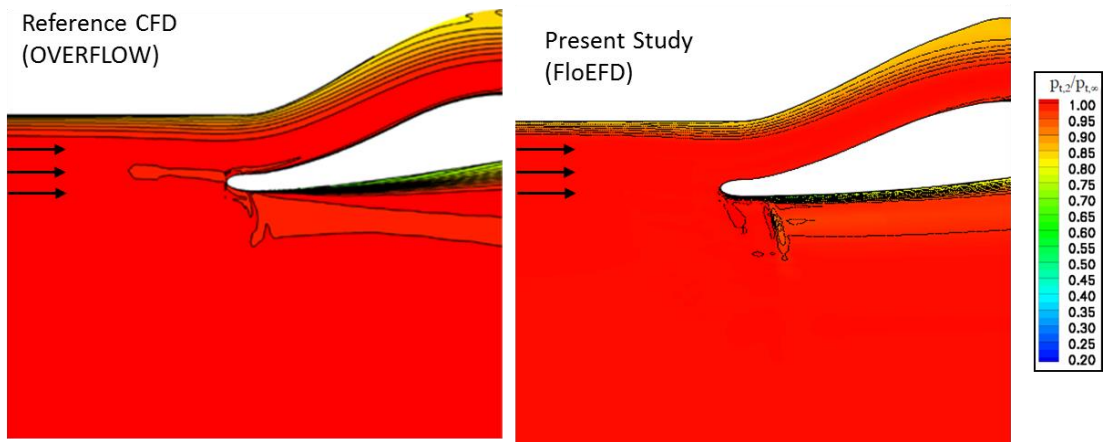
Figure 3-16 Total pressure distribution comparison on symmetry plane

3.1.6 Comments

Numerical analysis of flush mounted, S-duct intake with large amount of boundary layer ingestion is done by using commercial FloEFD v12. According to the results compared with the experimental data and reference CFD solutions, FloEFD v12 produced very accurate results to reference experiment and reference CFD solutions. As seen in Table 3-4 Pressure recovery result of present study is nearly the same with the experiment, mass flow rate and distortion coefficient results are below the %5 error rate. Total pressure distributions on AIP shows well agreement with the experiment, moreover better than reference CFD calculations. In Figure 3-15 and, Figure 3-16 Mach number distribution and total pressure distribution on symmetry plane shows well accordance with the reference CFD results. In all comparisons done in this study, FloEFD v12 has very-well agreement with the test data and reference CFD solutions.

3.2 NASA S-SHAPED INTAKE DIFFUSER TEST CASE

3.2.1 Introduction

The second validation study of FloEFD v12 based on S-duct diffuser wind tunnel tests done by NASA Lewis Research Center [7]. This test case contains large separated flow region that is complex and difficult to predict accurately by numerical methods [43]. In this manner Vuillerme, Deck, and Chevrier tried to develop numerical methods to handle this flow problem and focused on validation of their methods by comparing their data with available experimental data in their paper.
In this validation process of FloEFD v12 results are compared with available experimental data and other numerical methods results found in the reference paper.

3.2.2 Geometry Description

The duct centerline consists of two circular arcs sharing same radius. The centerline curve coordinates given by the equations below. The geometry of S-shaped duct is represented in Figure 3-17.
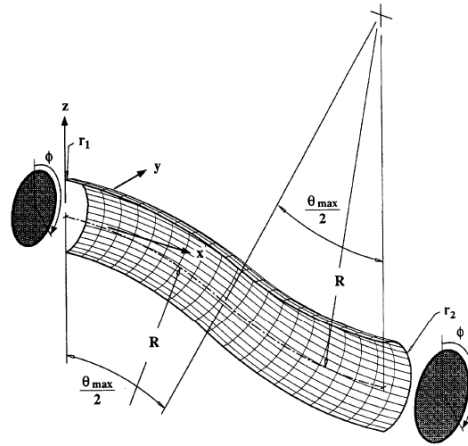
Figure 3-17 Diffuser of S-shaped intake test-case [7]

$$For\ 0 \leq \theta \leq \frac{\theta_{max}}{2} \tag{3.6}$$

$$x_{cl} = R.\sin(\theta)\ ; \qquad y_{cl} = 0\ ; \qquad z_{cl} = R.\cos(\theta) - R \tag{3.7}$$

$$For \quad \frac{\theta_{max}}{2} \leq \theta \leq \theta_{max} \tag{3.8}$$

$$x_{cl} = 2R.\sin\left(\frac{\theta_{max}}{2}\right) - R.\sin(\theta_{max} - \theta) ; \quad y_{cl} = 0 ; \tag{3.9}$$

$$z_{cl} = 2R.\cos\left(\frac{\theta_{max}}{2}\right) - R - R.\cos(\theta_{max} - \theta) \tag{3.10}$$

$$\frac{2r}{D_1} = 1 + 3\left(\frac{D_2}{D_1} - 1\right)\left(\frac{\theta}{\theta_{max}}\right)^2 - 2\left(\frac{D_2}{D_1} - 1\right)\left(\frac{\theta}{\theta_{max}}\right)^3 \tag{3.11}$$

The duct geometry is built by using equations given above where $\theta_{max} = 60^0$ and R=1.02 m. Diameter of intake duct is 0.2042 m and outlet diameter is 0.2544 m. Thus area ratio of 1.52 is used to diffuse the flow to lower Mach numbers from the intake to the outlet of the duct. Some sections are employed to measure the static pressure, total pressure and the velocity over the NASA's test process. In order to compare these properties with the test data, these sections located in the S-duct according to the given dimensions. Total pressure isolines and normal velocity isolines generated at these sections and compared with the experimental data measured by NASA. Locations of the sections are given with the solutions. S-shaped intake diffuser modeled according to given dimensions by using commercial SOLIDWORKS™ 2012 solid modelling program and solid model represented on Figure 3-18.
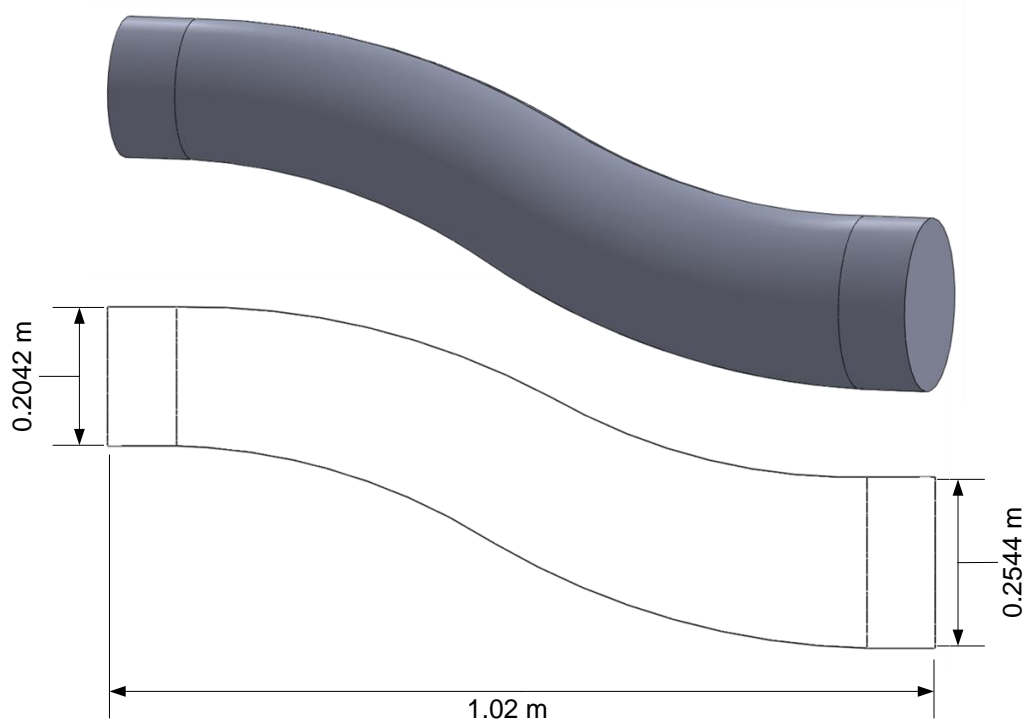
Figure 3-18 Solid Model of S-shaped intake diffuser

3.2.3 Computational Grid Generation and Numerical Analysis

FloEFD adaptive 3-D mesh solver is used for generating computational grid and performing numerical analysis. The volume of the intake diffuser is used as computational domain in order to simulate test conditions. As it mentioned above at Section 3 FloEFD uses Modified k-ε turbulence model algorithm. Therefore Modified k-ε turbulence model is used for the numerical calculations.

NASA Lewis Research Center test conditions are used represented at Table 3-5.

Table 3-5 NASA Wind Tunnel Test Conditions

Mach Number	0.6
Mass Flow Rate	7.135 kg/s
Reynolds Number	2,600,000

Mass flow inlet boundary condition is applied at intake duct and pressure outlet boundary condition is applied at the outlet of the S-shaped intake diffuser. The wind tunnel ambient conditions; which are static pressure of 101325Pa and static temperature of 300K, are defined as pressure outlet B.C. Intake mass flow rate is

7.135 kg/s according to the tunnel measurement [43] is given as intake boundary condition. The boundary conditions are demonstrated at Figure 3-19 below.
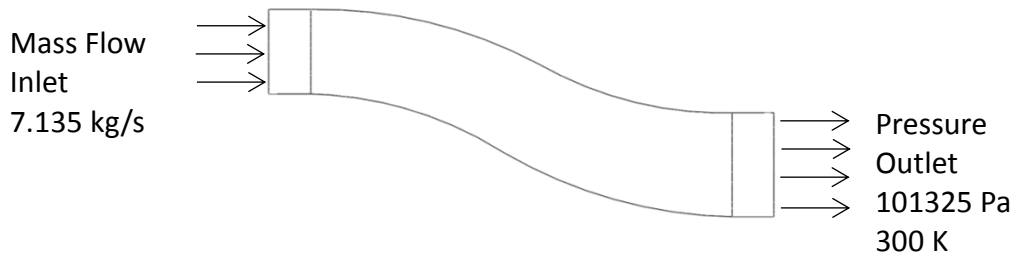
Figure 3-19 Boundary Conditions applied for the numerical analysis of S-shaped intake diffuser

FloEFD v12 can apply the mass flow intake boundary condition as a fully developed flow. For the internal flow that passes through round and rectangular intake openings, this option provides to specify the velocity profile and turbulence parameters (turbulent energy, dissipation) automatically corresponding to the fully developed flow in a tube demonstrated at Figure 3-20.
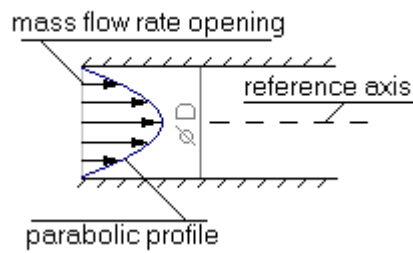
Figure 3-20 Fully developed flow applied as mass flow intake [52]

Computational domain and cartesian mesh used for CFD analysis are represented at Figure 3-21.
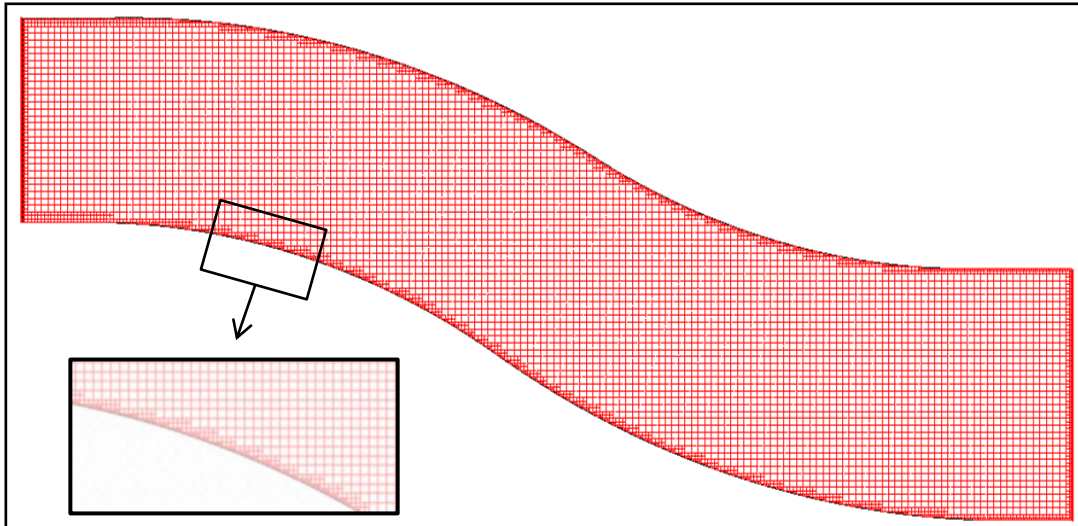
Figure 3-21 Computational Domain and Cartesian Mesh

Throughout the numerical calculations, FloEFD v12 applied adaptive mesh refinements for three times.

The number of computational mesh after each refinement are represented Table 3-6.

Table 3-6 The Number of Mesh After Refinements

Number of Mesh	
Initial Mesh	846,816
First Refinement	1,300,000
Second Refinement	3,700,000
Final Refinement	10,843,000

3.2.4   Results

The reference study employed different turbulence models such as "Baldwin-Lomax", "Spalart-Almaras", "k-l Smith" and "k-kl ONERA" in order to assess the intake performance and investigate the influence of the turbulence model to intake performance. In present study Modified k-ε turbulence model is used for the numerical analysis at the same conditions with CFD calculations of the reference papers.

Present study pressure recovery coefficient (PR) result of the S-shaped intake diffuser is compared to reference CFD analysis results. NASA Lewis Research Center test data is also attached to the CFD solutions and represented together at Figure 3-22.
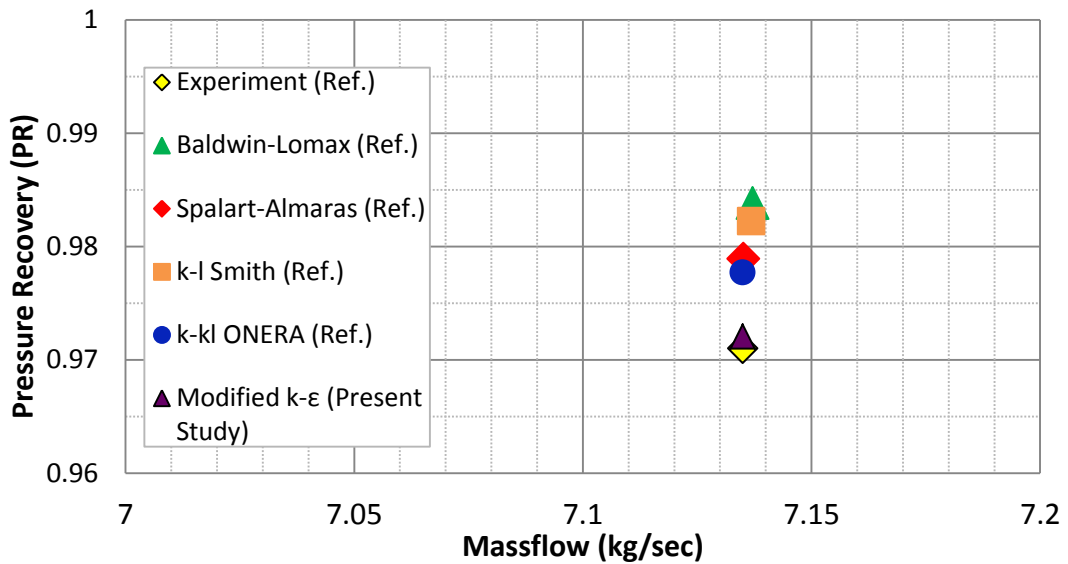
Figure 3-22 Comparison of the PR coefficient with the reference CFD and Experiment data

It can be seen from Figure 3-22 that all turbulence models in reference paper give different results compared to experimental data. It can be also seen that present study solution is identical with the experiment. Results of experiment and present study are represented at Table 3-7 with the percentage error.

Table 3-7 Comparison of Experiment and Present Study

	Experiment Result	FloEFD Result	Error (%)
PR	0.971	0.972	0.11
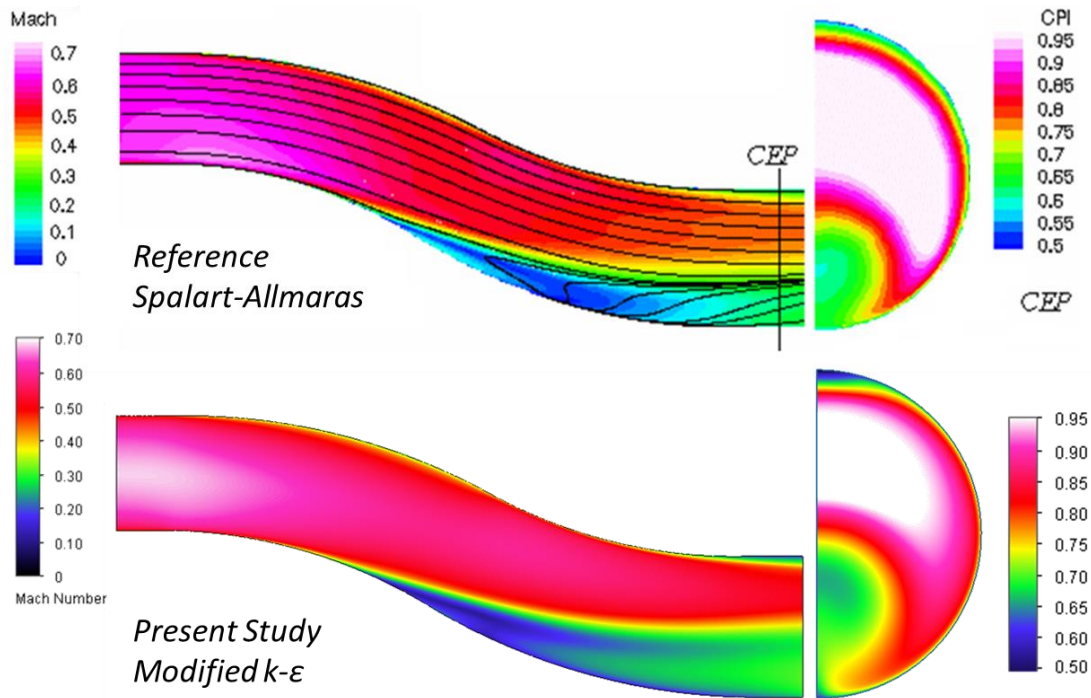
Figure 3-23 Mach Number Contour Comparison of Reference CFD Solution and Present Study

According to the Mach number contours; Reference's CFD solution that obtained by using Spalart-Almaras turbulence model gives identical results with the present study. However it can be seen from the Figure 3-23, modified k-ε turbulence model predicts the separation region slightly before than the Spalart-Almaras turbulence model and k-ε turbulence model finds the reattachment region larger than Spalart-Almaras turbulence model. Although, minor flow separation and reattachment discrepancies are found between the reference CFD and present study, it can be said that both solutions give nearly the same solutions at all.

3.2.5 Section Study

In this section, non-dimensional form of total pressure and normal velocity distributions at given stations of S-shaped intake diffuser are compared with experimental results and reference CFD results. All data given in this study are in non-dimensional form. Intake centerline flow parameters define as the reference states such as, $P_{0,cl}$, P_{cl} and M_{cl} . Nondimensional form of the flow conditions are given in the equations below.

Total pressure distribution;

$$C_{p0} = \frac{P_0 - P_{cl}}{P_{0,cl} - P_{cl}} \qquad (3.12)$$

Normal velocity distribution;

$$C_{vel} = \frac{M}{M_{cl}} \qquad (3.13)$$

In the figures below, present study represents FloEFD modified k-ε turbulence model, Ref. CFD corresponds to reference CFD solutions using Baldwin-Lomax turbulence model. Experiment represents NASA Lewis Research Center test data of the S-shaped intake diffuser.

3.2.5.1 Section B

Section-B is the second station of the S-shaped intake diffuser. At this station, S-shape becomes to form to deflect the incoming air flow. This section exists at $\frac{s}{d} = 0.96$, from downstream of the centerline origin. Station of the Section-B is demonstrated in Figure 3-24. Total pressure distributions in Section-B are represented at Figure 3-25.
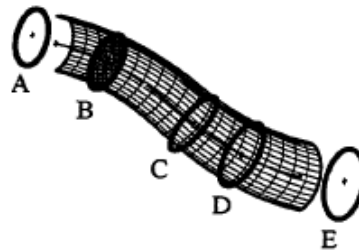
Figure 3-24 Section-B of S-shaped intake diffuser

Experiment

Ref. CFD
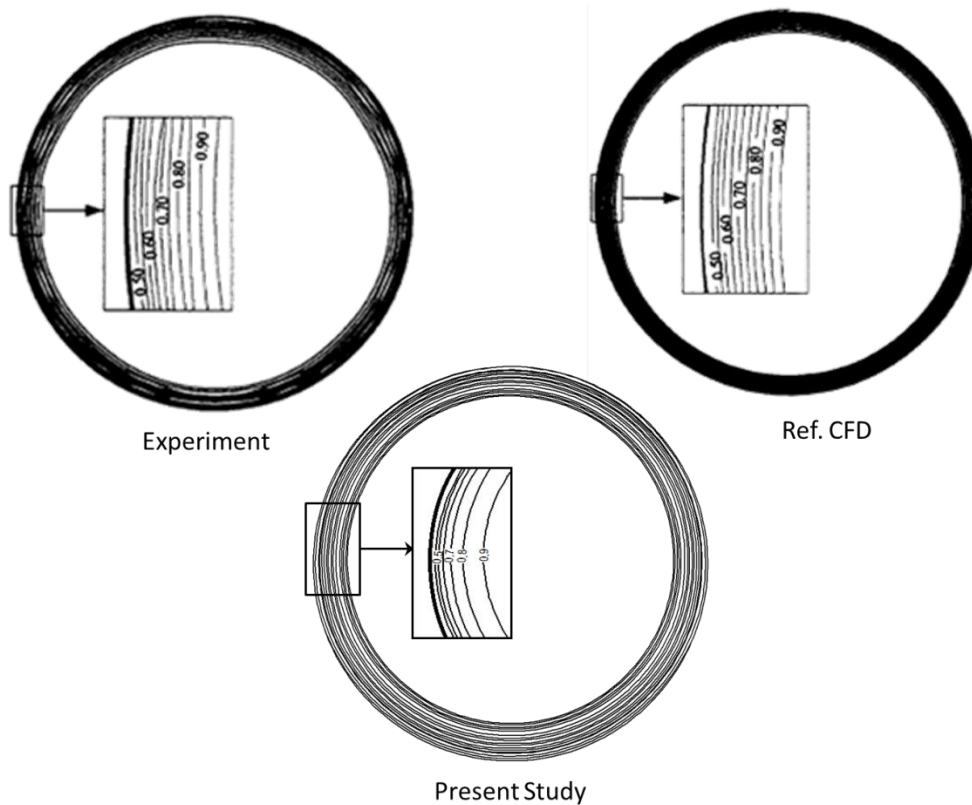
Present Study

Figure 3-25 Total pressure distributions in Section-B

Boundary layer development can be seen on the wall of duct at Section-B. No deflection in centerline curve from Section-A to Section-B. Present study results shows well agreement with the both experimental and reference CFD results in Section-B.

3.2.5.2 Section C

Section-C is the third station of the intake that air passing through. This section exists at $\frac{s}{d} = 2.97$, about 0.35 diameters downstream of the S-duct entrance. Station of the Section-C is demonstrated in Figure 3-26. Total pressure and normal velocity distributions in Section-C are represented at Figure 3-27 and Figure 3-28.
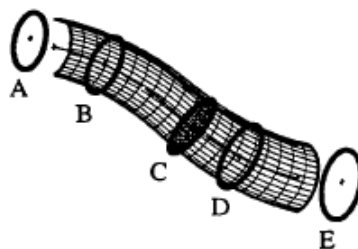
Figure 3-26 Section-C of S-shaped intake diffuser
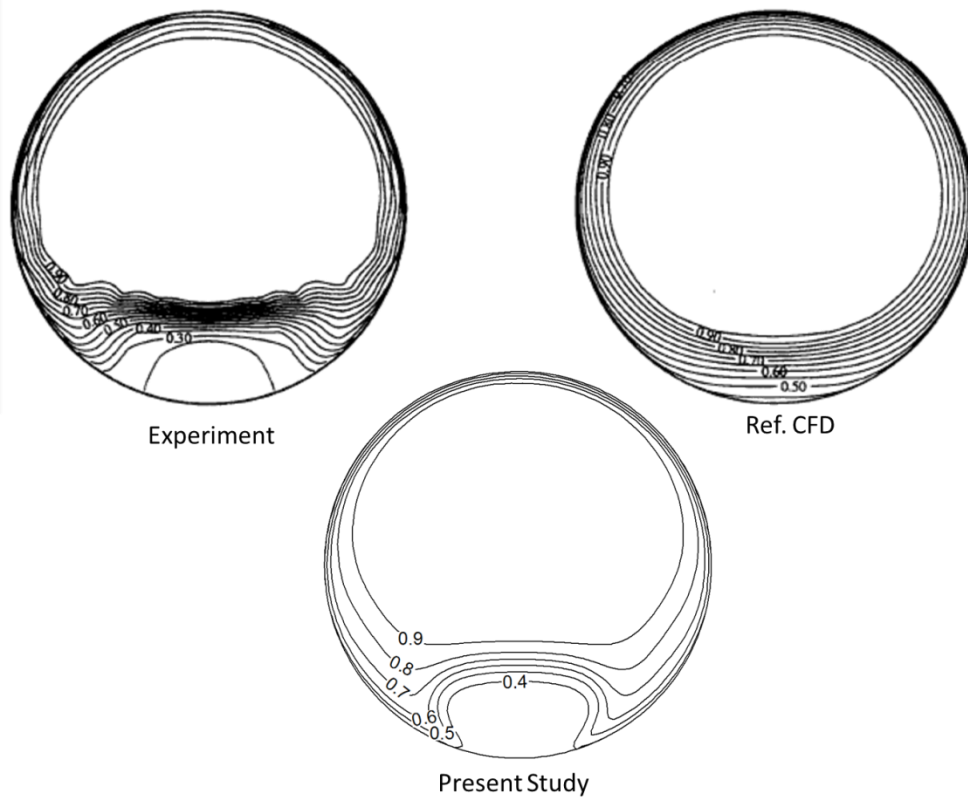
Figure 3-27 Total pressure distributions in Section-C
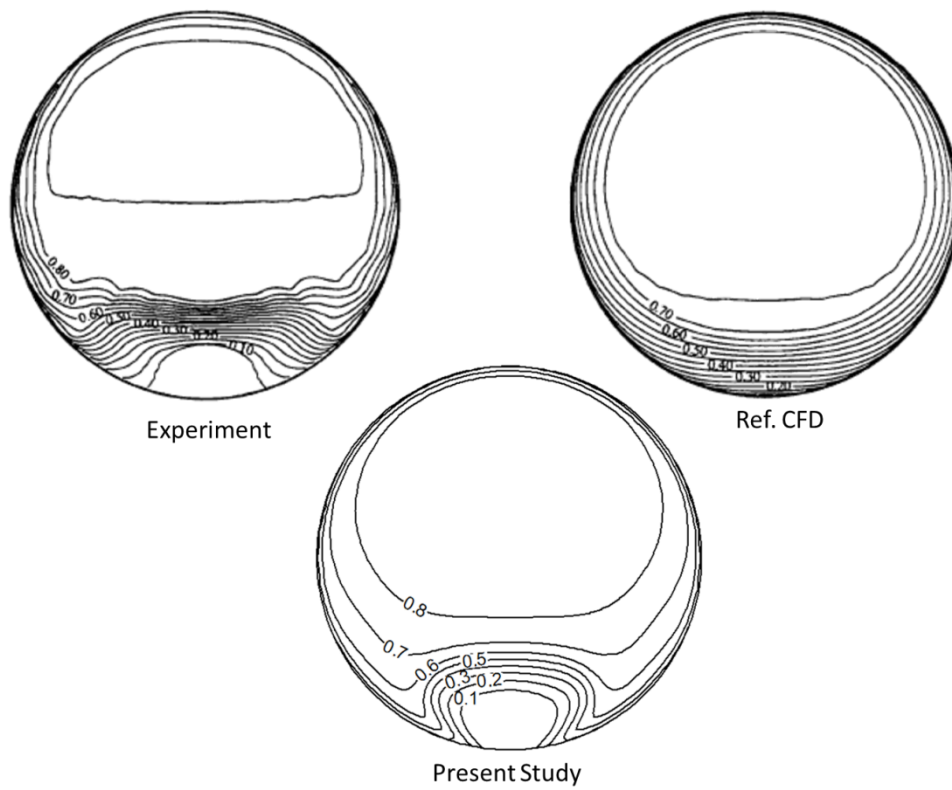
Figure 3-28 Normal velocity distributions in Section-C

49

The Section-C located in the middle of the S-shaped intake diffuser. This location exists on the separated air flow region. Total pressure and normal velocity distributions discrepancies arise from this section compared to Section-B due to the high deflection angle of the centerline curve on the location of the Section-C. It means that flow separated from intake surface at this section. It can be seen from the total pressure distributions and normal velocity distributions; low momentum region in the bottom portion of the S-duct is developed. Reversed flow generate adverse pressure gradient and boundary layer thickening caused this low momentum layer and this phenomena decreases the total pressure recovery coefficient in other words efficiency of the intake. Besides, present study has good accordance with the experimental results than the reference CFD results.

3.2.5.3 Section D

Section-D is the fourth station of the intake that measurements are done. This section exists at $\frac{s}{d} = 4.01$, from downstream of the centerline origin. Station of the Section-D is demonstrated in Figure 3-29. Total pressure distributions and normal velocity distributions in Section-D are represented Figure 3-30 and Figure 3-31.
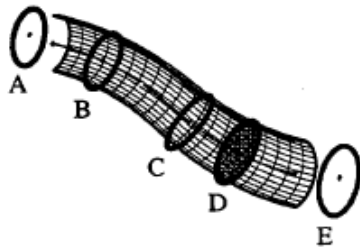
Figure 3-29 Section-D of S-shaped intake diffuser
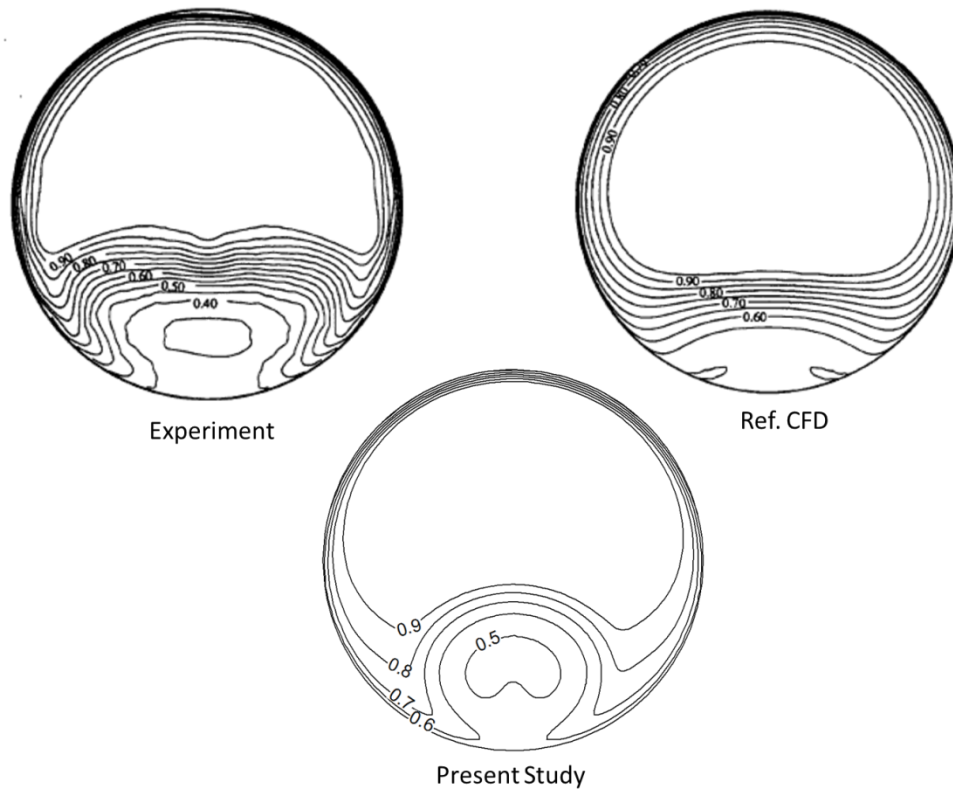
Figure 3-30 Total pressure distributions in Section-D
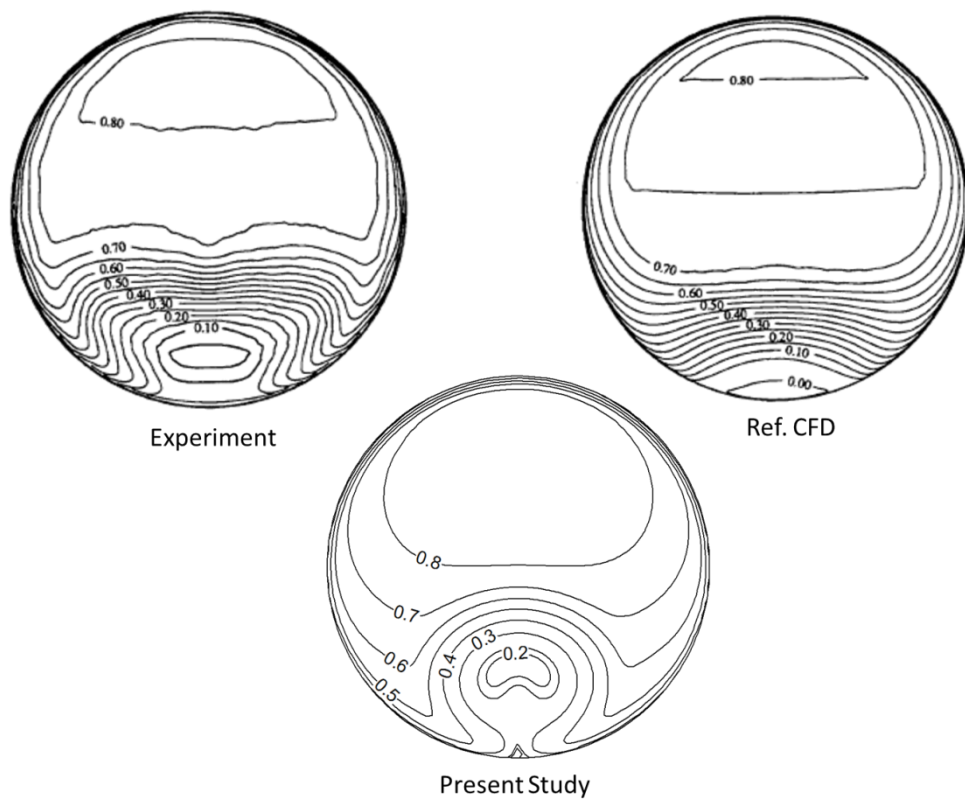
Figure 3-31 Normal velocity distributions in Section-D

In the Section-D total pressure and normal velocity distributions shows low momentum region upward of Section-C in the bottom of the S-duct. Figure 3-31 represents that near zero velocity region is transported from the bottom of the S-duct to away from the surface. Additionally present study shows well agreement with the experimental results than the reference CFD results as the same as Section-C.

3.2.6 Comments

Validation of the FloEFD 12 is done in this study by solving internal flow of S-shaped intake diffuser. According to the results compared with the experimental data and reference CFD solutions, FloEFD modified k-ε turbulence model solution very accurate solving the internal flow of S-shaped intake diffuser. In all comparisons done in this study, FloEFD v12 has very-well agreement with the test data and reference CFD solutions. Holding all these comprehensive results obtained by FloEFD v12 analysis, it can be said that an intake design study can be performed by using FloEFD v12.

CHAPTER 4

AN INTAKE DESIGN and OPTIMIZATION FOR A GENERIC CRUISE MISSILE

In this section, the benchmark design problem is described. Baseline cruise missile intake design requirements are defined. Geometric details of the subsonic-transonic missile body and intake are represented. A generic missile body is selected with a typical ogive nose, length to diameter ratio of 1.2. Geometric details are given in Figure 4-3. Three diameters length subsonic-transonic intake geometric parameters are given in details. S-Shape design is mentioned comprehensively. CATIA V5 3D modelling software is used to generate the parametric intake model by using generative shape design module.

4.1 Benchmark Problem Description

In order to design appropriate intake for design requirements and avoid from enlarging design space, the limits of design should be specified accordingly. It is important to consider design point of the cruise missile while designing intake that will be integrated to turbojet engine. In this study design problem consists of parameterization baseline intake geometry for fixed engine geometry and for defined cruise conditions of cruise flight.

4.1.1 Baseline Cruise Missile Intake Flight Conditions and Design Requirements

Cruise missiles generally make cruise flight in small angle of attacks in order to reduce drag like commercial aircrafts. In this study, 2° angle of attack is determined as cruise angle of attack and 0.8 Mach is determined as cruise Mach number for intake design. Flight conditions of generic submerged intake for cruise are given at Table 4-1.

Table 4-1 Subsonic Intake Design Point on Cruise Condition

Mach Number	0.80
Angle of Attack	2°
Angle of Sideslip	0°
Altitude	Sea Level
$\dot{m}_{corr}$	4.43 kg/s

A commercial turbojet engine is used in cruise missiles, represented at Figure 4-1 .
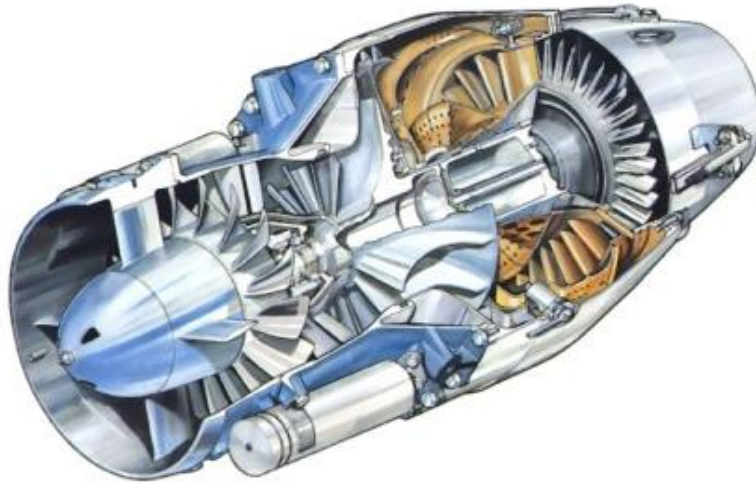
Figure 4-1 Commercial Turbojet Engine

Mass flow rate is an engine requirement, as it mentioned before. In this study the required corrected mass flow rate of the engine is assumed to 4.43 kg/s withstanding literature and engine company's values. In this design optimization study, intake will supply this amount of mass flow to the engine at cruise conditions. Engine hub is used for ensuring flow uniformity upstream of the compressor blades. Geometric details of engine hub are demonstrated in Figure 4-2.
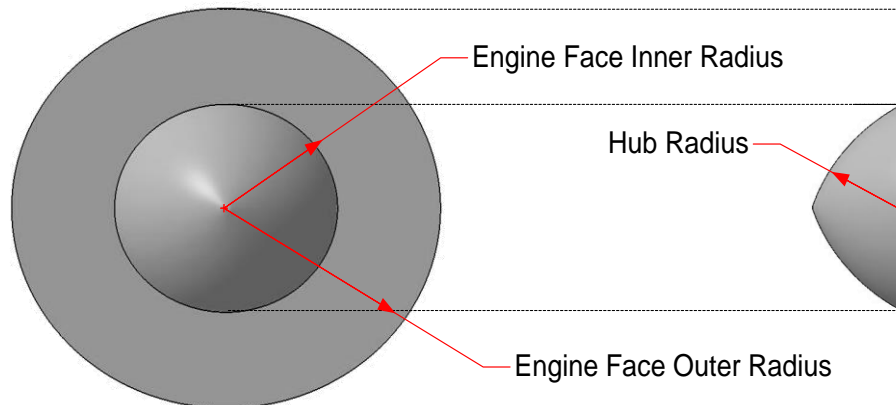
Figure 4-2 Hub of Engine Geometry

4.2 Geometry of Generic Subsonic Submerged Intake

Subsonic-transonic S-duct intake is placed on cruise missile body. In this study cruise missile body has no tail or wings because in the optimization study numerous geometry will be analyzed by CFD tool. In order to diminish CFD analysis time, wings or tails are not be taken in to account design study. If wings or tails existed on the missile geometry, optimization process time would increase markedly regarding increasing number of grids. Details of the geometry will not be given due to confidentiality. Diameter of the missile is given as D, length of missile, length of nose, location of the Aerodynamic Interface Plane (AIP) are given in Figure 4-3 in terms of missile diameter. Length of intake also determined as three diameters. These parameters are remained constant during design optimization study.
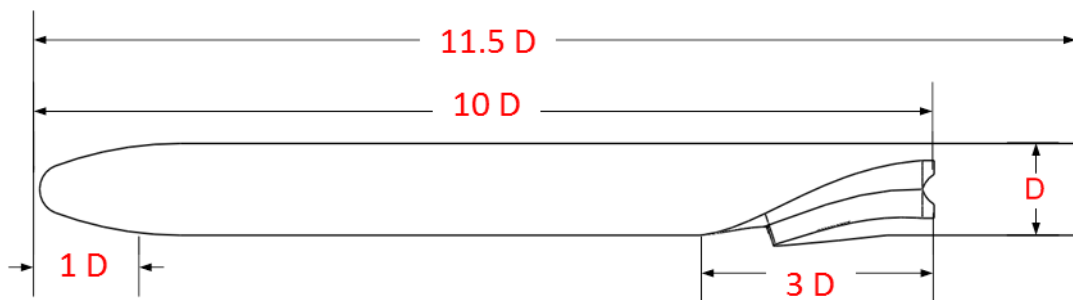
Figure 4-3 Symmetry Section of Subsonic Body Intake Missile Geometry

4.2.1 Parameterization of S-Shaped Submerged Intake

Intake of the subsonic-transonic cruise missile is examined in two main parts, which are ramp and diffuser. These parts are modeled by 20 different sections attached to

each other linearly and are perpendicular to S-Shape curve at each section location. Motor tangent length is also a required parameter for design process in order to provide flow tangency upstream of the compressor face. Detailed information about sections that form ramp and diffuser sections, S-shape curve and motor tangent length will be given below. These parameters are represented at Figure 4-4.
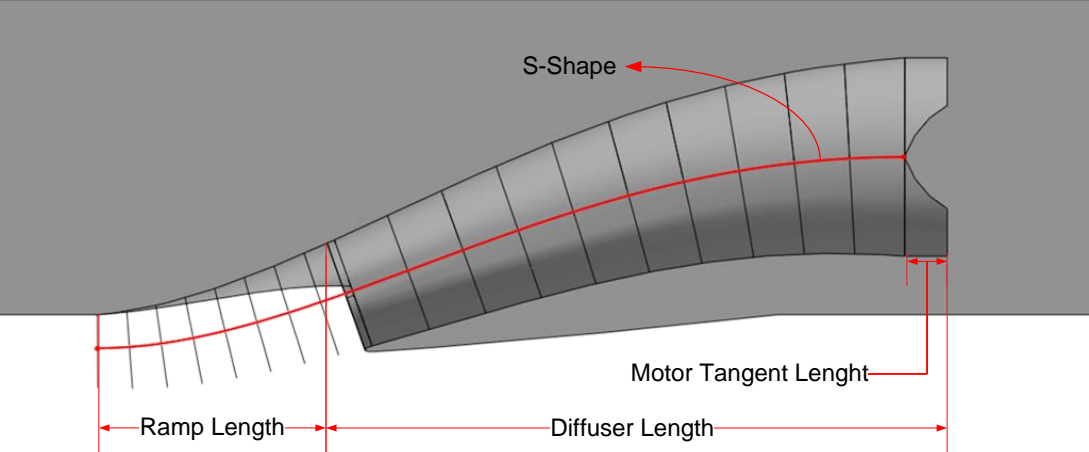
Figure 4-4 Parts of the Subsonic Intake Geometry

Sections consist of two concentric ellipses with same width and different height. Upper and lower side length of the section from geometric center is named as e_1 e_2, respectively. The half width of the section is represented as e_3. These parameters are the inputs of the throat section (9th section) in design process in order to build S-duct. The throat section of the ramp is given in Figure 4-5.
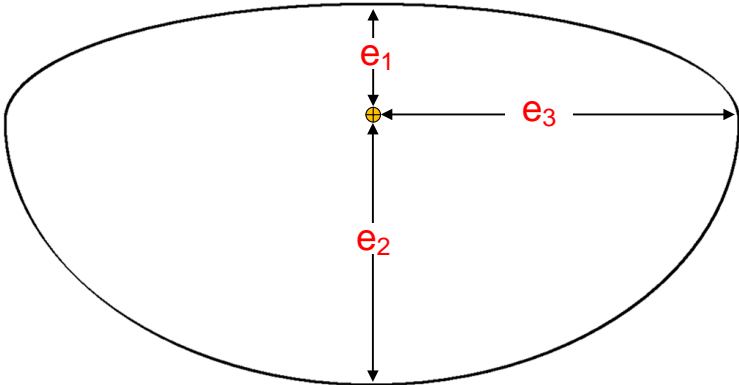
Figure 4-5 Throat Section of Parametric Intake

The S-duct is modeled in 20 sections, 9 of which constitute the ramp part of the S-duct and the rest create the diffuser part. Thereby the diffuser part of the S-duct is constructed by the 11 different sections which are formed by increasing throat

56

section parameters to the AIP along the S-Shape curve. Ramp sections are modelled similarly to the diffuser but throat parameters are decreased through the S-curve to the ramp start. Last two sections (19 and 20) have the same geometry in order to ensure tangency at AIP. Isometric view of all sections through the S-Shape for basis geometry is given in Figure 4-6.
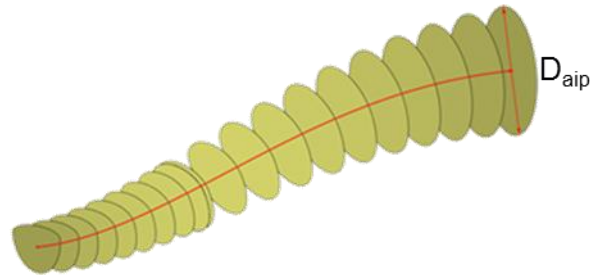
Figure 4-6 Sections from Ramp Starting to AIP through the S-Shape Curve

The throat section parameters are changed linearly according to S-curve length between each other. All sections are arranged to S-shape curve from their geometric center. Parameters, e_1,e_2 and e_3 are increased linearly to the AIP diameter limit of D_{aip}. This limit is specified by the engine face or engine compressor diameter. Thereby design study has two design constraints from the AIP geometry as given below.

$$e_1 + e_2 \leq D_{aip}$$

$$2 * e_3 \leq D_{aip}$$

Linear increase e_1,e_2 and e_3 values in consequence of section areas applied for parametric geometry. The first section of ramp is located at $X = 0$ and the others stretch out along the S-Shape curve to the AIP which is located at $X = 3D$.Isometric view of the intake with construction sections is given in Figure 4-7.
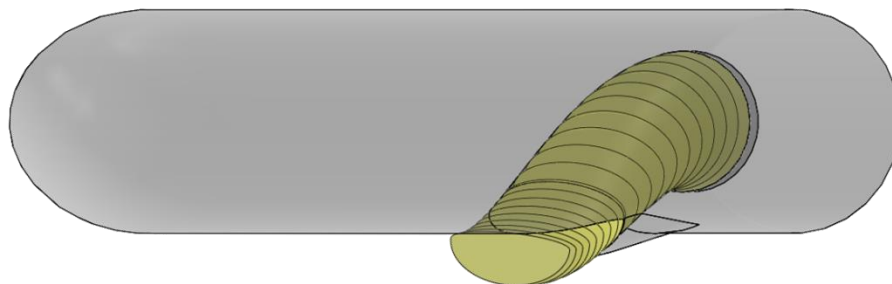
Figure 4-7 Isometric view of sections on Missile Body

Lip is another geometric parameter for subsonic-transonic intakes that affects the flow and air entrance to the duct. On the other hand lip design also affects the drag characteristics of the missile for submerged intakes. In the literature lip design is investigated independently from the other design parameters. [41]. Thereby in this study lip design is not investigated in this study. Lip part of the parametric intake is designed by combining two NACA profiles of upper and lower side and lip parameters remain constant during design study. NACA0012 profile is used for both side of the lip geometry whereas different profile lengths are used for the upper and lower sides. Upper part and lower part of the lip sections are given in Figure 4-8. , and the NACA profiles and profile lengths are given in Table 4-2.
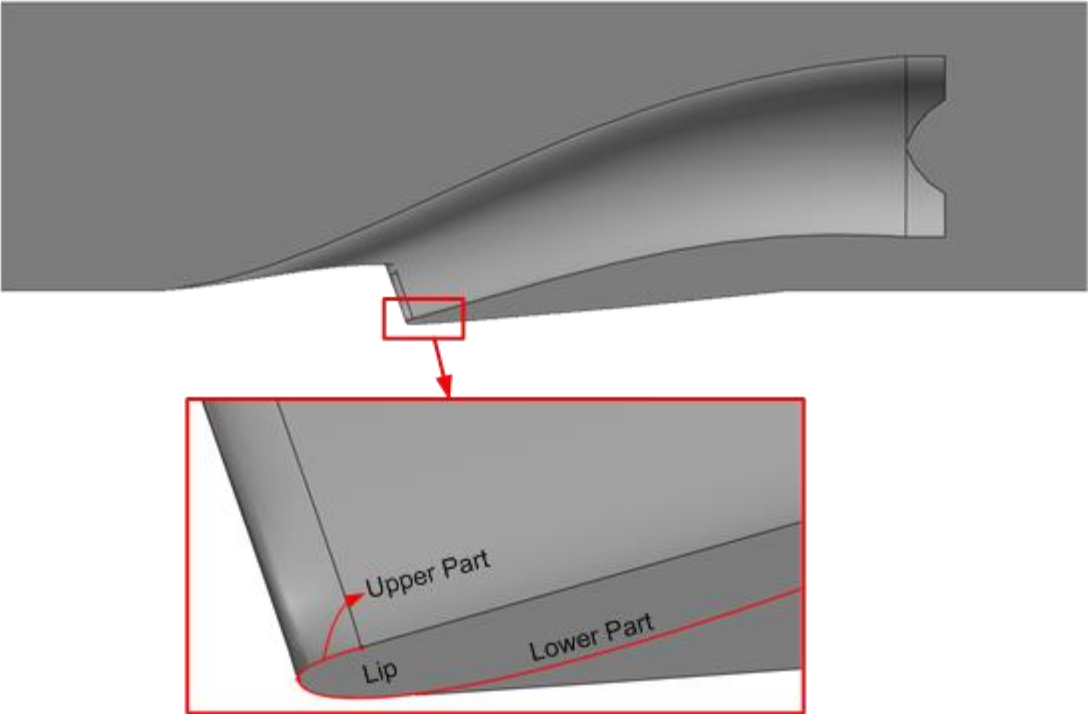
Figure 4-8 Lip Geometry of Generic Submerged Intake

Table 4-2 NACA Lip Geometric Details

Lip Section	NACA Profile	Profile Length (mm)
Upper Part	0012	33.33
Lower Part	0012	116.66

4.2.2 S-Shape Design

S-shape is one of key parameter of intake design [41]. S-shape is the main dominant parameter that determines the how air deflects in the intake. S-shape centerline curvature effects the distortion of the flow because of flow non-uniformity at the exit of the intake, and it dictates the flow separation where the turning stations of the S-Shape. In order to avoid flow separation and high distortion rates, the S-shape must be well-designed and efficient aerodynamically.
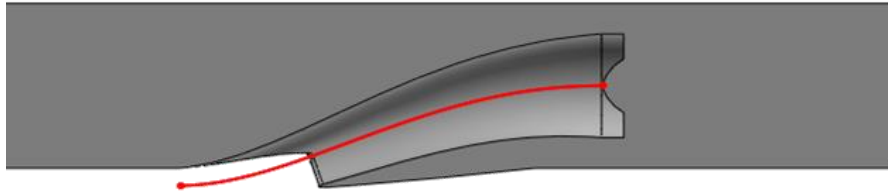
Figure 4-9 S-Shape view from Missile Symmetry Section

S-shape is generated by using 4th order polynomial with tangency boundary conditions at starting and ending points of the S-curve. Location of the saddle point on the curve is defined with the "k" parameter as a ratio of the projection of the S-curve length on x-direction where H is the y-direction offset length and L is the length of S-curve on the x-direction.
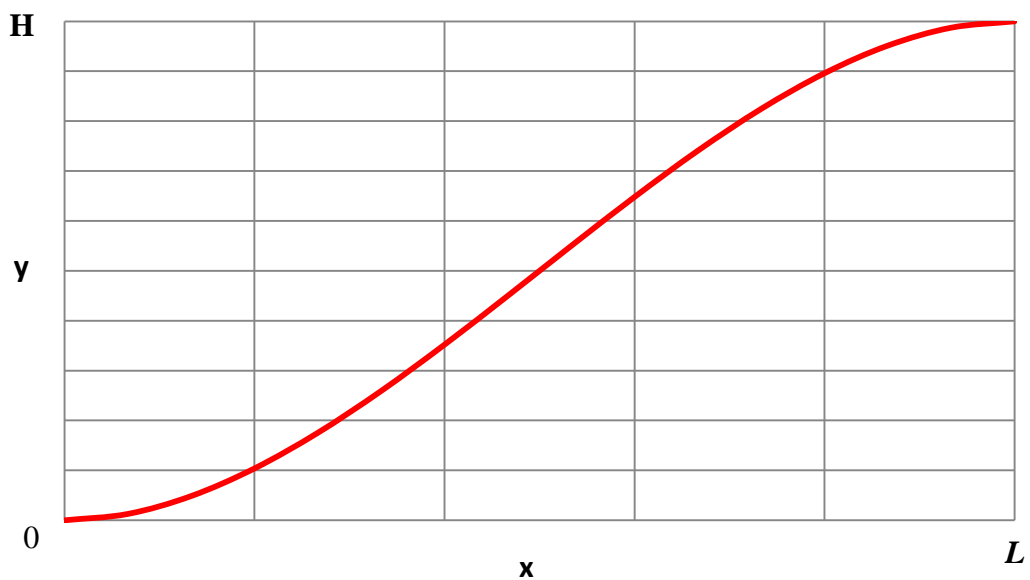
Figure 4-10 4th order S-Shape curve

The general equation of the S-Shape curve specified as quartic function 4th order polynomial is given below.

59

$$y = ax^4 + bx^3 + cx^2 + dx + e \qquad (4.1)$$

While generating S-shape curve; boundary conditions are needed to specify the boundaries of the starting and ending points of the S-curve and apply the tangency conditions on these points. A boundary condition is also applied to determine and control the saddle point of the S-curve to change the curve characteristics during the intake design process.

- Boundary Condition 1

The first boundary condition specifies the starting point of the curve.

at $x = 0$; $y = 0$

Hence

$$y = ax^4 + bx^3 + cx^2 + dx + e \qquad (4.1)$$

$$e = 0 \qquad (4.2)$$

- Boundary Condition 2

The second boundary condition specifies the starting point of the curve is tangent to x axis ($y = 0$).

At $x = 0$; $y' = 0$
$$y' = 4ax^3 + 3bx^2 + 2cx + d = 0 \qquad (4.3)$$

Hence;
$$d = 0 \qquad (4.4)$$

- Boundary Condition 3

The third boundary condition specifies the ending point of the curve.

At $x = L$; $y = H$
$$aL^4 + bL^3 + cL^2 = H \qquad (4.5)$$

- Boundary Condition 4

This boundary condition determines the ending point of the curve is tangent to $y = h$ line.

At $x = L$; $y' = 0$

$$4aL^3 + 3bL^2 + 2cL = 0 \qquad (4.6)$$

- Boundary Condition 5

The fifth boundary condition specifies the location of the saddle point of the S-curve.

At $x = s$; $y'' = 0$
$$12as^2 + 6bs + 2c = 0 \qquad (4.7)$$

It can be useful to express x-coordinate of saddle point (s), as percentage of the intake length (L) for different aspects such as comparability of different curves or well-parameterizing the s-curve for S-shape design process. In order to define x-coordinate of saddle point (s) as a ratio of the L, k parameter is specified as a linear variable. Equation 5 shows x-coordinate of saddle point in terms of intake length percentage ratio k,

$$s = kL \qquad (4.8)$$

Substituting the Equation 4.8 into Equation 4.7 the following equation is obtained.

$$12ak^2L^2 + 6bkL + 2c = 0 \qquad (4.9)$$

Substituting all boundary conditions into main 4th order polynomial, 3 equations appears to be solved together in order to obtain 3 unknown parameters (a, b, c).

Firstly, multiplying Equation 4.6 with L, following equation is obtained.

$$4aL^4 + 3bL^3 + 2cL^2 = 0 \qquad (4.10)$$

Substituting Equation 4.10 into Equation 4.5;

$$2c + bL = \frac{4H}{L^2} \qquad (4.11)$$

$$c = \frac{2H}{L^2} - \frac{bL}{2} \qquad (4.12)$$

Parameter c is obtained in terms of b.

Inserting c into 2, Parameter b is obtained in terms of a. (Equation 4.15)

$$4aL^2 + 4bL + \frac{8H}{L^2} - 2bL = \frac{4H}{L^2} \qquad (4.13)$$

$$4aL^2 + 2bL = -\frac{4H}{L^2} \tag{4.14}$$

$$b = -\frac{2H}{L^3} - 2aL \tag{4.15}$$

Substituting this Equation 15 into Equation 4.12; parameter c will be found in terms of a. Hence;

$$c = \frac{3H}{L^2} + aL^2 \tag{4.16}$$

Finally substituting parameter b and c into equation; parameter a is found in terms of k.

$$12ak^2L^2 + 6kM\left(-\frac{2H}{L^3} - 2aL\right) + 2(\frac{3H}{L^2} + aL^2) = 0 \tag{4.17}$$

$$a = \frac{12kH - 6H}{12k^2L^4 - 12kL^4 + 2L^4} \tag{4.18}$$

After applying boundary conditions on quartic function, obtained equations obviously show that , b and c are functions of "k", , "d" and "e" are equal to zero.

$$a = f(k)$$

$$b = f(k)$$

$$c = f(k)$$

$$d = 0$$

$$e = 0$$

According to obtained equations, all S-shape parameters described in terms of k , hence five independent variables of the quadric equation becomes depended to saddle point location percentage (k) of S-shape length on x-coordinate. Thus k parameter is the only one parameter that will be used for varying the S-shape curve. In other words by changing k parameter, saddle point location that defines S-curve divergent to convergent transition point by percentage of the curve length on x-axis, is changed. For different values of k parameter different S-shaped curve alternatives are obtained and represented in Figure 4-11.
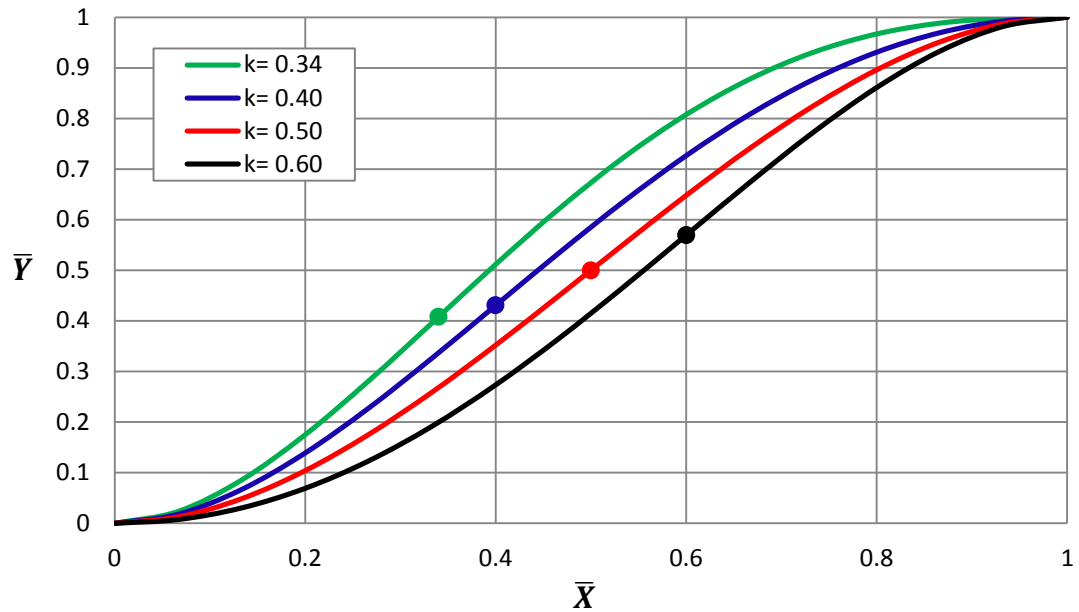
Figure 4-11 The change of S-curve for different saddle point locations.

It can be seen that on Figure 4-11, for different saddle point locations that are described with parameter k, different S-Shaped curves are obtained. Provided that the tangency boundary conditions are satisfied, numerous S-Shaped curves can be defined by changing saddle point location on the S-curve.

4.3 Computational Grid Generation and Boundary Conditions

For design optimization study cartesian mesh is generated over the generic cruise missile body and submerged intake. Initially two refinements are done to partial cells in order to capture the missile body and intake surface moreover during CFD analysis 3 of level 2 adaptive refinements are done at 200th, 400th and 600th iterations. Due to fast convergence characteristics of FloEFD after 800 iterations convergence is handled and analyses are stopped. Total time of creating mesh and analysis a configuration is about lasts 8 hours.
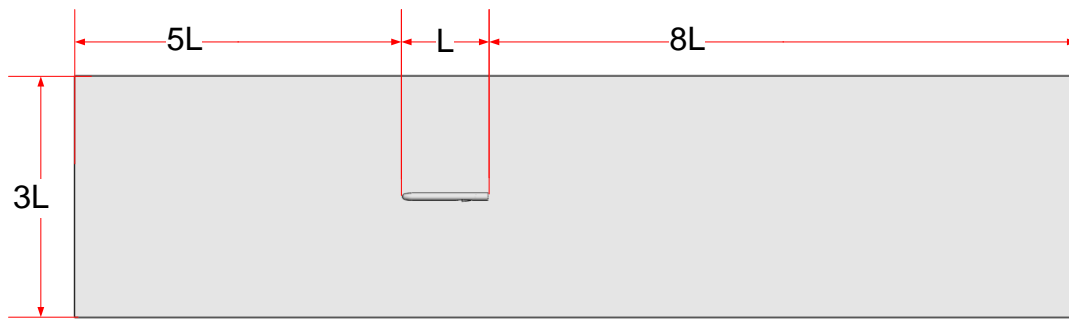
Figure 4-12 Computational Domain Size

Outer surfaces of fluid domain is defined as constant pressure, temperature and velocity as boundary condition since these surfaces are far enough from missile geometry surfaces. No slip wall boundary condition is applied on missile surfaces. Mach outlet boundary condition is applied on engine face considering throat mass flow rate for intake analysis.

Figure 4-13 Mach Outlet Boundary Condition Surface

4.3.1 Grid Independence Study

In order to get CFD results independent of grid size and density, grid convergence analysis are done for the generic submerged intake before design optimization work. Six different cartesian grids of submerged intake are examined to determine minimum grid size in order to reduce computational time and avoid from unnecessary CPU overloading. The effects of total cell number on PR values of six different grids are given at Table 4-3. Change of PR value according to total cells is represented at Figure 4-14.

Table 4-3 Grid Independency Study

Grid Number	Total Cells	PR
1	69,536	0.86842
2	177,038	0.87834
3	418,712	0.89608
4	1,483,796	0.90133
5	2,788,301	0.90136
6	5,032,488	0.90139
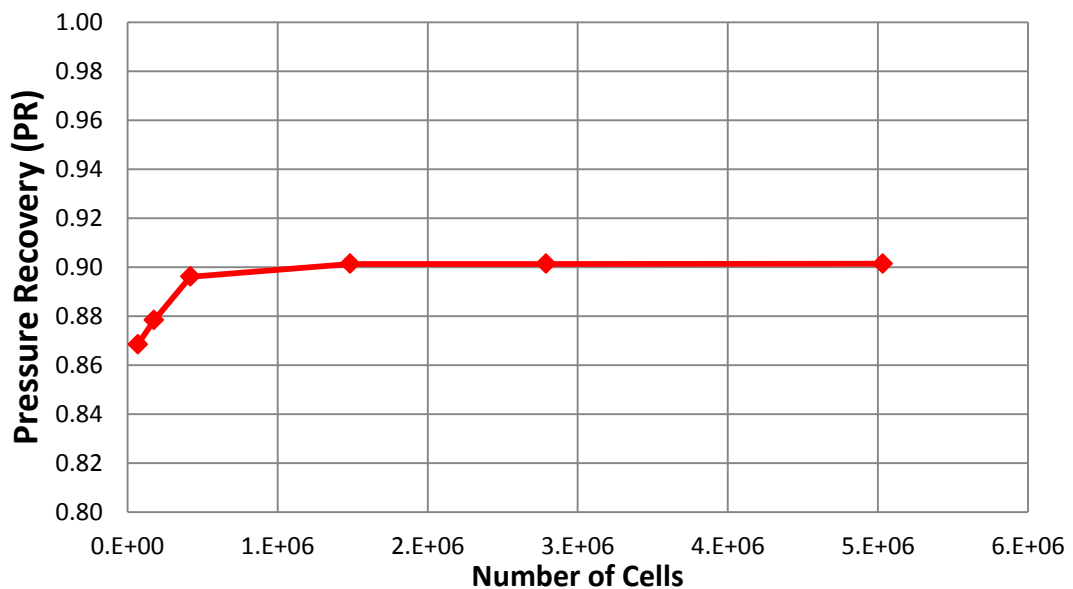
Figure 4-14 Grid Independency Study
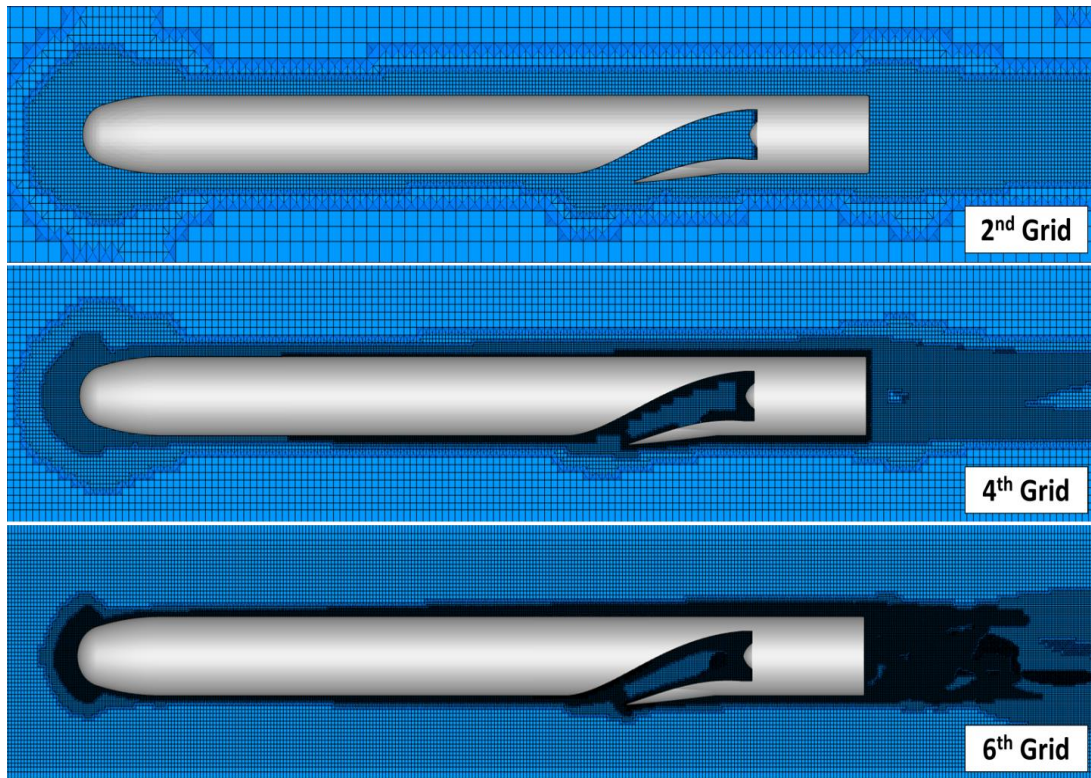
Figure 4-15 Representations of Different Grids

It can be seen that pressure recovery coefficient (PR) is sensitive to mesh quality. First three grid types gave unsatisfactory results even though 4th, 5th and 6th grids gave nearly same satisfactory PR results. In order to save both time and computer power, 4th grid type is chosen for the rest of the numerical analysis and optimization study in this thesis. Different grid densities are given in Figure 4-15.

CHAPTER 5

VALIDATION STUDY OF DEVELOPED DESIGN METHOD

In this section, validation of developed design study is presented. This study will be used as a basis work for application of this method for future studies. Furthermore, in order to understand the optimization algorithm, geometric constrains are not used. All geometric design parameters are set to be free during the optimization process and all CFD settings mentioned in Chapter 4 are used in this study. Convergence is obtained in four optimization step and results are discussed.

5.1 Aim of Validation Study

This study is done for two reasons, the first and the most important one is to check the design optimization algorithm whether it is work correctly and the second one is to understand the effect of the parameters and developed design algorithm, during optimization steps. In order to achieve this aims, geometric constraints and objective penalties are not used and optimization algorithm is set to be free to change geometric parameters to maximize PR coefficient. Six different geometric parameters are chosen for optimization study and these parameters are changed according to optimization algorithm. S-shape parameter (k), motor tangent length (mtl), diffuser length (dfl), throat section lengths (e_1, e_2, e_3) are design variables for the validation study. Other parameters are kept constant. Basis geometry is constructed by using these parameters. Geometric details of the basis geometry are given in Table 5-1

Table 5-1 Parametric Intake Geometric Parameters for Initial Geometry

Parameter	Value
S-Shape Parameter (k)	0.40
Motor Tangent Length (mtl)	50 mm
Diffuser Length (dfl)	700 mm
Throat Length.1 (e_1)	49 mm
Throat Length.2 (e_2)	83 mm
Throat Length.3 (e_3)	107 mm
Upper Lip NACA Type	NACA0012
Upper Lip Profile Length	33.3 mm
Lower Lip NACA Type	NACA0012
Lower Lip Profile Length	116.6 mm

It is expected from this validation study the design optimization method will find an optimum geometry that is similar to pitot type intake that was explained at introduction section. Since no geometric limitations are used, the algorithm will increase the offset of the intake, from the body. This situation can be explained with boundary layer effects in the submerged intake. If entrance of the intake located so close the missile body, developed boundary layer from the missile body sucked into the intake and low energy fluid will reduce the PR at the AIP. So this phenomenon will be as a validation study of this steepest descent optimization algorithm whether it can be used intake performance analysis. If design algorithm will increase the offset of the submerged intake from the missile body just like pitot type intake, it can be said that the algorithm is working correctly.

5.2 Objective Function

Since there are no limitations and penalties for this parameter free validation study the objective function equals to PR. In this study objective function will be maximized.

$$f(\vec{X}) = PR \qquad\qquad (5.1)$$

5.3 Results and Discussion

Design optimization algorithm applied to initial geometry in order to find the best intake geometry with no geometric and performance limits. The study converged in 4 iterations. In every optimization step, approximately 15 geometries are analyzed by using CFD tool. Totally after about 80 CFD runs final geometry is determined. The geometries regarding to Configuration Number (CN) are found the best against the others in every optimization step. Their geometric details and performance results are tabulated at Table 5-2 and Table 5-3. Front views of these geometries are represented at Figure 5-1.

Table 5-2 Geometric details of Intakes Obtained from Optimization Steps (mm)

Geometry	mtl	dfl	k	e_1	e_2	e_3	Offset	A_{th} (mm²)
CN-1	50.00	700.00	40.0	49.00	83.00	107.00	0.117D	22185.93
CN-2	49.23	701.48	41.08	47.08	82.88	103.11	0.119D	21049.31
CN-3	47.55	707.83	42.57	57.94	89.82	105.12	0.181D	24398.36
CN-4	44.24	743.56	49.69	59.77	92.33	99.11	0.262D	23679.51
CN-5	44.24	743.56	50.0	60.77	92.33	99.11	0.264D	23835.20
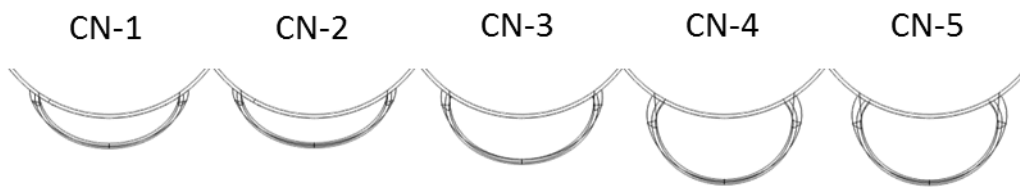
Figure 5-1 Geometries of Intakes Obtained from Optimization Steps

Table 5-3 Performances of Intakes that are Obtained from Optimization Steps

Geometry	$\dot{m}_{corr}$ (kg/s)	DC	PR
CN-1	4.28	0.0343	0.9104
CN-2	4.26	0.0358	0.9153
CN-3	4.47	0.0293	0.9240
CN-4	4.34	0.0203	0.9484
CN-5	4.34	0.0203	0.9495

PR improvement by optimization algorithm is represented in Figure 5-2. It can be seen that from Table 5-3 PR is totally increased about 4.3% at the end of optimization iterations. Correspondingly 40% distortion coefficient enhancement is achieved from final geometry CN-5 compared to initial configuration. Corrected mass flow rate remained nearly same value. Small increase of corrected mass flow rate can be interpreted as throat area of final geometry bigger than initial configuration.
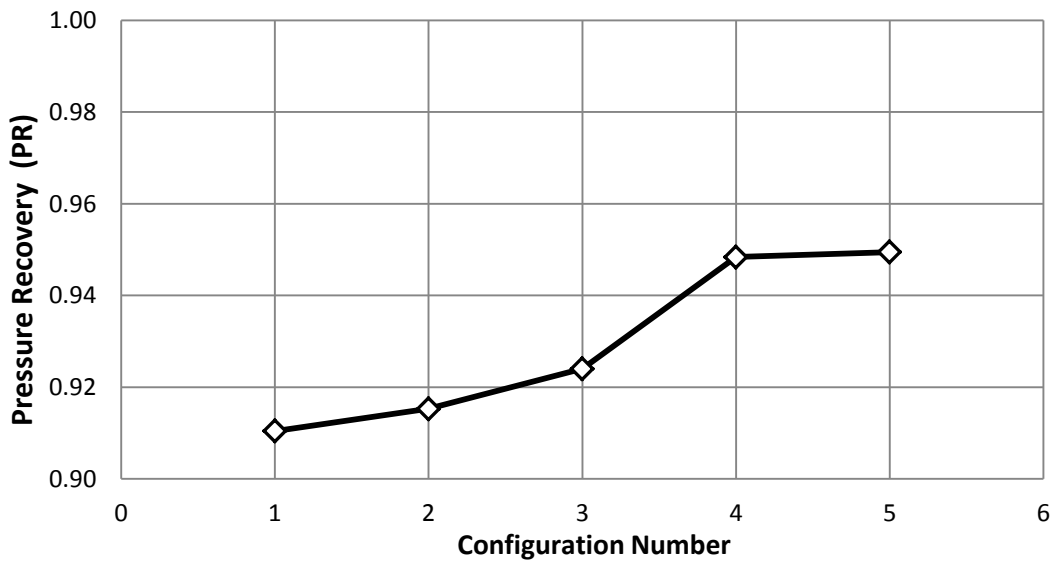
Figure 5-2 Pressure Recovery Coefficients of Intakes on Optimization Steps

In this study optimization algorithm is validated. As it expected the final geometry intake shape is similar to pitot type intake that has better performance compared to submerged intakes. Optimization algorithm with no limitations increased the intake offset from the missile body. This caused performance improvement without given any geometric limitations. In next design study geometric limitations are applied to optimization algorithm in order to optimize shape geometry of submerged intake.

CHAPTER 6

APPLICATION OF INTAKE DESIGN

In this section, validated optimization algorithm is used for designing a subsonic submerged intake according to given flight conditions and engine requirements. Total offset from missile body is limited in this study. Design optimization is conducted at cruise flight conditions given in Chapter 4. Geometric details of optimum intakes on each optimization step are given in detail and their performance parameters are discussed. Finally, future work about enhancement of this study is mentioned.

6.1 Initial Geometry and Geometric Limitations

In this chapter, an application of designing a subsonic submerged intake by using design optimization algorithm is done by applying geometric limitations. Considering launch platforms and diameter of canister of this kind of missiles, intake offset from missile body is determined and limited by 0.156 diameter of missile. Offset limitation represented in Figure 6-1. In order to keep corrected mass flow rate constant, throat area limited to 24081 mm^2. Throat parameters e_1 and e_2 are changed during design process by optimization algorithm. The third throat parameter, e_3 is set free and it changed automatically according to e_1 and e_2 in order keep throat area constant. Random subsonic intake geometry is chosen as initial geometry for design optimization algorithm. S-shape parameter "k" is chosen as 0.31 that is considered as inferior s-shape in order to provide flow separation inside the intake that will be optimized and reattached by the optimization algorithm.

71
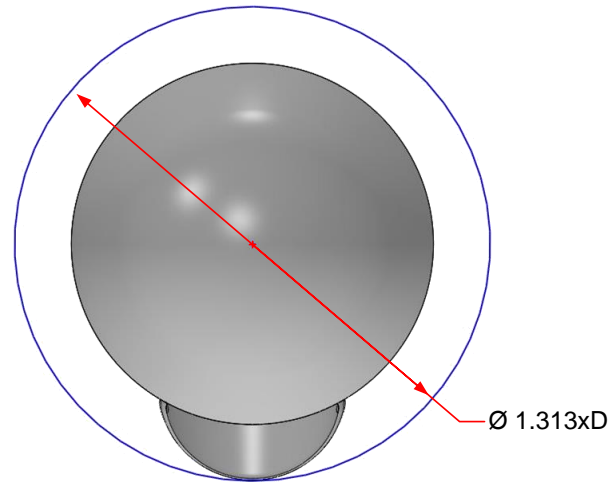
Figure 6-1 Geometric Limit of Intake Offset Diameter

S-Shape is also limited to $k < 0.67$ provide S-shape tangency to the missile body. The limit of S-Shape parameter is represented in Figure 6-2 and out of limits also can be seen in this figure. S-Shape parameter is remained defined region during the optimization process.
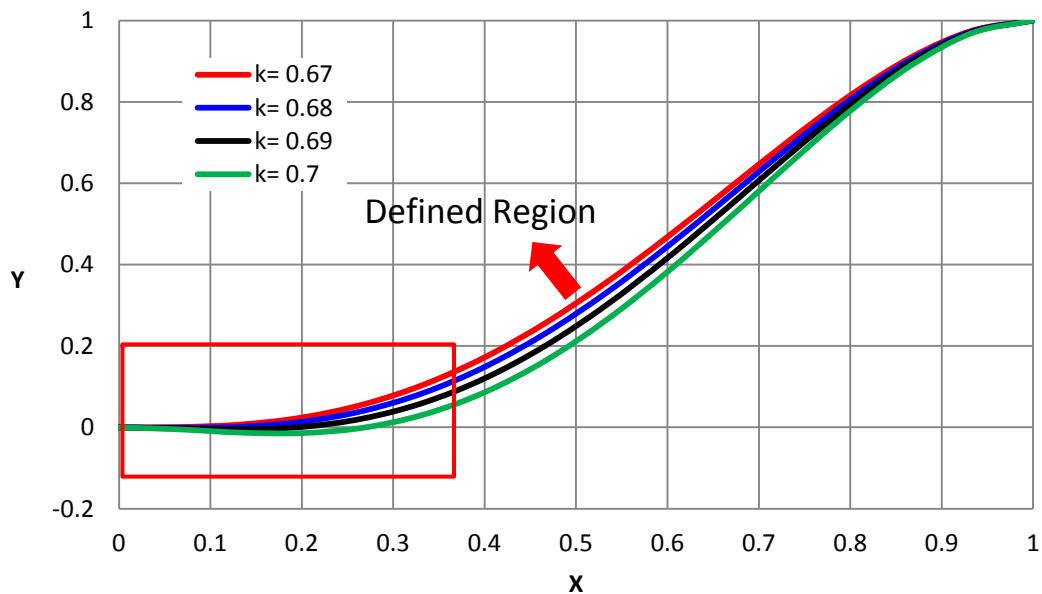
Figure 6-2 Geometric Limit of S-Shape Parameter

Throat parameters e_1, e_2 and e_3 are given as 80.0, 94.08 and 88.06 respectively in order to provide throat area at value about 24081 mm^2. Geometric details of initial geometry are given in Table 6-1. Lip parameters are determined as same as with the study at Chapter 5.

72

Table 6-1 Geometric Parameters of Initial Geometry

Geom	mtl	dfl	k	e_1	e_2	e_3	Offset	A_{th} (mm²)
G_0	2.00	700.0	0.31	80.00	94.08	88.06	0.156D	24081

6.2 Objective Function

Objective function is determined to represent performance of submerged intake and geometric limitations not only for designing high performance intake but also design appropriate geometry in design limits. PR and DC performance parameters, mentioned before, defined with different weights to calculate objective function. Also geometric penalty parameter is added to calculation of objective function. Objective function determined as;

$$f(\vec{X}) = 100 * (1 - PR) + 10 * (DC_{DPCP}) + p_1$$

p_1 is geometric penalty value of "k" (S-Shape Parameter) will be added to objective function when k parameter is above 0.6742 value. This is an upper limit of S-shape parameter since S-Shape orientation is corrupted above this value. This penalty is given at first iteration about value 3.

6.3 Optimization Results

Intake optimization study converged in 5 iterations. In every optimization step, approximately 12 geometries are analyzed by using CFD tool. Totally after about 60 CFD runs, convergence is obtained. The geometries regarding to Configuration Number (CN) are found the best against the others in every optimization step and their performance results are tabulated and represented below.

Optimization algorithm is started by using initial geometry. First geometric design parameters are changed with small amounts in order to calculate gradient direction that directs the local optimum. After calculating gradient direction, line search algorithm is applied to initial geometry to find the optimum geometry of first optimization step. Algorithm repeated until convergence obtained.

The first optimization step is presented in Table 6-2.

Table 6-2 Gradient and Line Search Calculations for Optimization Step 1

OPTIMIZATION STEP 1										
Geom	**dfl**	**k (%)**	**e_1**	**e_2**	**e_3**	**$\dot{m}_{corr}$**	**PR**	**DC_{DPCP}**	**OBJ**	**GRAD**
G_0	700.0	31.00	80.00	94.08	88.07	4.43	0.8882	0.0478	11.66	
Δ_1	688.0	32.00	80.00	94.08	88.07	4.43	0.9036	0.0418	10.06	0.0940
Δ_2	714.0	30.00	80.00	94.08	88.07	4.43	0.8826	0.0512	12.25	
Δ_3	694.0	31.00	84.00	94.08	86.09	4.43	0.8991	0.0445	10.54	0.0096
Δ_4	707.0	31.00	76.00	94.08	90.14	4.43	0.8907	0.0509	11.44	
Δ_5	694.0	31.00	80.00	98.08	86.09	4.43	0.9003	0.0441	10.41	0.0123
Δ_6	707.0	31.00	80.00	90.08	90.14	4.43	0.8892	0.0480	11.56	

Line search algorithm applied to first optimization step and represented in Figure 6-3.
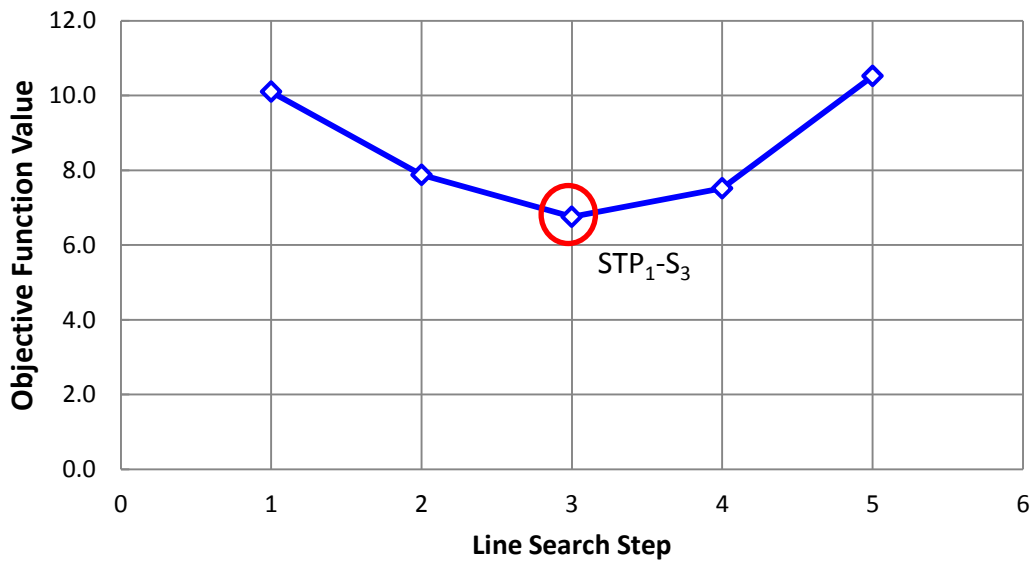
Figure 6-3 Line Search Through the Gradient Direction for Optimization Step 1

The geometry that obtained from optimization step 1 is used as an initial point of next optimization step. The gradient search process for optimization step 2 is presented in Table 6-3.

Table 6-3 Gradient and Line Search Calculations for Optimization Step 2

Geom	dfl	k (%)	e_1	e_2	e_3	$\dot{m}_{corr}$	PR	DC_{DPCP}	OBJ	GRAD
STP$_1$-S$_3$	553.5	52.99	82.25	96.96	85.54	4.43	0.9356	0.0313	6.76	
Δ_1	533.0	56.99	82.25	96.96	85.54	4.43	0.9331	0.0358	7.05	0.0087
Δ_2	570.0	48.99	82.25	96.96	85.54	4.43	0.9281	0.0316	7.50	
Δ_3	543.5	52.99	86.25	96.96	83.68	4.43	0.9279	0.0362	7.57	-0.0136
Δ_4	562.5	52.99	78.25	96.96	87.50	4.43	0.9339	0.0218	6.83	
Δ_5	543.5	52.99	82.25	100.9	83.68	4.43	0.9295	0.0334	7.39	-0.0058
Δ_6	562.5	52.99	82.25	92.9	87.50	4.43	0.9323	0.0306	7.07	

Caption: OPTIMIZATION STEP 2 (header row spanning table)

Line search algorithm applied to second optimization step through the gradient direction represented in Figure 6-4.
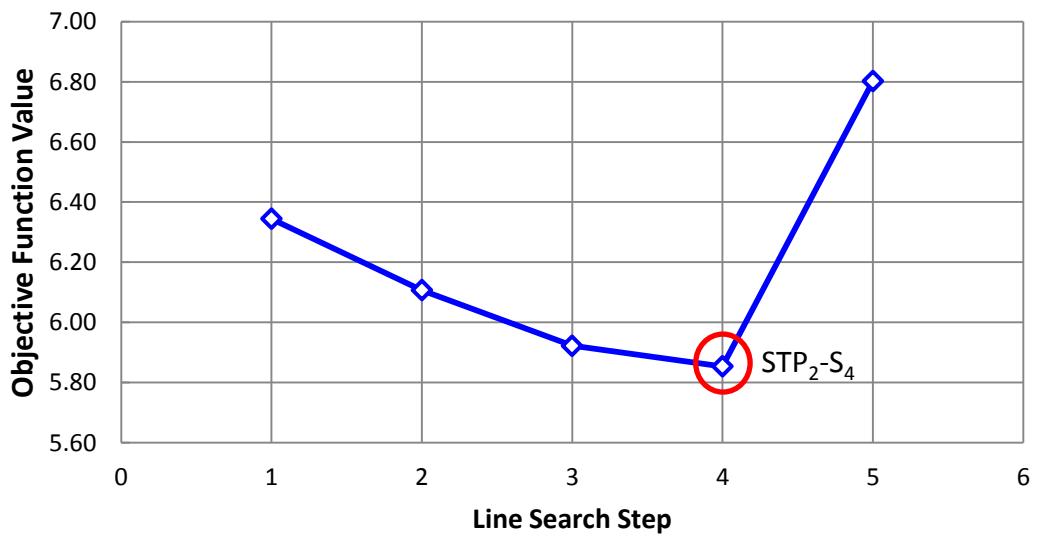
Figure 6-4 Line Search Through the Gradient Direction for Optimization Step 2

STP$_2$-S$_4$ geometry is obtained from second optimization step that used as the initial geometry for optimization step 3. The gradient search table for optimization step 3 is presented in Table 6-4.

Table 6-4 Gradient and Line Search Calculations for Optimization Step 3

OPTIMIZATION STEP 3										
Geom	**dfl**	**k (%)**	**e_1**	**e_2**	**e_3**	**$\dot{m}_{corr}$**	**PR**	**DC_{DPCP}**	**OBJ**	**GRAD**
STP_2-S_4	556.0	58.46	73.64	93.31	91.82	4.43	0.9442	0.0271	5.85	
Δ_1	544.0	60.46	73.64	93.31	91.82	4.43	0.9424	0.0313	6.08	-0.0121
Δ_2	567.0	56.46	73.64	93.31	91.82	4.43	0.9447	0.0262	5.79	
Δ_3	549.0	58.46	76.64	93.31	90.20	4.43	0.9405	0.0253	6.20	-0.0103
Δ_4	564.5	58.46	70.64	93.31	93.50	4.43	0.9438	0.0227	5.84	
Δ_5	549.0	58.46	73.64	96.31	90.20	4.43	0.9402	0.0251	6.23	-0.0103
Δ_6	564.0	58.46	73.64	90.31	93.50	4.43	0.9438	0.0253	5.87	

Line search through the obtained gradient direction for optimization step 3 is represented in Figure 6-5.
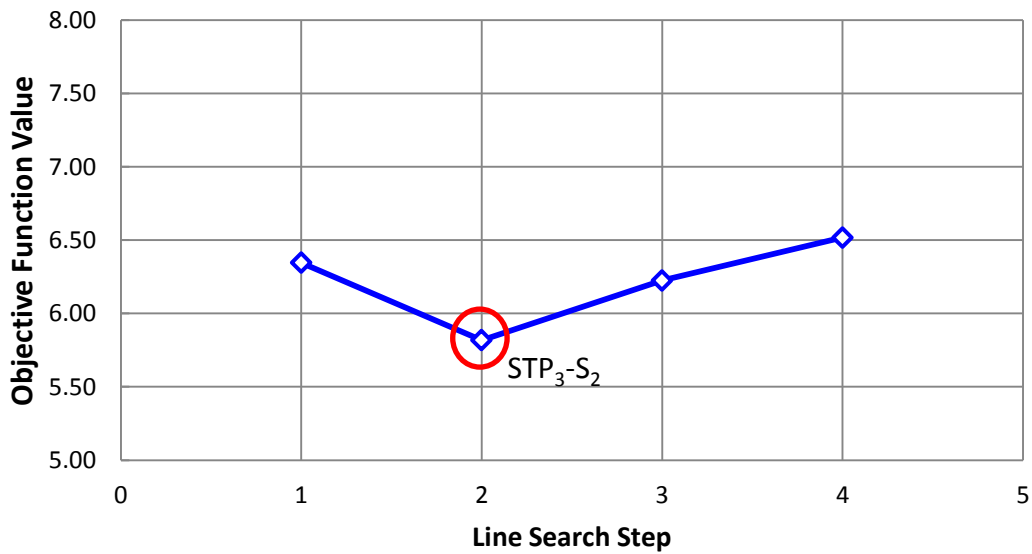
Figure 6-5 Line Search Through the Gradient Direction for Optimization Step 3

STP_3-S_2 geometry is obtained from third optimization step that is used as the initial geometry for optimization step 3. The gradient search table for optimization step 4 is presented in Table 6-5.

Table 6-5 Gradient and Line Search Calculations for Optimization Step 4

OPTIMIZATION STEP 4										
Geom	**dfl**	**k (%)**	**e_1**	**e_2**	**e_3**	**$\dot{m}_{corr}$**	**PR**	**DC_{DPCP}**	**OBJ**	**GRAD**
STP_3-S_2	579.0	56.04	71.59	91.25	94.14	4.43	0.9443	0.0247	5.82	
Δ_1	569.0	58.04	71.59	91.25	94.14	4.43	0.9453	0.0208	5.68	0.0194
Δ_2	589.0	54.04	71.59	91.25	94.14	4.43	0.9405	0.0182	6.13	0.0194
Δ_3	574.0	56.04	73.59	91.25	93.00	4.43	0.9445	0.0273	5.83	0.0137
Δ_4	584.0	56.04	69.59	91.25	95.32	4.43	0.9403	0.0175	6.15	0.0137
Δ_5	574.0	56.04	71.59	93.25	93.00	4.43	0.9441	0.0273	5.86	0.0113
Δ_6	584.0	56.04	71.59	89.25	95.32	4.43	0.9405	0.0178	6.12	0.0113

Line search through the obtained gradient direction for optimization step 4 is represented in Figure 6-6.
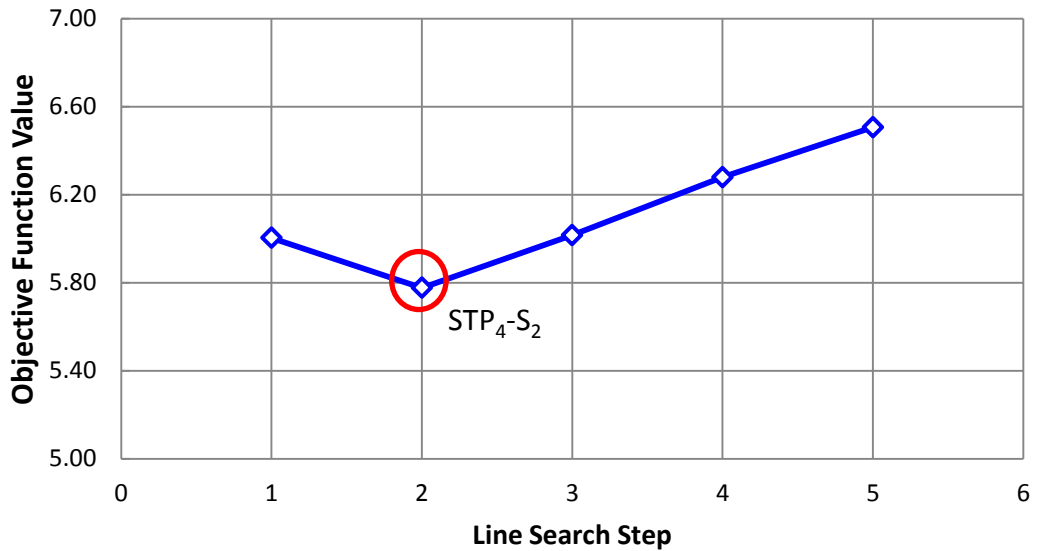
Figure 6-6 Line Search Through the Gradient Direction for Optimization Step 4

STP_4-S_2 geometry is obtained from fourth optimization step. The gradient search table for optimization step 5 is presented in Table 6-6.

Table 6-6 Gradient and Line Search Calculations for Optimization Step 5

OPTIMIZATION STEP 5										
Geom	dfl	k (%)	e_1	e_2	e_3	$\dot{m}_{corr}$	PR	DC_{DPCP}	OBJ	GRAD
STP$_4$-S$_2$	568.0	57.39	72.54	92.04	93.15	4.43	0.9449	0.0265	5.78	
Δ_1	562.0	58.39	72.54	92.04	93.15	4.43	0.9448	0.0238	5.76	0.0068
Δ_2	573.0	56.39	72.54	92.04	93.15	4.43	0.9444	0.0277	5.83	
Δ_3	566.0	57.39	73.54	92.04	92.59	4.43	0.9445	0.0270	5.82	0.0167
Δ_4	571.0	57.39	71.54	92.04	93.72	4.43	0.9423	0.0244	6.01	
Δ_5	566.0	57.39	72.54	93.04	92.59	4.43	0.9447	0.0265	5.80	-0.0051
Δ_6	571.0	57.39	72.54	91.04	93.72	4.43	0.9451	0.0250	5.74	

Line search through the obtained gradient direction for optimization step 4 is represented in Figure 6-7
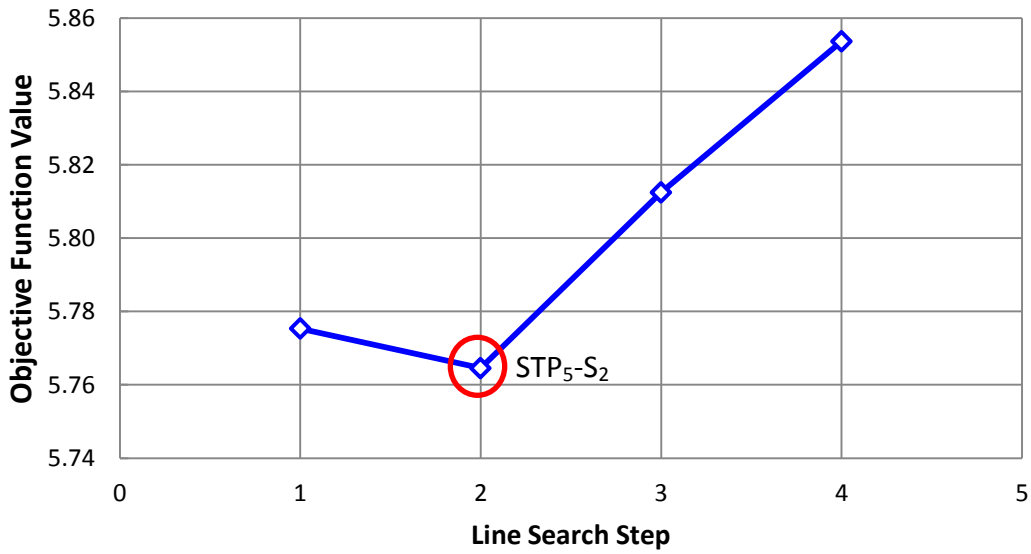
Figure 6-7 Line Search Through the Gradient Direction for Optimization Step 5

After 5 optimization step, optimization algorithm converged and final geometry "STP$_5$-S$_2$" is obtained. Geometric details of final geometry is given in Table 6-7

Table 6-7 Final Geometry obtained from Optimization Process

Geom	dfl	k	e_1	e_2	e_3	$\dot{m}_{corr}$	PR	DC_{DPCP}	OBJ
STP_5	568.0	0.5744	72.65	92.00	93.11	4.43	0.9450	0.0262	5.76

Geometric details of configurations that are obtained in each optimization step are also given with the initial and final geometry in Table 6-8.

Table 6-8 Geometric details of Intakes Obtained from Each Optimization Steps

Geom	dfl	k (%)	e_1	e_2	e_3	$\dot{m}_{corr}$	PR	DC_{DPCP}	OBJ
G_0	700.0	31.00	80.00	94.08	88.07	4.43	0.8882	0.0478	11.66
STP_1	553.5	52.99	82.25	96.96	85.55	4.43	0.9356	0.0313	6.76
STP_2	556.0	58.46	73.64	93.31	91.82	4.43	0.9442	0.0271	5.85
STP_3	579.0	56.04	71.59	91.25	94.14	4.43	0.9443	0.0247	5.82
STP_4	568.0	57.39	72.54	92.04	93.15	4.43	0.9449	0.0265	5.78
STP_5	568.0	57.44	72.65	92.00	93.11	4.43	0.9450	0.0262	5.76

Since PR and DC improvement, objective function decreased at each optimization step. Corrected mass flow rate value remains constant during optimization steps can be seen in Table 6-8. As optimization algorithm converged, objective function is totally reduced about 50.6% at the end of iterations. Correspondingly 6.4% pressure recovery coefficient recruitment and about 45% distortion coefficient enhancement are achieved at the end of optimization process compared to initial intake configuration. Intake geometries obtained from optimization steps are given in Figure 6-8.
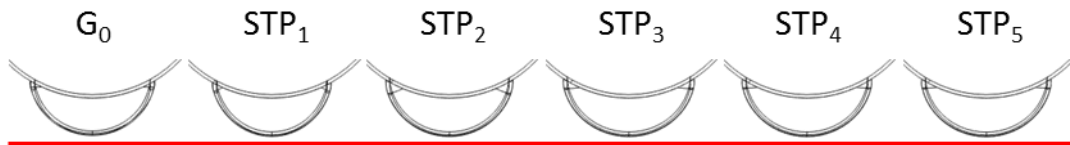
Figure 6-8 Intake Geometries Obtained from Each Optimization Step

The geometric differences of the intakes obtained at each iteration compared with the initial geometry, given in detail from the symmetry plane and throat sections in Figure 6-9 and Figure 6-10 respectively.
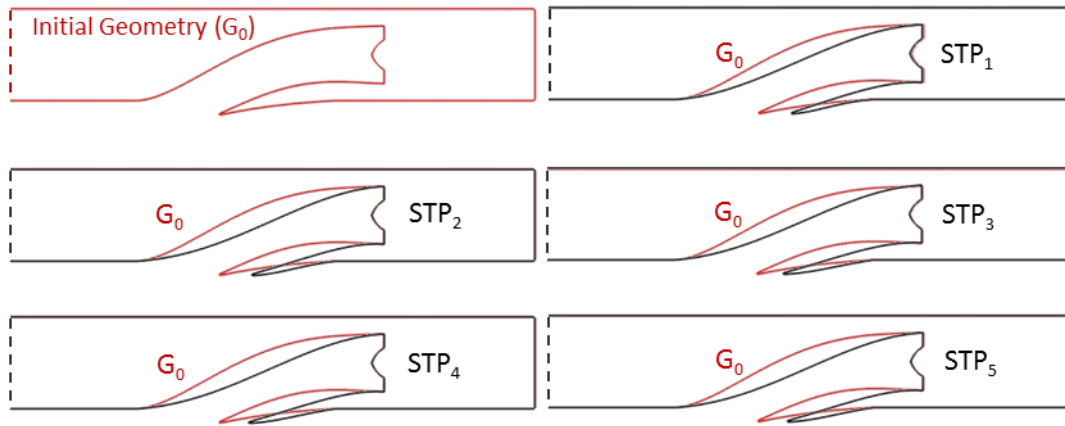
Figure 6-9 Comparison of Intake Geometries Obtained from Each Optimization Step
with Initial Geometry
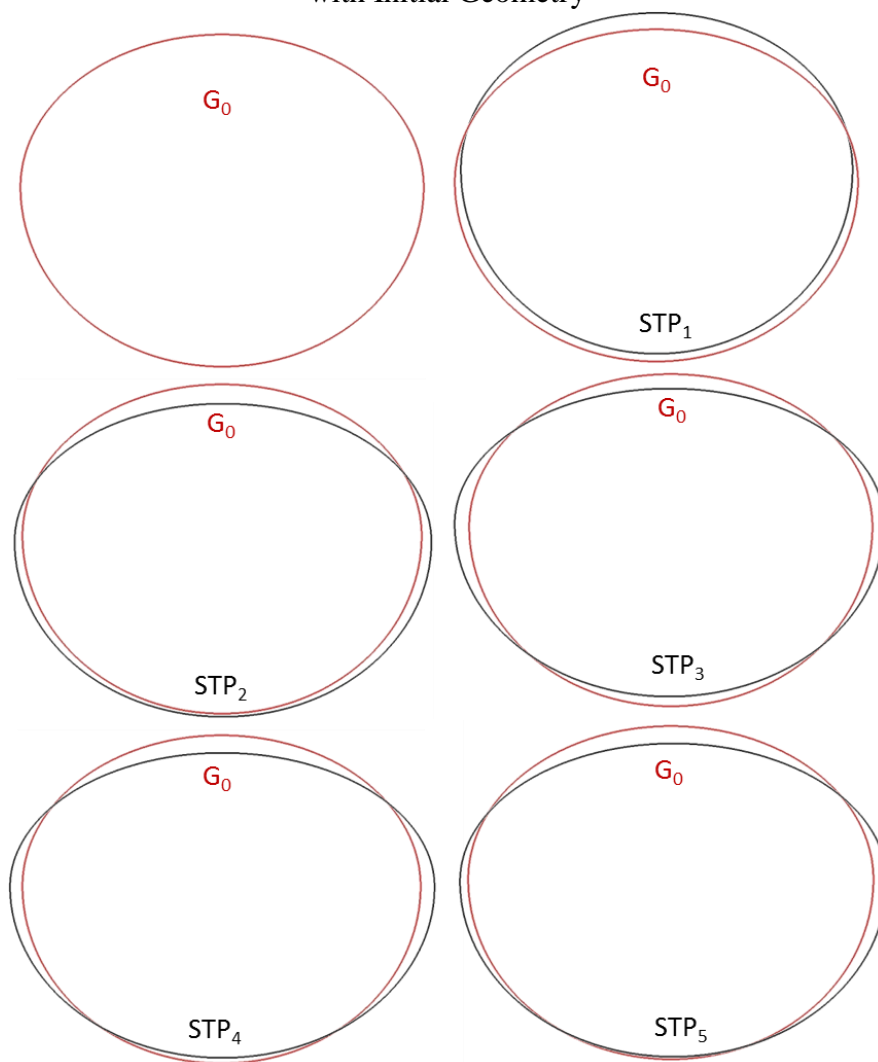
Figure 6-10 Throat Section Comparison of Intake Geometries Obtained from
Optimization Steps

80

Normalized objective function values for each optimization steps are presented in Figure 6-11.
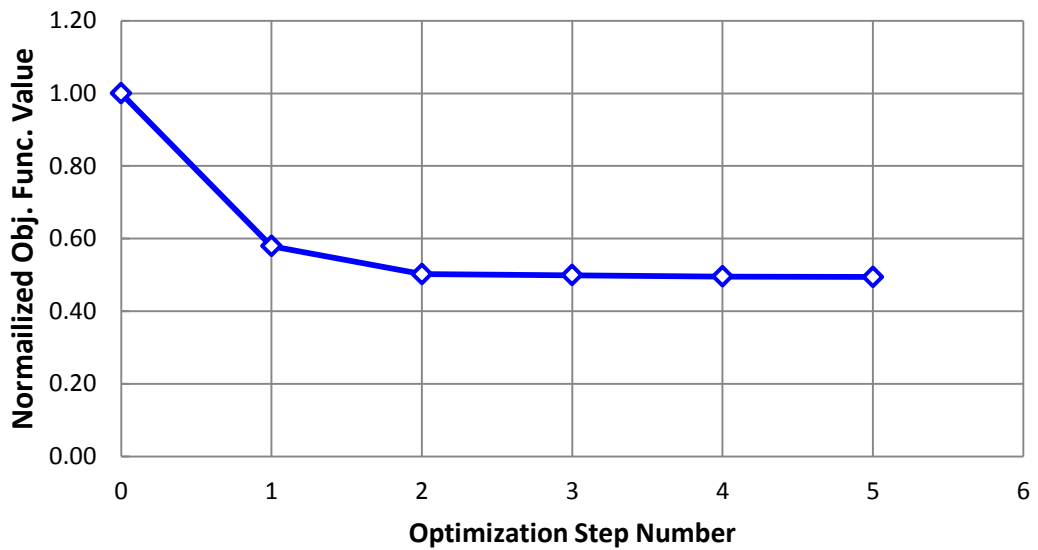
Figure 6-11 Normalized Objective Function Values on Each Optimization Steps

Relatively pressure recovery improvement during optimization process can be seen in Figure 6-12
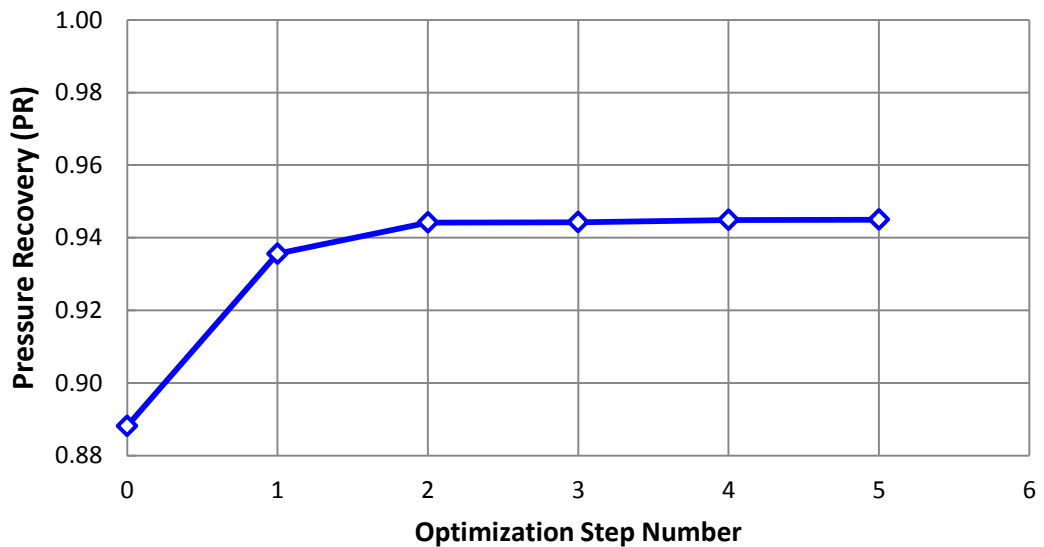
Figure 6-12 Pressure Recovery Values on Each Optimization Steps

Change of distortion coefficient is given during the optimization process is given in Figure 6-13. As it mentioned before reduction of this coefficient represents flow uniformity on the AIP. According to Figure 6-13 approximately 45% grade of DC improvement is obtained at the end of optimization algorithm.
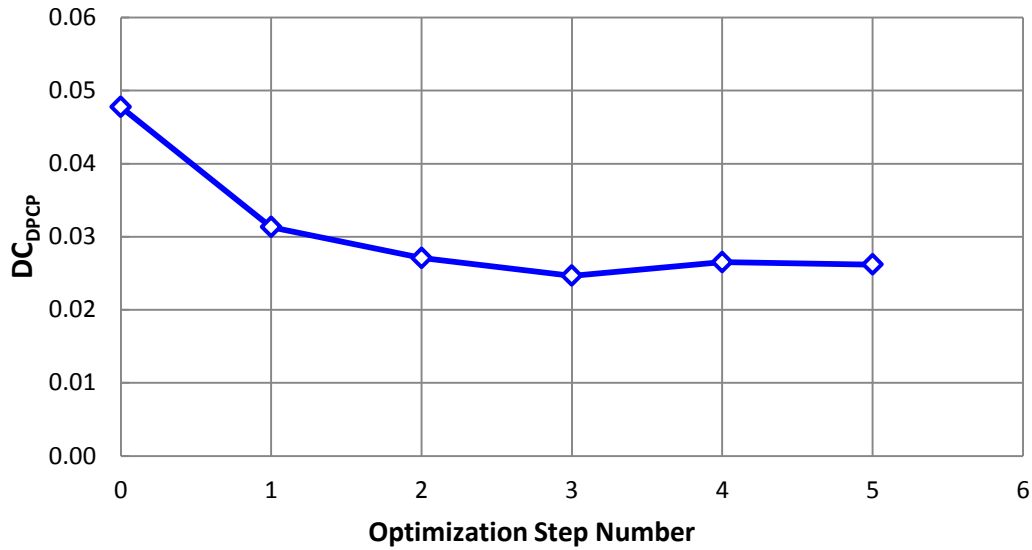
Figure 6-13 Distortion Coefficient Values on Each Optimization Steps

Since throat area is remained constant at each geometry that are analyzed during all steps of optimization algorithm, and the same boundary conditions applied for each geometry, corrected mass flow rate value remained constant during optimization process. Constant value of corrected mass flow rate on each optimization step is represented in Figure 6-17
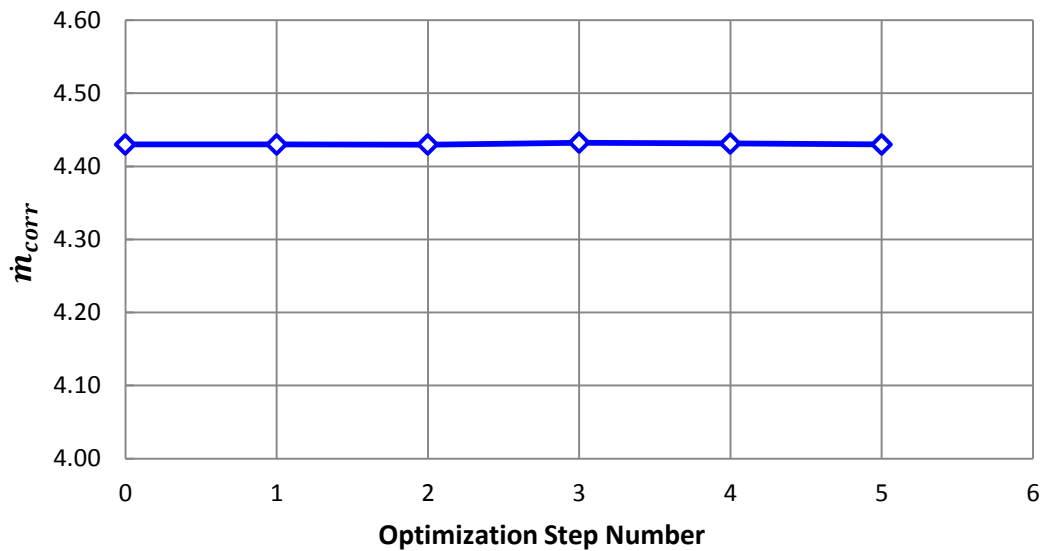
Figure 6-14 Corrected Mass Flow Rate Values on Each Optimization Steps

Change of design parameters at each optimization steps are represented below. The S-shape parameter "k" is started from 0.31 at the initial geometry and finally reached and converged to the 0.574 at the end of optimization process. (Figure 6-15)
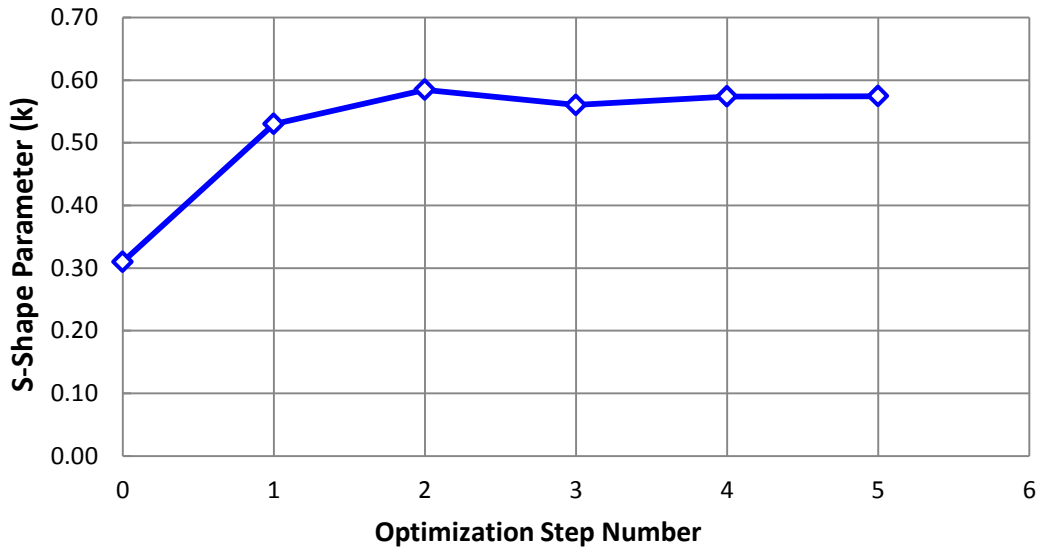
Figure 6-15 Change of S-Shape Parameter during Optimization Steps

The change of throat section parameters e_1, e_2 and e_3 are presented in Figure 6-16.
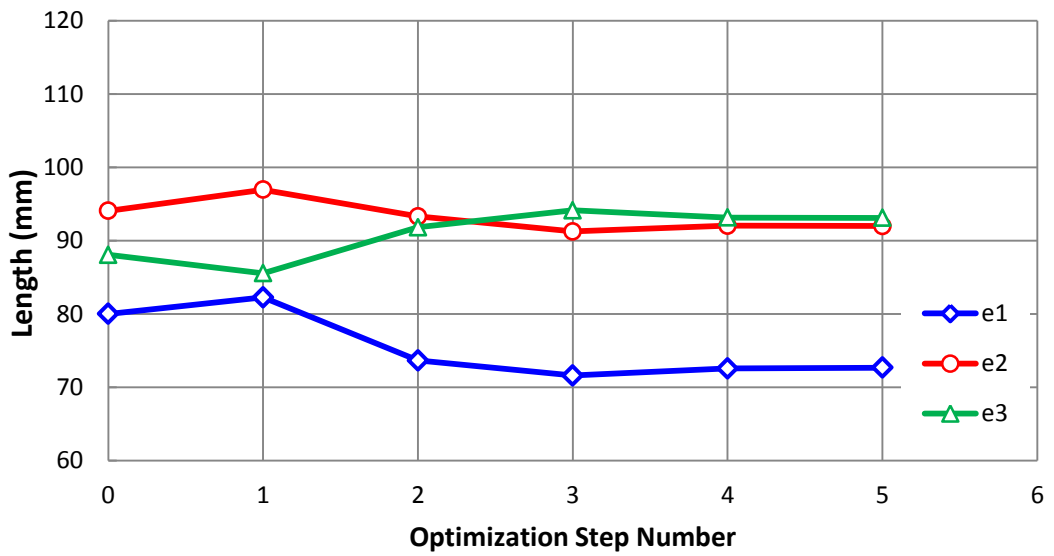
Figure 6-16 Change of Throat Parameters during Optimization Steps

83

The change of diffuser length at each optimization step is represented in Figure 6-17.
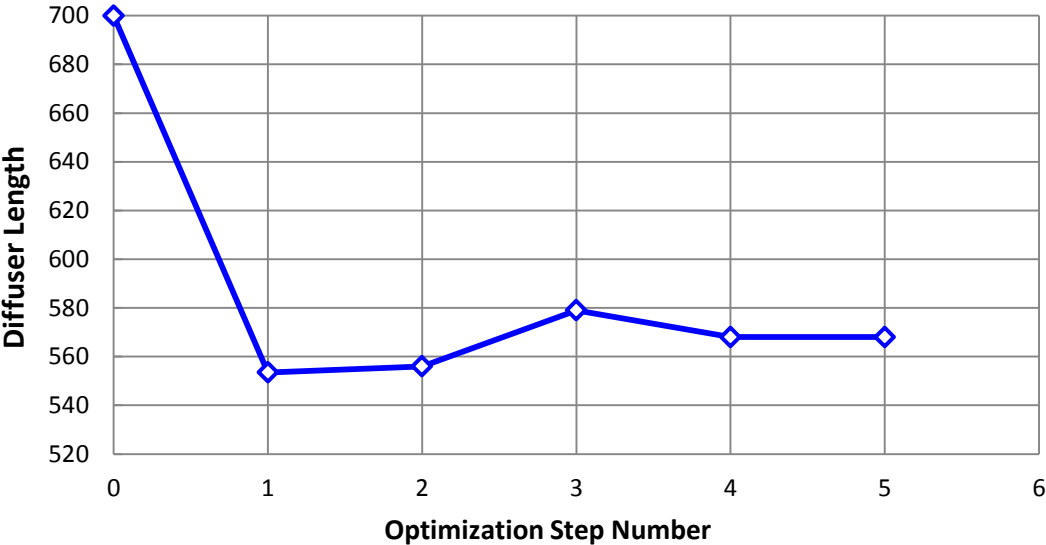
Figure 6-17 Change of Diffuser Length Value during Optimization Steps

In this optimization study axial force coefficient is not considered as an intake performance parameter so it is not included objective function calculations. However in design of cruise missiles axial force the one of the most important design parameter. Hence in this optimization study total axial force coefficient of the cruise missile calculated for each optimization step and compared to each other. axial force coefficient of intake with the missile body obtained each optimization step is tabulated in Table 6-9 and change of axial force coefficient represented in Figure 6-18

Table 6-9 Cruise Missile Axial Force Coefficient Obtained each Optimization Step

Opt. Step	Geometry	C_A
-	G_0	0.9922
1	STP_1	0.8827
2	STP_2	0.8698
3	STP_3	0.8631
4	STP_4	0.8643
5	STP_5	0.8640
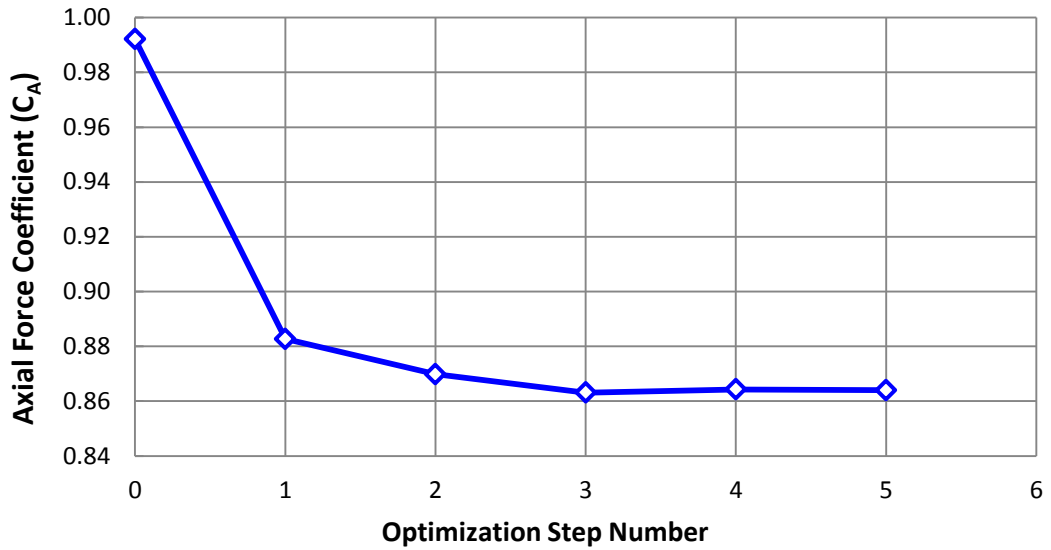
Figure 6-18 Change of Axial Force Coefficient of Cruise Missile During Optimization Steps

At the end of intake performance optimization process 12.8% axial force coefficient improvement on total cruise missile is obtained. It can be said that from the analysis results PR enhancement triggered axial force improvement since flow reattachment from separation reduces axial force in the diffuser.

Performance parameter values and improvement of each parameter compared between initial and final geometry obtained by using optimization algorithm, tabulated at Table 6-10 at the end of the optimization process.

Table 6-10 Performance of Intakes Obtained from Optimization Steps

Param.	Initial Geometry	Final Geometry	Improvement (%)
PR	0.8882	0.9450	6.40
DC(60)	0.4059	0.2173	46.46
DC_{DPCP}	0.0478	0.0262	45.13
CA_{body}	0.9922	0.8640	12.91

Flow visualization study is conducted to AIP of each obtained geometry is given at Figure 6-19. Performance enhancement such as total pressure increase and distribution uniformity can be seen from this figure.
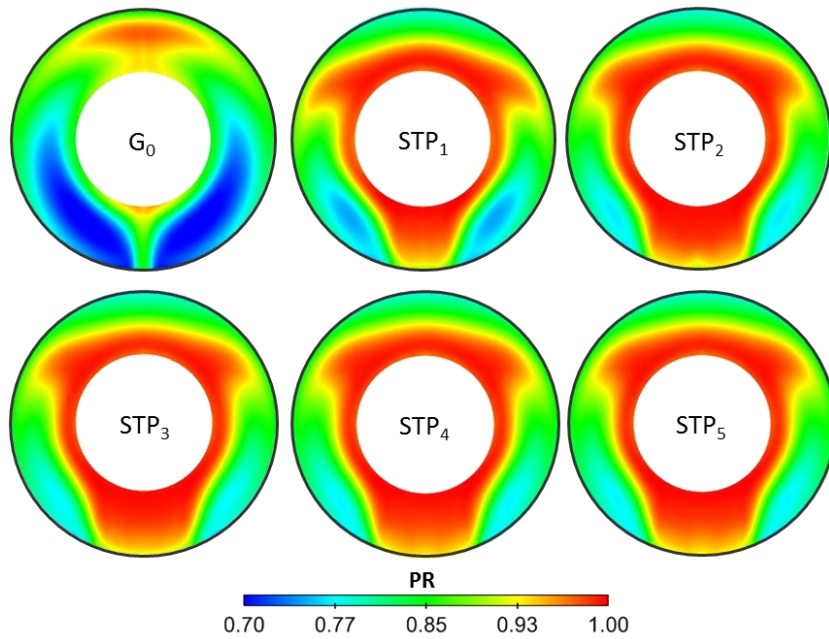
Figure 6-19 Total Pressure Distribution on AIP for each Optimization Iterations

In order to understand performance improvement and enhancement achieved from design optimization iterations, 4 sections are determined in the diffuser section of intakes and each of these sections are investigated. Sections are cut according to diffuser length in order to compare each intake configuration. Section stations are depicted and demonstrated at Figure 6-20 and Figure 6-21. Sections are cut from same locations on each intake based on diffuser length (dfl) in order to compare flow vortices and separation regions inside. Sections for each intake configuration obtained from every optimization step represented in Figure 6-22 to Figure 6-27
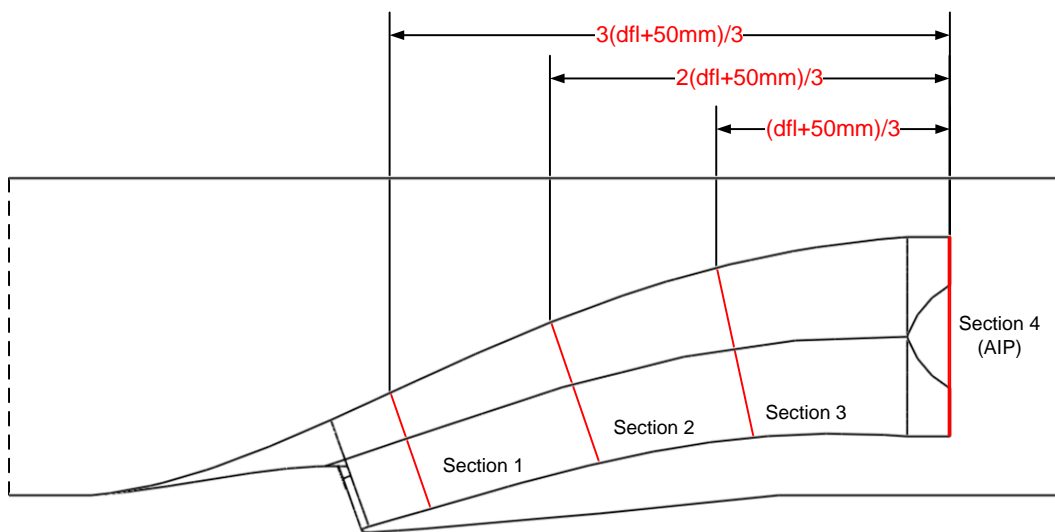
Figure 6-20 Sections on a Configuration
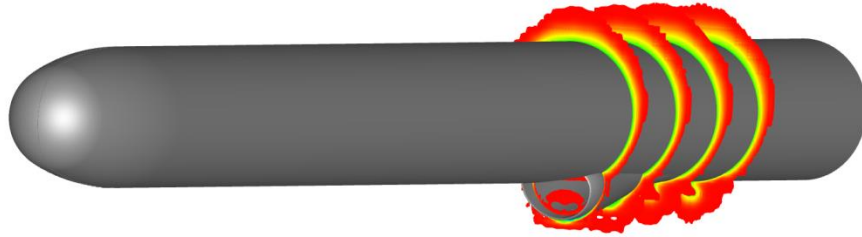
Figure 6-21 Sections Demonstrated on Final Configuration
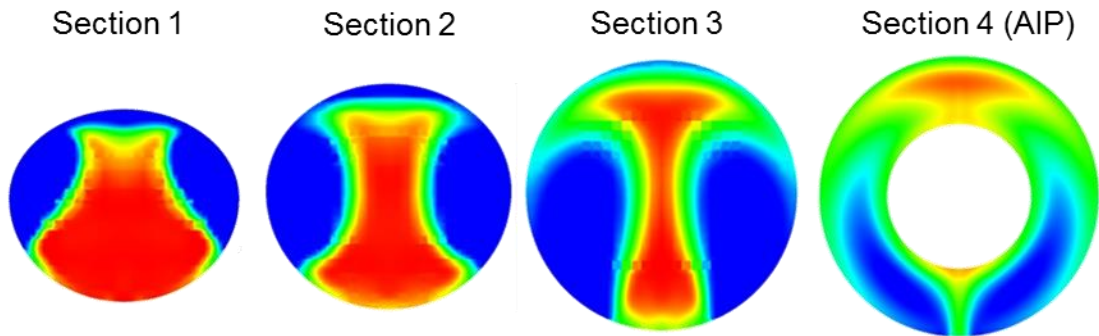
Figure 6-22 Inner sections of Initial Geometry (G_0)
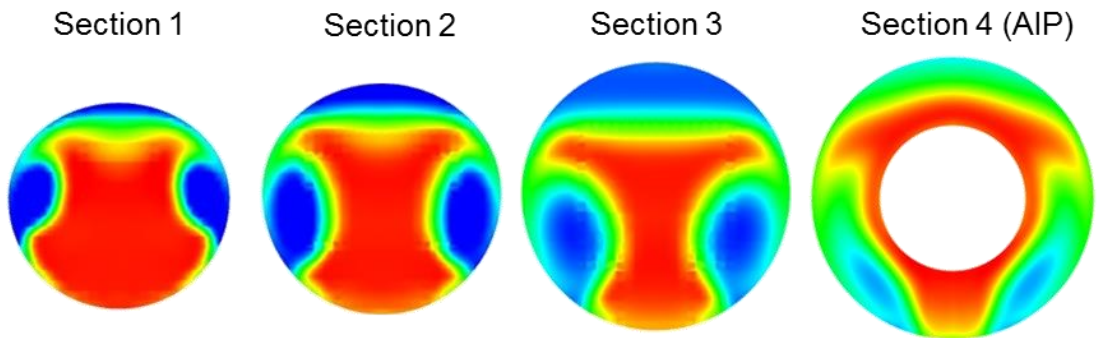
Figure 6-23 Inner sections of STP_1
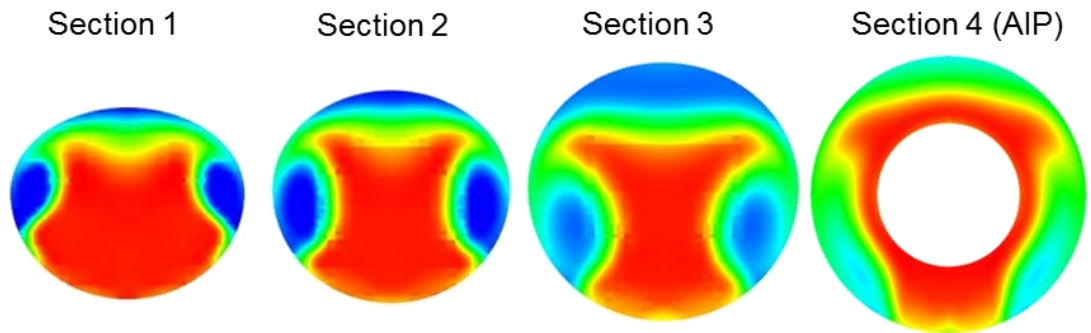
Figure 6-24 Inner sections of STP_2
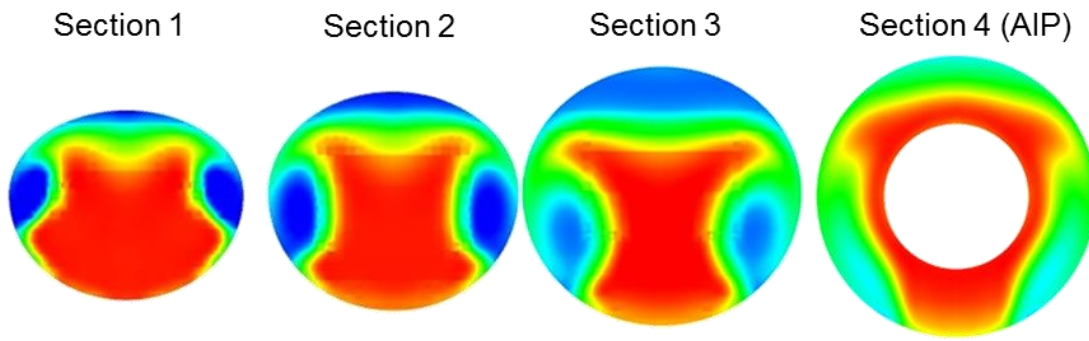
Figure 6-25 Inner sections of STP$_3$
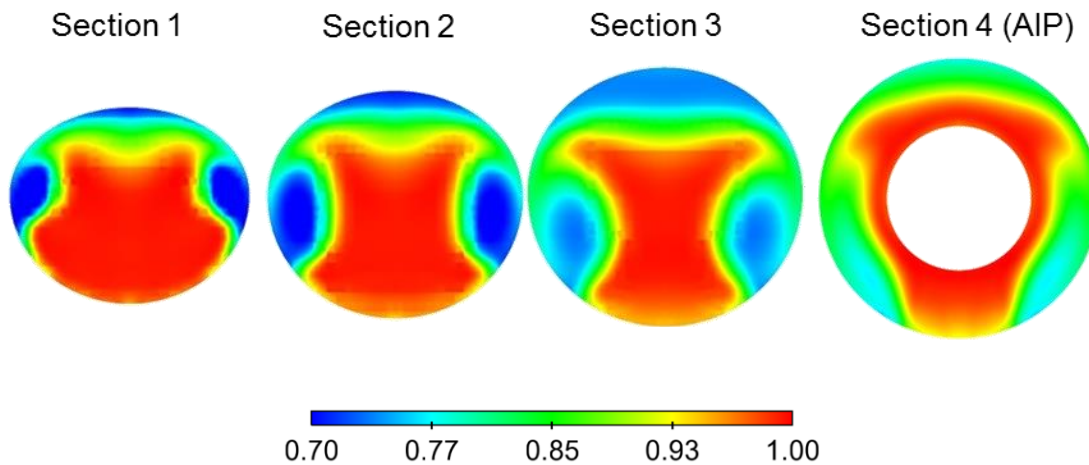
Figure 6-26 Inner sections of STP$_5$

It can be seen from Figure 6-22 that there is a flow separation on the upper side region of the initial geometry and it moves down through to AIP. Separated flow reattaches the upper surface at near Section 3. Separation region grows as it moves down and creates the maximum separation area at lower surface at Section 3. Flow reattaches in the middle of the lower surface between Section 3 and Section 4. Large separation region is dominates the performance of intake on the lower side symmetrically and it creates high total pressure disturbance and non-uniform total pressure distribution at AIP.

Remarkable difference obtained at second iteration of optimization algorithm STP$_1$ configuration has much higher PR value compared to initial geometry. Since characteristics of the optimization algorithm fast increase of PR and dramatic decrease of DC obtained at yet first iteration. Separation formation can be seen at this second configuration but separation is weaker than initial intake configuration, could be seen at Section 3 in Figure 6-23. Considerable amount of higher total pressure,

distributed upper side region compared to initial geometry. Also weak flow separation creates higher PR and lower DC at the AIP section of STP_1.

After second iteration intake sections flow visualizations are represented in Figure 6-24. STP_2 creates different flow separation form compared to G_0 and STP_1. Lower side vortices move up to middle side of the sections and separation is weakened at all sections. At the AIP section upper separation region reduced and lower vortices are weakened. PR increased and DC is diminished compared to previous intake configuration.

A little difference can be seen on STP_3 intake geometry compared to STP_2 (Figure 6-25). Total pressure distribution is more uniform at the AIP section. There are little lower side separation regions at this configuration. After this iteration following intake geometries STP_4 and STP_5 are obtained from iteration 4 and 5. STP_4 and STP_5 section contours are nearly same; hence only STP_5 sections are given. (Figure 6-26)

For the last iteration design parameters are changed little and this change creates little improvement on PR and weakening on DC. STP_5 is the final intake geometry obtained by optimization algorithm. Final geometry has 0.9450 PR and 0.0262 DC while $\dot{m}_{corr}$ is 4.43 kg/s at the end of optimization process. Symmetry section pressure recovery contours of STP_5 are given in Figure 6-27.

The final geometry STP_5 is compared to initial geometry and it represented in Figure 6-28.
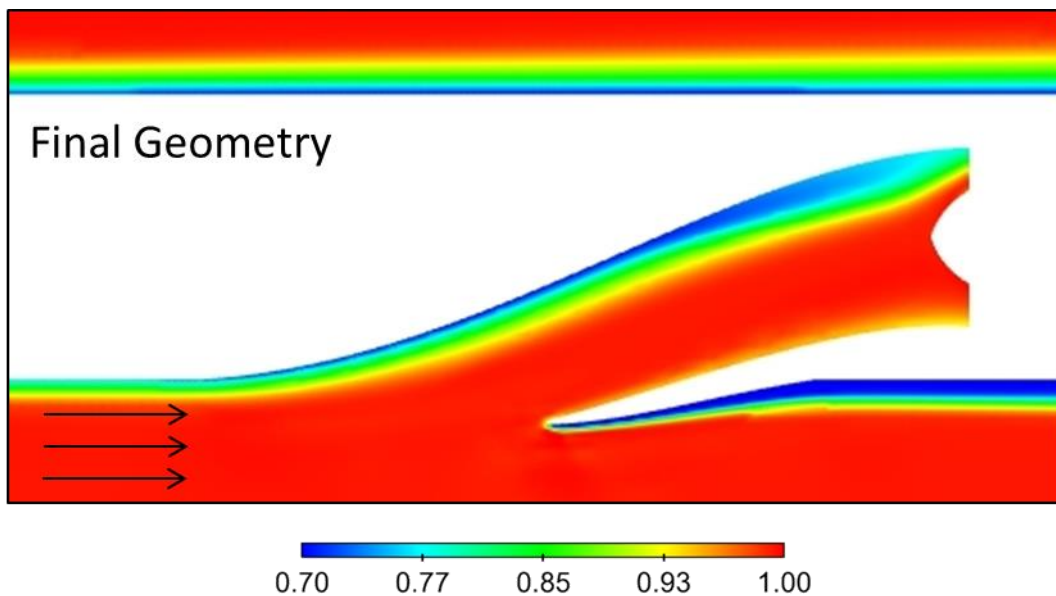
Figure 6-27 PR contours from symmetry Plane of STP_5 Geometry

89
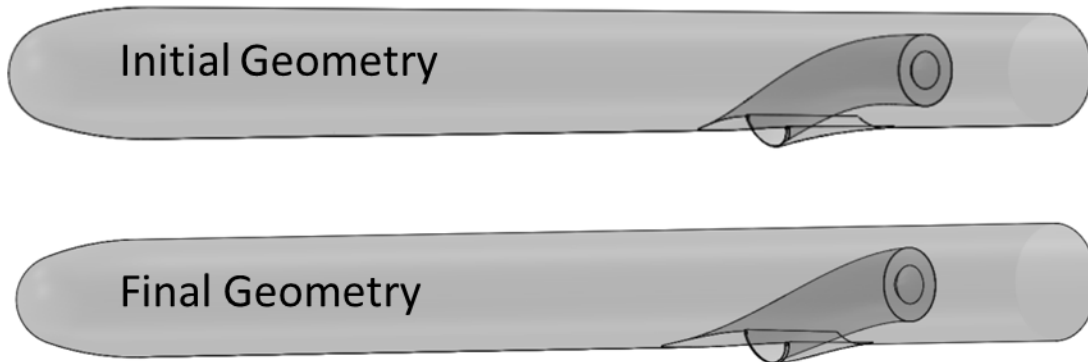
Figure 6-28 STP$_5$ Final Geometry compared to Initial Geometry

6.4 Off-Design Condition Comparison of Initial and Final Intake Geometries

Performance of final geometry, STP$_5$, is investigated at different off-design conditions and compared to initial geometry G$_0$. Cruise conditions generally operate at small angle of attacks and side-slip angles. Off-design CFD analyses are done in order to test performance of final geometry, STP$_5$, at different flight conditions.

The PR and DC$_{DPCP}$ values of the final geometry at 0.8 Mach and 0° side-slip condition by changing angle of attacks are presented and compared to initial geometry at Figure 6-29 and Figure 6-30 respectively.
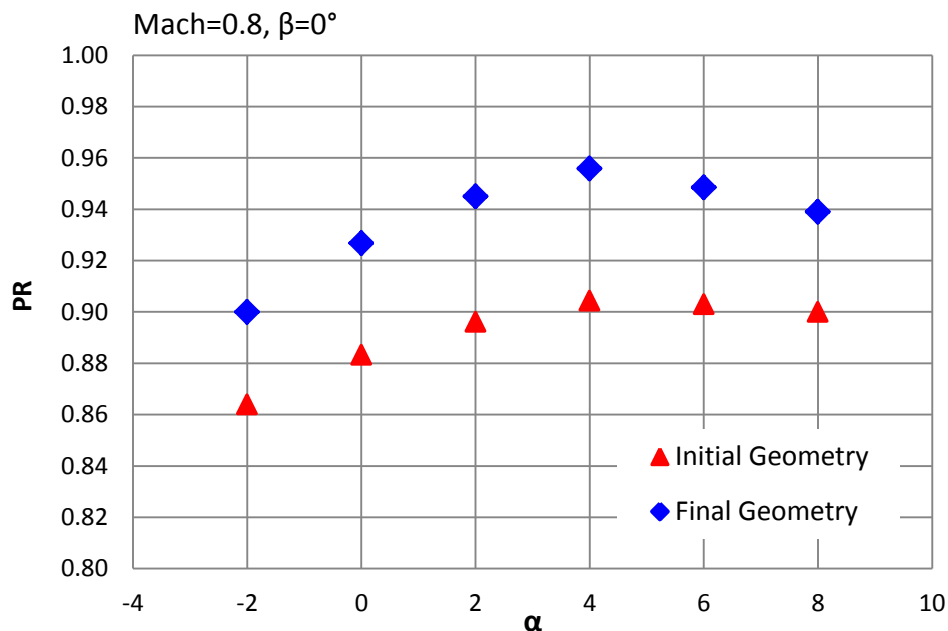
Figure 6-29 Initial and Final Configuration PR at Different Angle of Attacks
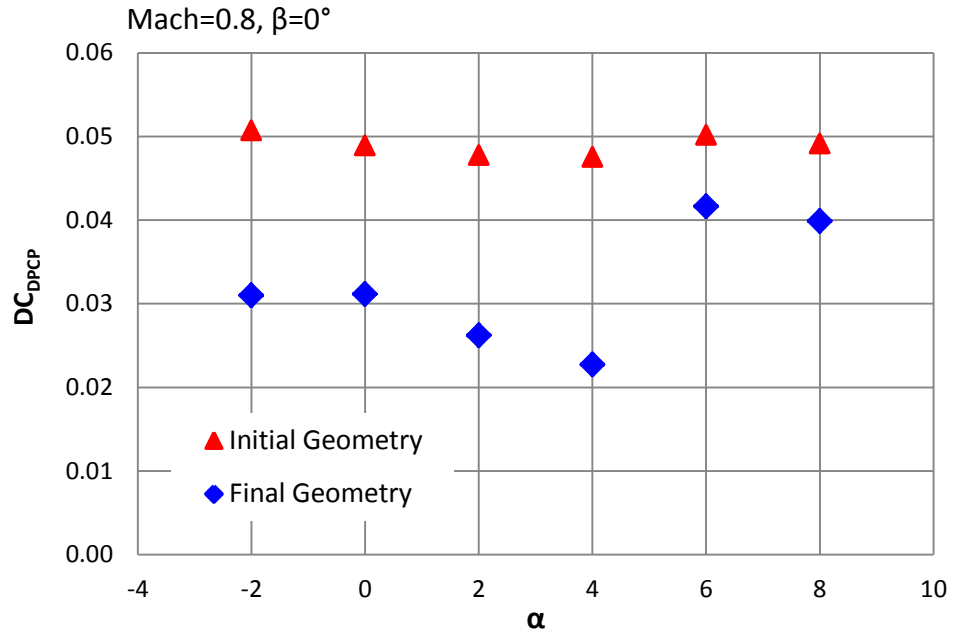
Figure 6-30 Initial and Final Configuration DC$_{DPCP}$ at Different Angle of Attacks

The PR and DC$_{DPCP}$ values of the final geometry a at 0.8 Mach and 2° angle of attack condition by different side-slip angles are presented and compared to initial geometry at Figure 6-31 and Figure 6-32 respectively.
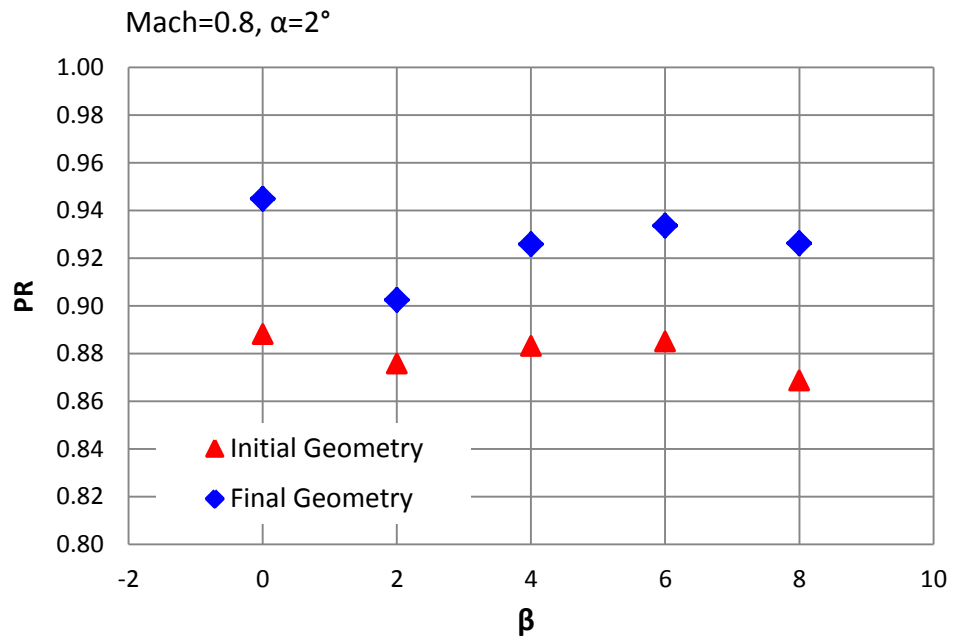
Figure 6-31 Initial and Final Configuration PR at Different Side-Slip Angles
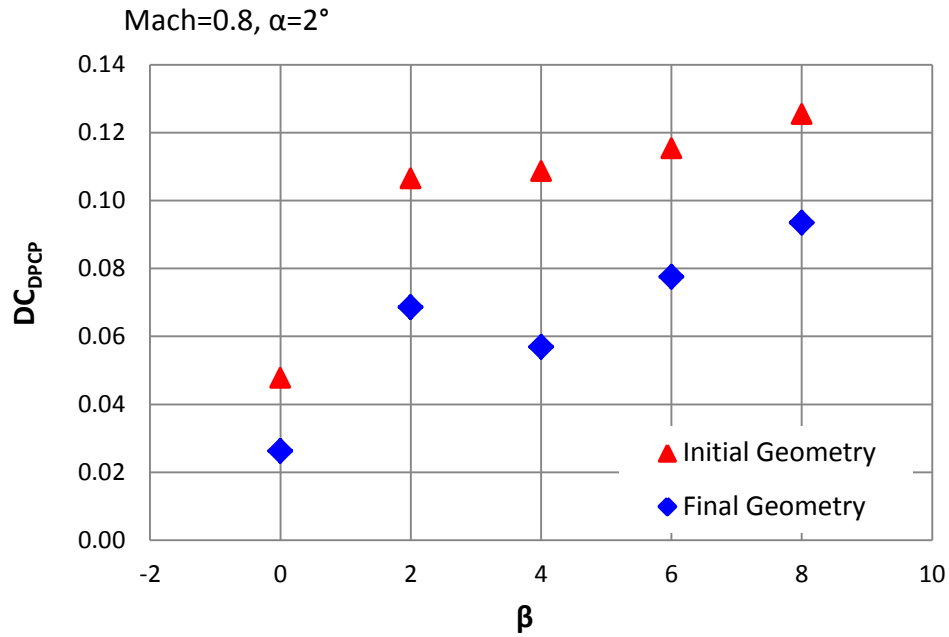
Figure 6-32 Initial and Final Configuration DC_{DPCP} at Different Side-Slip Angles

According to off-design conditions study for almost all off-design conditions final geometry has better performance compared to initial intake geometry G_0. It can be said that optimization algorithm improved the intake geometry not only at certain design condition but also off-design flight conditions.

CHAPTER 7

CONCLUSION AND FUTURE WORK

In this thesis, design and optimization study of subsonic-transonic submerged intake for a cruise missile are carried out. Submerged intake parameterization is conducted and a parametric submerged intake for a cruise missile is constructed. A basic optimization algorithm is developed in order to find optimum submerged intake shape for given design requirements and flight conditions by integrating gradient search and line search optimization methods. Validation study of optimization algorithm performed by using random initial submerged intake geometry without using any performance and geometric constrains. After 4 optimization step, final geometry of validation study is obtained as it expected, it has similar shape like pitot type intakes. In validation study, offsets of the lip sections from the missile bodies are increased by the optimization algorithm as PR increases during optimization process. Since there is no geometric limitation of the throat section area, as offset from the body increased, the throat area is increased accordingly. Throat area increment directly related to amount of mass flow rate taken by the intake at a constant flight condition. Thereby PR is increased with the mass flow rate rise, in other words by the increment of the intake offset from the missile body. These results are demonstrated that the optimization algorithm works; such the final geometry shows similarity with the pitot type intakes. In order to limit mass flow rate growth and offset length from the missile body, optimization algorithm is conducted to an initial geometry with applying some geometric constraints. These limitations are employed by assuming a real cruise missile launch platform diameters and radar cross section area characteristics in literature. The throat area is remained constant during the optimization process in order to determine and limit the amount of mass flow rate that passes through the throat area. Objective function contains PR and DC

performance parameters with different weights. Some geometric penalty values are added to the objective function to avoid from undesired geometries. By applying optimization algorithm to the initial geometry of constrained design study, after five optimization iterations 6.4% improvement of PR and 45% enhancement of DC are obtained. Final geometry is achieved 0.945 pressure recovery coefficient and 0.0262 distortion coefficient (DC_{DPCP}).

Even though there is no constraint added in the objective function, in order to keep mass flow rate constant, the mass flow rate is kept constant during design optimization study by confining throat area at a constant value. Since the sensitivity of the subsonic intake geometries, there is no extreme change in shape of diffuser in such optimization studies. Thus except some boundary layer loses, limiting throat cross-section area at a constant value is sufficient to have constant mass flow rate both at throat and AIP section in this study. Only small change of mass flow rate can be seen at the AIP section due to internal separation and secondary flows.

On the other hand, body + intake axial force coefficients are compared between the geometries that are obtained during design iterations. Axial force coefficient is decreased as iterations proceed, and converged to 0.864. Totally about 13% axial force improvement attained during design optimization study.

In order to investigate the final configuration performance at different flight conditions, additional CFD analyses are performed. Specified off-design conditions are analyzed for both initial and final configurations and performances are compared. At all off-design conditions, final configuration has better performance than initial configuration.

In future, optimization study will be continued with additional parameters of subsonic-transonic submerged intake. Lip parameters will be added to optimization algorithm to find optimum lip geometry in order to performance enhancement of submerged intake. Mass flow rate and axial force coefficient could be added to objective function according to design requirements of subsonic-transonic submerged intake of cruise missiles.

REFERENCES

[1] D. Tanks, "Assessing the Cruise Missile Puzzle: How great a defense challenge," The Institute for Foreign Policy Analysis, Washington DC.

[2] H. Avcıoğlu, "A Tool For Trajectory Planning and Performance Verification of Cruise Missiles," Middle East Technical University, Ankara, September, 2000.

[3] E. Fleeman, Tactical Missile Design, Reston,Virginia: AIAA Education Series, 2001.

[4] G. Laruelle, "Air Intakes : Role, Constrains and Design," International Council of the Aeronautiacal Sciences Congress, Les Mureaux, France, 2002.

[5] L. Hime, C. Perez and S. Ferreira, "Review Of The Characteristics of The Submerged Inlets," 18th International Congress of Mechanical Engineering, Ouro Preto, MG, November 6-11, 2005.

[6] O. Akman, G. Akar. and O. Göker, "Ses Altı ve Ses Civarı Hız Rejimlerinde Uçan Jenerik bir Seyir Füzesi için Yarı-Gömülü Hava Alığı Tasarımı" V. Ulusal Havacılık ve Uzay Konferansı, UHUK-2014-096, Erciyes Üniversitesi, Kayseri, 8-11 Eylül 2014.

[7] S. R. Wellborn, T. H. Okiishi and B. A. Reichert, "A Study of the Compressible Flow Through a Diffusing S-Duct," in *NASA Lewis Research Center*, Cleveland , December,1993.

[8] E. S. Taskinoglu, A Multiobjective Shape Optimization Study for A Subsonic Submerged Inlet, New Jersey : The State University of New Jersey, 2004.

[9] T. Reynolds, Flow Control Application in a Submerged Inlet Characterized by Three-Component LDV, Wright-Patterson Air Force Base, Ohio: Graduate School of Engineering and Management Air Force Institute of Technology Air University, 2010.

[10] J. D. Mattingly, Elements of Propulsion:Gas Turbines and Rockets, Blacksburg, Virginia: AIAA Education Series.

[11] J. D. Mattingly, W. H. Heiser and D. T. Pratt, Aircraft Engine Design, Alexander Bell Drive, Reston: AIAA Education Series, 2002.

[12] L. Kyungjae, L. Bohwa, K. Sanghun, S. Y. and D. L., "Inlet Distortion Test with Gas Turbine Engine in the Altitude Engine Test Facility," 27th AIAA Aerodynamic Measurement Technology and Ground Testing Conference, Daejeon, Korea, 28 June-1 July, 2010.

[13] M. Rütten, S. Kuckenburg, S. Koch and M. Rein, "Investigation of the Flow within Partially Submerged Scoop Type Air Intakes," AIAA Applied Aerodynamics Conference, San Diego, CA, 2013.

[14] SAE, "Aerospace Recommended Practive, Gas Turbine Engine Inlet Flow Distortion Guidelines, SAE ARP1420 Rev.B," SAE Aerospace International Group, USA, 2011.

[15] S. E. Tournier and J. D. Paduano, "Flow Analysis and Control in a Transonic Inlet," AIAA.

[16] N. Bissinger and T. Breuer, "Basic Principles – Gas Turbine Compatibility – Intake Aerodynamic Aspects," Encyclopedia of Aerospace Engineering - Volume 8 - Chapter EAE487, Munich, Germany.

[17] E. S. Taskinoglu, A Multiobjective Shape Optimization Study for A Subsonic Submerged Inlet, New Jersey : The State University of New Jersey , May 2004.

[18] A. C. Rabe, "Effectiveness of a Serpentine Inlet Duct Flow Control Scheme at Design and Off-Design Simulated Flight Conditions," Virginia Polytechnic Institute and State University, Blacksburg,Virginia, August 2003.

[19] R. Devine, J. Watterson and R. Cooper, "Performance Improvement of Flush Parallel Walled Auxiliary Intakes by Means of Vortex Generators," in *24. International Congress of the Aeronautical Sciences*, 2004.

[20] B. G. Allan and L. R. Owens, "Numerical Modeling of Flow Control in a Boundary-Layer-Ingesting Offset Inlet Diffuser at Transonic Mach Numbers," NASA Langley Research Center, Hampton.

[21] Nichols, M. R. and Pierpont, P. K., "Preliminary Investigation of a Submerged Air Scoop Utilizing Boundary-Layer Suction to Obtain Increased Pressure Recovery," National Advisory Committee for Aeronautics, Washington, March,1950.

[22] P. K. Pierpont and R. R. Howell, "Low-Speed Investigation of A Semisubmerged Air Scoop With and Without Boundary Layer Suction," National Advisory Committee for Aeronautics (NACA), Washington, 1951.

[23] F. M. Rogallo, "Internal-Flow System For Aircraft," National Advisory Committee for Aeronautics, Washington, October,1940.

[24] C. Frick, W. F. Davis, L. M. Randall and E. A. Mossman, "An Experimental Investigation of NACA Submerged-Duct Entrances," National Advisory Committee for Aeronautics, Washington, 1945.

[25] E. Mosman and L. Randall, "An Experimental Investigation of the Design Variables For NACA Submerged Duct Entrances," National Advisory Committee for Aeronautics, Washington, 1948.

[26] N. Delany, "An Investigation of Submerged Air Inlets on a 1/4 Scale Model of a Typical Fighter-Type Airplane," National Advisory Committee for Aeronautics, Washington, June,1948.

[27] E. A. Mossman, "A Comparison of Two Submerged Inlets at Subsonic and Transonic Speeds," National Advisory Committee for Aeronautics, Washington, September,1949.

[28] R. A. Taylor, "Some Effects of Side-Wall Modifications on the Drag and Pressure Recovery of an NACA Submerged Inlet at Transonic Speeds," National Advisory Committee of Aeronautics, Washington, 1952.

[29] N. J. Martin and C. A. Holzhauser, "An Experimental Investigation at Large Scale of Several Configurations of NACA Submerged Air Intake," National Advisory Committee for Aeronautics, Washington, October,1948.

[30] C. F. Hall and J. Frank, "Ram-Recovery Characteristics of NACA Submerged Inlets at High Subsonic Speeds," National Advisory Committee for Aeronautics, Washington, November, 1948.

[31] J. Axelson and T. R. A., "Preliminary Investigation of the Transonic Characteristics of an NACA Submerged Inlet," National Advisory Committee for Aeronautics , Washington, June,1950.

[32] J. L. Frank, "Pressure-Distribution and Ram-Recovery Characteristics of NACA Submerged Inlets at High Subsonic Speeds," National Advisory Committee for Aeronautics, Washington, July,1950.

[33] J. S. Dennard, "A Transonic Investigation of the Mass Flow and Pressure Recovery Characteristics of Several Types of Auxiliary Air Inlets," National Advisory Committee for Aeronautics, Washington, April,1957.

[34] L. S. Rolls, "A Flight Comparison of a Submerged Inlet and a Scoop Inlet at Transonic Speeds.," National Advisory Committee for Aeronautics, Washington, March,1953.

[35] D. Gault, "An Experimental Investigation of Naca Submerged Air Inlets on 1/5 Scale Model of A Fighter Airplane," National Advisory Committee for Aeronautics (NACA), Washington, 1947.

[36] C. F. Hall and F. D. Barclay, "An Experimental Investigation of NACA Submerged Inlets at High Subsonic Speeds I-Inlets Forward of the Wing Leading Edge," National Advisory Committee for Aeronautics (NACA), Washington, June,1948.

[37] A. H. Sacks and R. J. Spreiter, "Theoritical Investigation of Submerged Inlets at Low Speeds," National Advisory Committee for Aeronautics, Washington, August,1951.

[38] J. A. Albers and B. A. Miller, "Effect of Subsonic Inlet Lip Geometry on Predicted Surface and Flow Mach Number Distributions," National Aeronautics and Space Administration, Washington, December,1973.

[39] R. W. Luidens, N. O. Stockman and J. H. Diedrich, "An Approach to Optimum Subsonic Inlet Design," in *24th Annual International Gas Turbine Conference and First Solar Energy Conference*, California, March,1979.

[40] F. H. Hanson and E. A. Mossman, "Effect of Pressure Recovery on the Performance of a Jet-Propelled Airplane," National Advisor Committee for Aeronautics, NACA, Washington, September, 1948.

[41] H. He and X. Li, "Design of S-shaped Submerged Inlet," in *Advanced Materials Research Vols.*, 2011.

[42] J. G. Lee, S. Y. Jung and C. S. Ahn, "Numerical Simulation of Three-Dimensional Flows for Flush Inlet," in *22nd Applied Aerodynamics Conference and Exhibit*, Rhode Island, 2004.

[43] A. L. Vuillerme and S. Deck, "Numercal Simulations of the Flow Inside an S-Shaped Intake Diffuser," in *European Conference for Aerospace Sciences (EUCASS).*

[44] B. L. Berrier, M. B. Carter and B. G. Allan, "High Reynolds Number Investigation of a Flush-Mounted, S-Duct Inlet with Large Amounts of Boundary Layer Ingestion," in *National Aeronautics and Space Administration, NASA/TP-2005-213766*, Virginia, September,2005.

[45] S. Sun, R. Guo and Y. Wu, "Characterization and Performance Enhancement of Submerged Inlet with Flush-Mounted Planar Side Entrance," in *Journal of Propulsion and Power Vol.23, No. 5, September-October*, 2007.

[46] K. M. Loeper and P. King, "Numerical Investigation of Geometric Effects on Performance of S-Ducts," in *47th AIAA Aerospace Sciences Meeting Including The New Horizons Forum and Aerospace Exposition, AIAA 2009-713*, Orlando, Florida, 5 - 8 January 2009.

[47] J. Zhang, C. Wang and K. Lum, "Multidisciplinary Design of S-shaped Intake," in *26th AIAA Applied Aerodynamics Conference, AIAA 2008-7060*, Honolulu, Hawaii, 2008.

[48] E. Reddy and R. Reddy D., "Aerodynamic Shape Optimization of a Subsonic Inlet Using 3-D Euler Computation," in *31 st AIAA/;ASME/SAE/ASEE Joint Propulsion Conference and Exhibit, AIAA 95-2757*, San Diego, July 10-12, 1995.

[49] E. Taskinoglu and D. D. Knight, "Design Optimization for Submerged Inlets," in *41st Aerospace Sciences Meeting and Exhibit, AIAA 2003-1247*, Reno, Nevada, 6-9 January 2003.

[50] Mentor Graphics Corp., "Advanced Immersed Boundary Cartesian Meshing Technology in FloEFD™," 2011.

[51] Mentor Graphics Corp., "Enhanced Turbulence Modelling in FloEFD™," 2011.

[52] FloEFD12, "User Manuel," Mentor Graphics, 2012.

[53] T. Reynolds, "Flow Control Application in a Submerged Inlet Characterized by Three-Component LDV," Graduate School of Engineering and Management Air Force Institute of Technology Air University, Wright-Patterson Air Force Base, Ohio, 2010.